P.138

An Engineering Method
for Interactive Inviscid-Boundary Layers
in Three-Dimensional Hypersonic Flows

by

Christopher J. Riley

A Thesis Submitted to the Graduate Faculty
of North Carolina State University
in Partial Fulfillment of the
Requirements for the Degree of
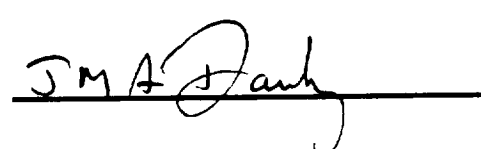Doctor of Philosophy
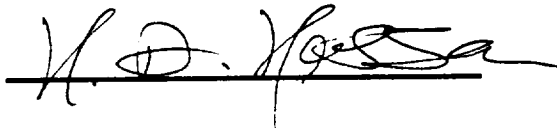
Major Subject: Aerospace Engineering

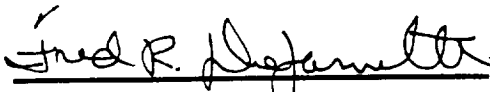## Department of Mechanical and Aerospace Engineering

Raleigh

1992

Approved by:

Chairman of Advisory Committee

An Engineering Method
for Interactive Inviscid-Boundary Layers
in Three-Dimensional Hypersonic Flows

by
Christopher J. Riley

Department of Mechanical and Aerospace Engineering

Raleigh

Abstract

Christopher J. Riley: *An Engineering Method for Interactive Inviscid-Boundary Layers in Three-Dimensional Hypersonic Flows.* (Under the direction of Dr. Fred R. DeJarnette.)

An engineering method has been developed that couples an approximate three-dimensional inviscid technique with the axisymmetric analog and a set of approximate convective-heating equations. The displacement effect of the boundary layer on the outer inviscid flow is calculated and included as a boundary condition in the inviscid technique. This accounts for the viscous interaction present at lower Reynolds numbers. The method is applied to blunted axisymmetric and three-dimensional elliptic cones at angle of attack for the laminar hypersonic flow of a perfect gas. The method is also applied to turbulent and equilibrium-air conditions. The present technique predicts surface heating rates, pressures, and shock shapes that compare favorably with experimental (ground-test and flight) data and numerical solutions of the Navier-Stokes and viscous shock-layer equations. In addition, the inclusion of the viscous interaction significantly improves results obtained at lower Reynolds numbers. The new technique represents a major improvement over current engineering aerothermal methods with only a modest increase in computational effort.

Acknowledgements

The author wishes to thank Dr. Fred R. DeJarnette, Professor of Mechanical and Aerospace Engineering at North Carolina State University, for his guidance during this investigation. It has been both a pleasure and a privilege to work with him. The author would also like to thank E. Vincent Zoby, Dr. Peter A. Gnoffo, H. Harris Hamilton, and the entire Aerothermodynamics Branch of the NASA Langley Research Center for their assistance and technical advice. The author is especially grateful to Dr. F. McNeil Cheatwood of Vigyan, Inc. for his suggestions concerning the manuscript. Finally, the author wishes to acknowledge the support given by his family and friends over the last few years. In particular, the love and encouragement from his wife Tina and daughter Corinne were invaluable.

Table of Contents

List of Figures

Nomenclature

Units for symbols are given in Appendix A.

$\mathcal{A}, \mathcal{B}, \mathcal{D}, \mathcal{J}$	geometric factors
B, C, D, b, c, d	conic section parameters (wind axes)
$\bar{B}, \bar{b}$	conic section parameters (body axes)
$\tilde{B}$	ratio of velocity gradients at stagnation point
C_f	local skin friction coefficient (see Eq. H.2)
C_p	specific heat at constant pressure
c_1, c_2, c_3, c_4, c_5	turbulent heating equation parameters
e	error between calculated and geometric shock layer thickness
$\mathbf{e}_{\bar{s}}, \mathbf{e}_{\bar{t}}$	tangential unit vectors on body surface
$\mathbf{e}_x, \mathbf{e}_r, \mathbf{e}_\phi$	unit vectors of cylindrical coordinate system (wind axes)
$\mathbf{e}_{\bar{x}}, \mathbf{e}_{\bar{r}}, \mathbf{e}_{\bar{\phi}}$	unit vectors of cylindrical coordinate system (body axes)
$\mathbf{e}_x, \mathbf{e}_y, \mathbf{e}_z$	unit vectors of Cartesian coordinate system (wind axes)
$\mathbf{e}_{\bar{x}}, \mathbf{e}_{\bar{y}}, \mathbf{e}_{\bar{z}}$	unit vectors of Cartesian coordinate system (body axes)
$\mathbf{e}_\xi, \mathbf{e}_\beta, \mathbf{e}_n$	unit vectors of shock-oriented coordinate system
$\mathbf{e}_{\bar{\xi}}, \mathbf{e}_{\bar{\beta}}, \mathbf{e}_{\bar{n}}$	unit vectors of streamline coordinate system
f	radius in wind axes
$\bar{f}$	radius in body axes

G	$\cos\Gamma$
H	total enthalpy
h	enthalpy
h_y, h_z	scale factors in stagnation region
h_ξ, h_β	scale factors of shock-oriented coordinate system
$h_{\bar\xi}, h_{\bar\beta}$	scale factors of streamline coordinate system
k	thermal conductivity
L	reference length
M	Mach number
m	heating equation parameter
N	velocity profile exponent
n	coordinate normal to shock
$\bar n$	coordinate normal to body
$\mathbf{P}$	position vector
Pr	Prandtl number; $Pr = \dfrac{\mu C_p}{k}$
p	pressure
q	heat transfer rate
R	radius of curvature
Re	Reynolds number; $Re = \dfrac{\rho u L}{\mu}$
R_y, R_z	shock principal radii of curvature at stagnation line
$R_{\bar y}, R_{\bar z}$	body principal radii of curvature at nose

$\mathcal{R}$	specific gas constant
S	entropy
St	Stanton number; $St = \dfrac{q_w}{\rho_e u_e (h_{aw} - h_w)}$
s	distance along shock line
$\bar{s}$	distance along body surface
T	temperature
t	time; time-like variable of integration
U, V	velocity components in stagnation region
u, v, w	velocity components of shock-oriented coordinate system
$\bar{u}, \bar{v}, \bar{w}$	velocity components of streamline coordinate system
V	velocity magnitude
$\mathbf{V}$	velocity vector
w_f	weighting function in transition region
x, r, ϕ	cylindrical coordinate system (wind axes)
$\bar{x}, \bar{r}, \bar{\phi}$	cylindrical coordinate system (body axes)
x, y, z	Cartesian coordinate system (wind axes)
$\bar{x}, \bar{y}, \bar{z}$	Cartesian coordinate system (body axes)
α	angle of attack
Γ	surface angle relative to wind axes
$\bar{\Gamma}$	surface angle relative to body axes
γ	ratio of specific heats

δ	boundary layer thickness
δ^*	boundary layer displacement thickness
δ_ϕ	surface angle in circumferential direction (wind axes)
$\bar{\delta}_\phi$	surface angle in circumferential direction (body axes)
ϵ	determines axial distance from origin where integration of shock variables begins (see Appendix D)
η	stream function ratio, Ψ/Ψ_s
θ	boundary layer momentum thickness
$\bar{\theta}$	inclination angle of surface streamlines
κ_ξ, κ_β	shock curvatures
μ	viscosity
ξ, β	shock coordinates
$\bar{\xi}, \bar{\beta}$	streamline coordinates
$\tilde{\xi}, \tilde{\beta}$	transformed shock coordinates
ρ	density
σ	surface angle, $\phi - \delta_\phi$
$\bar{\sigma}$	surface angle, $\bar{\phi} - \bar{\delta}_\phi$
τ	skin friction
Φ, Ψ	stream functions (shock coordinates)
$\bar{\Phi}, \bar{\Psi}$	stream functions (body coordinates)

Subscripts

aw	adiabatic wall
b	body
beg	beginning of transition region
e	boundary layer edge
end	end of transition region
geo	geometric
i	marching step
inc	incompressible
L	laminar
n	nose
ref	reference
s	shock
T	turbulent
w	wall
0	stagnation point
∞	freestream conditions

Superscripts

$*$	reference value
$\prime$	dimensional quantity

1   Introduction

The thermal design of hypersonic vehicles involves accurately and reliably predicting the convective heating over the surface of the vehicle. Such results may be obtained by numerically solving the Navier-Stokes (NS) equations [1] or one of their various subsets such as the parabolized Navier-Stokes (PNS) [2] and viscous shock-layer (VSL) equations [3, 4, 5] for the flowfield surrounding the vehicle. However, due to the excessive computer run times and storage requirements of these CFD (computational fluid dynamics) approaches, they are impractical for the preliminary design environment where a range of geometries and flow parameters are to be studied. Even coupled solutions of the outer inviscid region described by the Euler equations and the inner viscous layer described by the boundary layer equations may be too computer intensive for preliminary design [6, 7].

On the other hand, engineering inviscid-boundary layer methods [8, 9, 10, 11] have been demonstrated to adequately predict the heating over a wide range of geometries and aerothermal environments. Various approximations in the inviscid and boundary layer regions reduce the computer time needed to generate a solution. This reduction in computer time makes the engineering aerothermal methods ideal for parametric studies.

The approach followed by the existing engineering methods is similar to a "classic" boundary layer analysis. The inviscid flowfield is calculated and that solution controls

the viscous boundary layer solution. In this decoupled approach, the viscous layer is assumed to have a negligible effect on the outer inviscid region. This assumption is accurate for relatively high Reynolds number flows where the boundary layer is thin compared to the shock layer. At lower Reynolds numbers, the thicker boundary layer displaces the outer flow and increases the surface pressure. These changes in the pressure may also significantly increase the heat transfer. The displacement effect of the boundary layer on the outer inviscid layer is called *viscous interaction* [12]. Neglecting the viscous interaction at these lower Reynolds numbers may lead to inaccurate results.

Two of the simpler engineering methods that are currently used are AERO-HEAT [8, 9] and INCHES [10]. Both use the "axisymmetric analog" concept [13] which allows axisymmetric boundary layer techniques to be applied to three-dimensional (3-D) flows provided the inviscid surface streamlines are known. AERO-HEAT calculates approximate streamlines based solely on the body geometry. INCHES uses an approximate expression for the scale factor in the windward and leeward planes that describes the spreading of surface streamlines. Circumferential heating rates are then generated by an empirical relation. Another area of approximation is the surface pressure distribution employed by the engineering methods. AEROHEAT assumes modified Newtonian theory which is inaccurate for slender bodies, whereas INCHES uses an axisymmetric Maslen technique [14, 15]. The deficiencies and limitations of these approximations to the surface streamlines and pres-

sures in the engineering aerothermal methods, along with their corresponding effects on the surface heat transfer, have been documented in Refs. [16] –[18].

To address these limitations and improve the capability of the engineering methods for lower Reynolds number flows, an engineering, interactive inviscid-boundary layer method for 3-D hypersonic flows has been developed. Jackson [19] developed a similar technique for 2-D and axisymmetric flows. The present method includes a simplified inviscid technique for computing the 3-D outer flow, a method of computing surface streamlines that allows the use of any axisymmetric boundary layer technique for the viscous solution, and an improved coupling between the viscous and inviscid solutions. This coupling of the two regions accounts for the viscous interaction effects.

The approximate 3-D inviscid method [20, 21, 22] employed here is more accurate than modified Newtonian theory and has a wider range of applicability than the axisymmetric Maslen technique. The inviscid method uses two stream functions that approximate the actual stream surfaces in the shock layer and a modified form of the Maslen second-order pressure equation [23]. Inviscid flowfields have been calculated over 3-D blunted noses as well as 3-D afterbodies with reasonable accuracy [22]. In addition, the method is much faster than numerical solutions of the inviscid (Euler) equations [22]. The first portion of the paper outlines this approximate inviscid technique.

Improved surface streamlines are calculated based on both the body geometry and surface pressure distribution. (Although the stream surfaces in the inviscid method

define surface streamlines, they are approximate and are not constrained to give the correct streamline directions on the body surface.) With the streamlines known, the axisymmetric analog allows axisymmetric boundary layer methods to be employed along each streamline. In lieu of numerically integrating the boundary layer equations, a set of approximate convective-heating equations developed by Zoby [24] is used for the viscous solution. This keeps computer costs to a minimum. The displacement effect of the boundary layer on the inviscid flow is computed and included as a new boundary condition in the inviscid technique. The later chapters present derivations of the surface streamline and convective-heating equations as well as a description of the inclusion of the effects of viscous interaction.

Results including shock shapes, surface pressures and heating rates are presented for spherically-blunted and 3-D elliptic cones at angle of attack for laminar and turbulent conditions. Both perfect gas and equilibrium-air flows are considered. Comparisons are made between results of the present technique, more exact methods (Euler, VSL, and NS), and available experimental data to demonstrate the accuracy and capability of the present engineering technique.

2 Inviscid Analysis

This chapter outlines the approximate technique used in the outer inviscid region of the shock layer. Although much of this material has been presented previously [20, 21, 22], a detailed description of the method is given for completeness. All variables used in the analysis are nondimensionalized by the reference quantities given in Appendix A.

2.1 Coordinate Systems

The three-dimensional shock surface can be represented by

$$r = f(x, \phi) \tag{2.1.1}$$

where (x, r, ϕ) are cylindrical coordinates with corresponding unit vectors $(\mathbf{e}_x, \mathbf{e}_r, \mathbf{e}_\phi)$. The x axis is aligned with the freestream velocity vector and is normal to the shock surface at the origin. Two angles, $\delta_\phi(x, \phi)$ and $\Gamma(x, \phi)$, describe the shock wave shape and are defined as

$$\tan\delta_\phi = \frac{1}{f}\frac{\partial f}{\partial \phi} \qquad \tan\Gamma = \frac{\partial f}{\partial x}\cos\delta_\phi \tag{2.1.2}$$

An additional angle that is useful in dealing with Cartesian coordinates is given by $\sigma = \phi - \delta_\phi$. All angles are shown in Fig. 2.1 and Fig. 2.2. For the special case of axisymmetric flow, $r = f(x)$, $\Gamma = \Gamma(x)$, $\delta_\phi = 0$, and $\sigma = \phi$.

Next a shock-oriented curvilinear coordinate system (ξ, β, n) is defined where ξ and β represent coordinates of a point on the shock surface and n is the inward distance
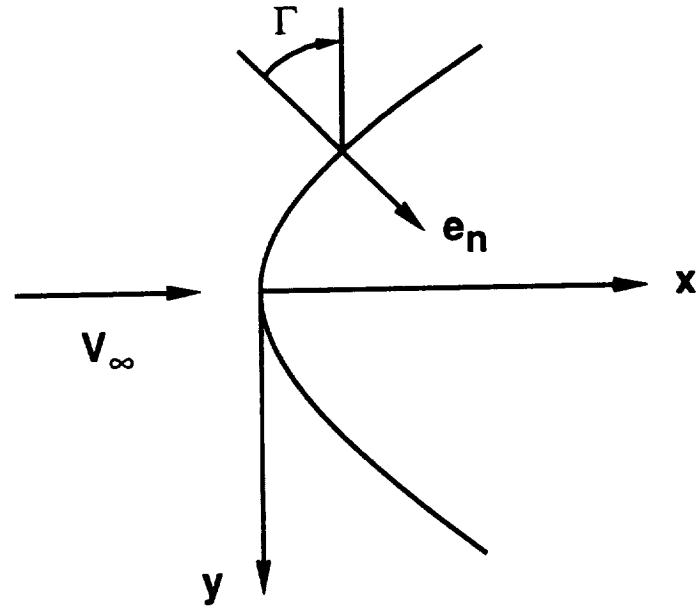
Figure 2.1. Shock wave geometry: side view.
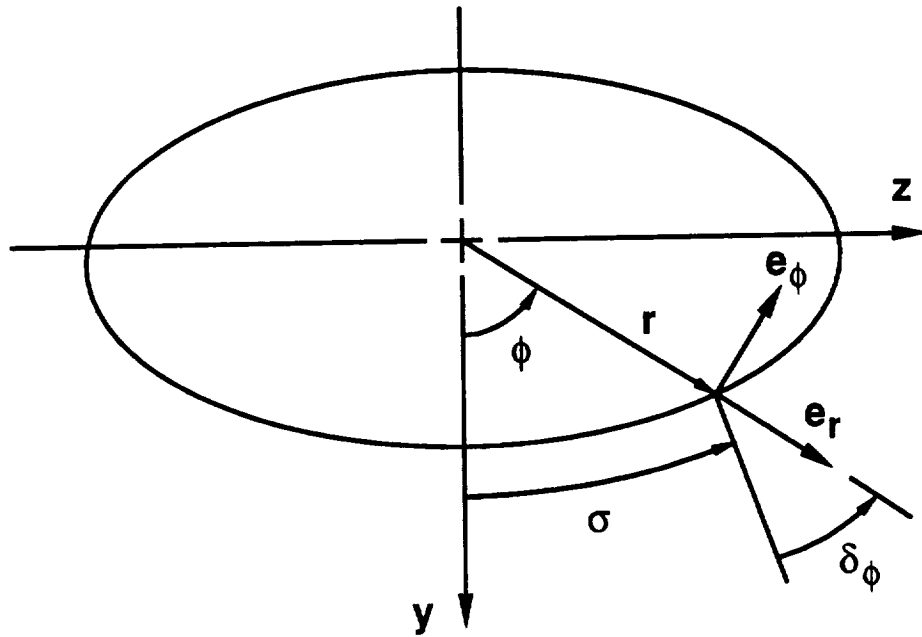
Figure 2.2. Shock wave geometry: rear view.

normal to the shock. Differential arc lengths along each coordinate direction at the shock are $h_\xi \, d\xi$, $h_\beta \, d\beta$, and dn where h_ξ and h_β are scale factors for the corresponding coordinates. This coordinate system is well-suited for hypersonic flow ($M_\infty \gg 1$) and thin shock layers.

The unit vector in the normal direction is defined by

$$e_n \equiv \frac{-\nabla F}{|\nabla F|} \qquad (2.1.3)$$

where

$$F(x, r, \phi) \equiv r - f(x, \phi) = 0 \qquad (2.1.4)$$

The remaining unit vectors, e_ξ and e_β, are tangent to the shock surface and are chosen such that e_ξ is in the direction of the tangential velocity just inside the shock surface. Since the tangential component of the freestream velocity is unchanged across the shock wave, the unit vector e_ξ may be found by subtracting the normal velocity from the freestream velocity as

$$e_\xi \equiv \frac{e_x - (e_x \cdot e_n)e_n}{|e_x - (e_x \cdot e_n)e_n|} \qquad (2.1.5)$$

The unit vector e_β is then defined to be perpendicular to e_ξ and e_n and is given by

$$e_\beta \equiv e_n \times e_\xi \qquad (2.1.6)$$

Lines of constant β are shown in Fig. 2.3 and Fig. 2.4. By using Eqs. (2.1.1)–(2.1.6),
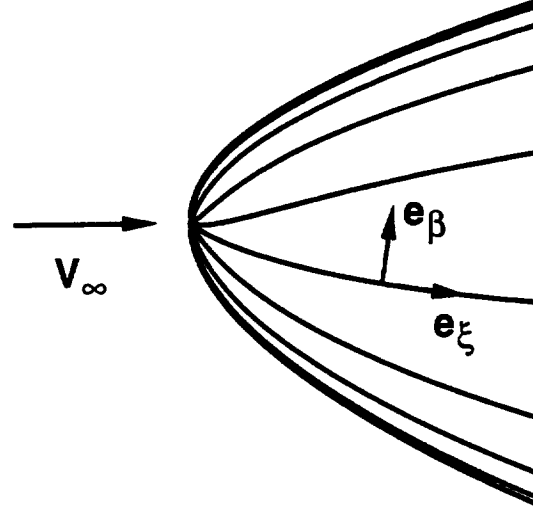
Figure 2.3. Shock-oriented curvilinear coordinate system: side view.

the unit vectors of the curvilinear coordinate system become

$$\mathbf{e}_\xi = \cos\Gamma \mathbf{e}_x + \sin\Gamma \cos\delta_\phi \mathbf{e}_r - \sin\Gamma \sin\delta_\phi \mathbf{e}_\phi$$

$$\mathbf{e}_\beta = \sin\delta_\phi \mathbf{e}_r + \cos\delta_\phi \mathbf{e}_\phi \qquad (2.1.7)$$

$$\mathbf{e}_n = \sin\Gamma \mathbf{e}_x - \cos\Gamma \cos\delta_\phi \mathbf{e}_r + \cos\Gamma \sin\delta_\phi \mathbf{e}_\phi$$

Written in Cartesian coordinates,

$$\mathbf{e}_\xi = \cos\Gamma \mathbf{e}_x + \sin\Gamma \cos\sigma \mathbf{e}_y + \sin\Gamma \sin\sigma \mathbf{e}_z$$

$$\mathbf{e}_\beta = -\sin\sigma \mathbf{e}_y + \cos\sigma \mathbf{e}_z \qquad (2.1.8)$$

$$\mathbf{e}_n = \sin\Gamma \mathbf{e}_x - \cos\Gamma \cos\sigma \mathbf{e}_y - \cos\Gamma \sin\sigma \mathbf{e}_z$$

Although this curvilinear coordinate system is orthogonal at the shock surface, it is

nonorthogonal within the shock layer for a general three-dimensional shock. However,
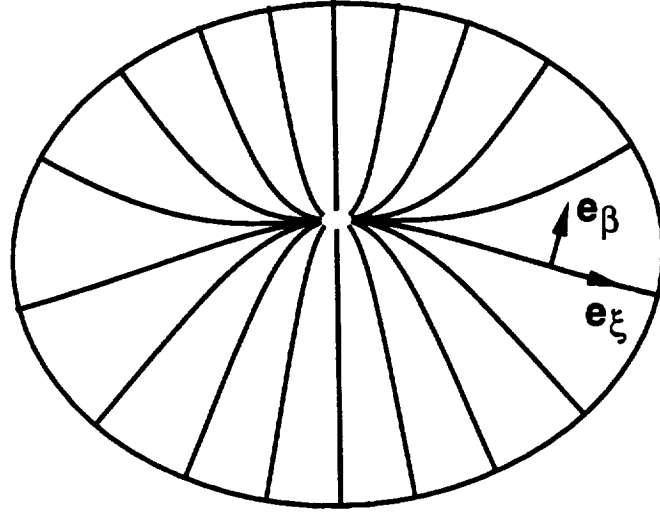
Figure 2.4. Shock-oriented curvilinear coordinate system: front view.

for thin shock layers, orthogonality may be assumed in the outer inviscid region. The nonorthogonality of the curvilinear coordinate system is only important near the body surface in the boundary layer. The transformations between the curvilinear, cylindrical, and Cartesian coordinates on the shock surface and in the shock layer are detailed in Appendix B.

The velocity is defined in terms of the unit vectors at the shock as

$$\mathbf{V} = u\mathbf{e}_\xi + v\mathbf{e}_n + w\mathbf{e}_\beta$$

From the definitions of $\mathbf{e}_\xi$ and $\mathbf{e}_\beta$, the crossflow velocity component at the shock, w_s, is equal to zero.

2.2 Governing Equations

In this section, the governing conservation equations for a steady, inviscid, and adiabatic flow are developed in the curvilinear coordinate system. By examining the shock layer geometry, approximations are made that allow for a simpler solution of the outer inviscid flowfield.

2.2.1 Stream Functions

The continuity equation for three-dimensional flows is given by

$$\nabla \cdot (\rho \mathbf{V}) = 0$$

This equation may be solved by the introduction of two stream functions as

$$\rho \mathbf{V} = \nabla \Psi \times \nabla \Phi$$

where Ψ and Φ represent the two stream functions [23]. Intersections of these stream functions define streamline paths.

Rewriting this equation in the shock-oriented curvilinear coordinate system yields

$$
\begin{aligned}
\rho u h_\beta \mathcal{B} &= \frac{\partial \Psi}{\partial \beta}\frac{\partial \Phi}{\partial n} - \frac{\partial \Psi}{\partial n}\frac{\partial \Phi}{\partial \beta} \\[2mm]
\rho v h_\xi h_\beta \mathcal{A}\mathcal{B} &= \frac{\partial \Psi}{\partial \xi}\frac{\partial \Phi}{\partial \beta} - \frac{\partial \Psi}{\partial \beta}\frac{\partial \Phi}{\partial \xi} \\[2mm]
\rho w h_\xi \mathcal{A} &= \frac{\partial \Psi}{\partial n}\frac{\partial \Phi}{\partial \xi} - \frac{\partial \Psi}{\partial \xi}\frac{\partial \Phi}{\partial n}
\end{aligned}
\tag{2.2.1}
$$

where the coordinate system is assumed to be orthogonal and the geometric factors $\mathcal{A}$ and $\mathcal{B}$ are derived in Appendix B. They are given by

$$\mathcal{A} = 1 - n\kappa_\xi \qquad\qquad \mathcal{B} = 1 - n\kappa_\beta$$

where κ_ξ and κ_β represent the curvatures of the shock surface in the ξ-n and β-n planes, respectively. As noted in Refs. [14] and [23] for blunt bodies at hypersonic speeds, most of the mass flow is near the shock wave where the velocity component w is small. A simplifying assumption for the outer inviscid layer is that $w = 0$ throughout the shock layer. From Eq. (2.2.1), it is seen that $\Phi(\beta)$ satisfies this assumption. Thus, if Φ is set equal to β, Ψ becomes

$$\frac{\partial \Psi}{\partial n} = -\rho u h_\beta \mathcal{B} \tag{2.2.2}$$

$$\frac{\partial \Psi}{\partial \xi} = \rho v h_\xi h_\beta \mathcal{A} \mathcal{B} \tag{2.2.3}$$

These definitions of Ψ and Φ are not unique, and because of the above assumption, they satisfy the exact flowfield equations only at the shock wave. The intersections of planes of constant β with the shock surface are referred to as *shock lines*. Shock lines are in the direction of the ξ coordinate, and for axisymmetric flow, planes of constant β are meridional planes (see Figs. 2.3 and 2.4).

2.2.2 Pressure Equation

The momentum equations for steady, inviscid flow may be written as

$$\mathbf{V} \cdot \nabla \mathbf{V} = -\frac{1}{\rho} \nabla p \tag{2.2.4}$$

Writing these equations in the (ξ, β, n) system gives the following momentum equation normal to the shock (assuming $w = 0$):

$$\frac{u}{\mathcal{A}} \left(\frac{1}{h_\xi} \frac{\partial v}{\partial \xi} + u \kappa_\xi \right) + v \frac{\partial v}{\partial n} = -\frac{1}{\rho} \frac{\partial p}{\partial n} \tag{2.2.5}$$

Now transform this equation from the (ξ, β, n) system to a new set of computational variables $(\tilde{\xi}, \tilde{\beta}, \eta)$ where

$$\tilde{\xi} = \xi \qquad \tilde{\beta} = \beta \qquad \eta = \frac{\Psi}{\Psi_s}$$

By letting $\Psi = 0$ define the body surface, $\eta = 1$ on the shock and $\eta = 0$ on the body. Using the chain rule of partial differentiation, the partial derivatives in the two coordinate systems are related by

$$\frac{\partial}{\partial \xi} = \left(\frac{\partial \tilde{\xi}}{\partial \xi}\right) \frac{\partial}{\partial \tilde{\xi}} + \left(\frac{\partial \tilde{\beta}}{\partial \xi}\right) \frac{\partial}{\partial \tilde{\beta}} + \left(\frac{\partial \eta}{\partial \xi}\right) \frac{\partial}{\partial \eta}$$

$$\frac{\partial}{\partial n} = \left(\frac{\partial \tilde{\xi}}{\partial n}\right) \frac{\partial}{\partial \tilde{\xi}} + \left(\frac{\partial \tilde{\beta}}{\partial n}\right) \frac{\partial}{\partial \tilde{\beta}} + \left(\frac{\partial \eta}{\partial n}\right) \frac{\partial}{\partial \eta}$$

Note that since no derivative with respect to β appears in the normal momentum equation, its partial derivative is not included here. With the help of Eqs. (2.2.2) and (2.2.3), the partial derivatives become

$$\frac{\partial}{\partial \xi} = \frac{\partial}{\partial \tilde{\xi}} + \frac{h_\xi h_\beta}{\Psi_s} \left[\rho v \mathcal{A} \mathcal{B} - \eta (\rho v)_s\right] \frac{\partial}{\partial \eta} \qquad (2.2.6)$$

$$\frac{\partial}{\partial n} = -\frac{\rho u h_\beta \mathcal{B}}{\Psi_s} \frac{\partial}{\partial \eta} \qquad (2.2.7)$$

Substitute the transformation into Eq. (2.2.5) to obtain

$$\frac{\partial p}{\partial \eta} = \frac{\Psi_s}{h_\beta \mathcal{A} \mathcal{B}} \left(\frac{1}{h_\xi} \frac{\partial v}{\partial \tilde{\xi}} + u \kappa_\xi\right) - \eta \frac{(\rho v)_s}{\mathcal{A} \mathcal{B}} \frac{\partial v}{\partial \eta} \qquad (2.2.8)$$

By substituting n into Eqs. (2.2.6) and (2.2.7), an expression for the velocity component v normal to the shock can be obtained and is given by

$$v = \frac{u}{\mathcal{A}} \frac{1}{h_\xi} \frac{\partial n}{\partial \tilde{\xi}} + \eta \frac{(\rho v)_s}{\rho \mathcal{A} \mathcal{B}} \qquad (2.2.9)$$

The only assumptions used in Eqs. (2.2.8) and (2.2.9) are that the velocity component w is equal to zero throughout the shock layer and that the curvilinear coordinate system is strictly orthogonal. To obtain explicit expressions for the pressure and normal velocity component, additional assumptions are required. The following approximations, which are consistent with the simplifications in Refs. [14] and [23], are valid for hypersonic flow and thin shock layers:

$$\rho \approx \rho_s \qquad\qquad n \approx \left(\frac{\partial n}{\partial \eta}\right)_s (\eta - 1)$$

$$u \approx u_s \qquad\qquad \frac{\partial \rho_s}{\partial \xi} \approx 0$$

$$\mathcal{A} \approx 1 \qquad\qquad \frac{\partial v}{\partial \xi} \approx 0$$

$$\mathcal{B} \approx 1$$

Relations for the derivative of the scale factor h_β (see Appendix B) and the velocity components at the shock (see Appendix C) are also needed to reduce Eqs. (2.2.8) and (2.2.9) to their final form. They are given by

$$\frac{1}{h_\xi h_\beta}\frac{\partial h_\beta}{\partial \xi} = \frac{\sin\Gamma}{h_\beta}\frac{\partial \sigma}{\partial \beta}$$

and

$$u_s = \cos\Gamma \qquad\qquad v_s = \frac{\sin\Gamma}{\rho_s}$$

Equations (2.2.8) and (2.2.9) can now be written as

$$p(\tilde{\xi},\tilde{\beta},\eta) = p_s(\tilde{\xi},\tilde{\beta}) + p_1(\tilde{\xi},\tilde{\beta})\,[\eta - 1] + p_2(\tilde{\xi},\tilde{\beta})\,[\eta^2 - 1] \qquad (2.2.10)$$

$$v(\tilde{\xi},\tilde{\beta},\eta) = v_s(\tilde{\xi},\tilde{\beta}) + v_1(\tilde{\xi},\tilde{\beta})\,[\eta - 1] \qquad\qquad\qquad (2.2.11)$$

where

$$p_1 = \frac{\Psi_s u_s \kappa_\xi}{h_\beta}$$

$$p_2 = -\frac{\Psi_s v_s \tan\Gamma}{2h_\beta}(\kappa_\xi + \kappa_\beta)$$

$$v_1 = \frac{\Psi_s v_s}{h_\beta \cos\Gamma}(\kappa_\xi + \kappa_\beta)$$

The pressure and normal component of velocity can now be found explicitly along a line normal to the shock surface, since all variables in Eqs. (2.2.10) and (2.2.11) are evaluated on the shock. Keep in mind that Eqs. (2.2.10) and (2.2.11) are approximate.

2.2.3 Other Relations

The energy equation for steady, adiabatic, inviscid flow reduces to the simple relation that the total enthalpy of the flow is constant:

$$H = h + \frac{1}{2}(u^2 + v^2) = H_\infty \qquad (2.2.12)$$

Also, for inviscid equilibrium or frozen flow, the post-shock entropy is constant along a streamline. This may be expressed as

$$S = S(\Psi, \beta) \qquad (2.2.13)$$

whereas the equations of state are of the form

$$\rho = \rho(p, S) \qquad h = h(p, S) \qquad (2.2.14)$$

The distance from the shock surface to the body is calculated by integrating Eq. (2.2.2) and noting that the geometric factor $\mathcal{B}$ is a function of n as given in Appendix B.

This yields a quadratic equation for the distance n_b:

$$n_b - \frac{n_b{}^2 \kappa_\beta}{2} = \frac{\Psi_s}{h_\beta} \int_0^1 \frac{d\eta}{\rho u} \tag{2.2.15}$$

Equations (2.2.10)–(2.2.15) provide expressions for the pressure, density, enthalpy, the velocity components u and v, and shock layer thickness. When combined with the properties at the shock (see Appendix C), they form an inverse method: for an assumed shock shape, the corresponding body shape is calculated.

2.3   Method of Solution

The procedure for solving the approximate inviscid flowfield equations, Eqs. (2.2.10)–(2.2.15), is outlined in this section. Since the method is an inverse one, the shock shape must be changed until the correct body shape is produced. The resulting iteration procedure is handled differently in each region of the flow.

2.3.1   Subsonic-Transonic Region

In the stagnation region of a blunt body traveling at hypersonic speeds, the flow is subsonic and the flowfield equations are elliptic. Thus, the shock shape for the entire subsonic-transonic region must be determined globally.

In this investigation, the blunt nose of the body is represented by a longitudinal conic section with an elliptical cross section as

$$\bar{r} = \bar{f}(\bar{x}, \bar{\phi})$$
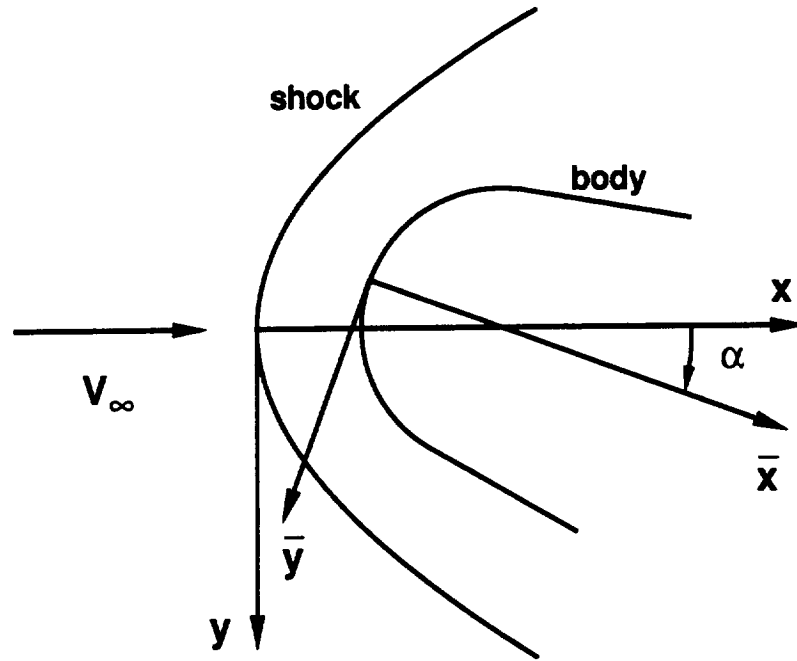
Figure 2.5. Shock and body axes.

where

$$\bar{f}^2(\bar{B}\cos^2\bar{\phi} + \sin^2\bar{\phi}) = 2\bar{x} - \bar{b}\bar{x}^2 \qquad (2.3.1)$$

and the bars indicate that the conic section parameters and coordinates refer to the body with $e_{\bar{x}}$ aligned with the body axis and not the wind axis (see Fig. 2.5). The nondimensional nose radius in the $\bar{x} - \bar{z}$ plane is equal to unity. The parameter $\bar{B}$ governs the ellipticity of the body cross section and for $\bar{B} = 1$, the shape is axisymmetric. The parameter $\bar{b}$ determines the longitudinal shape of the body. Values of $\bar{b}$ greater than zero produce ellipsoids, equal to zero produce a paraboloid, and less than zero produce hyperboloids. A value of $\bar{b}$ equal to one produces a sphere provided $\bar{B}$ is also equal to one.

Van Dyke and Gordon [25] suggest that a conic-section body shape produces a

shock surface that can also be described by a conic section. Therefore, represent the three-dimensional shock surface in the subsonic-transonic region by three longitudinal conic sections blended in the circumferential direction with an ellipse as

$$r = f(x, \phi)$$

where

$$f^2[B(x)\cos^2\phi + \sin^2\phi] + fC(x)\cos\phi = D(x) \qquad (2.3.2)$$

$$B(x) = \frac{f_2^2}{f_1 f_3}$$

$$C(x) = B(x)(f_3 - f_1)$$

$$D(x) = f_2^2$$

and

$$f_k^2 + b_k x^2 - 2c_k x + 2d_k x f_k = 0 \qquad k = 1, 2, 3 \qquad (2.3.3)$$

The index k refers to the 0, 90, and 180 deg meridional planes, respectively, in the wind-oriented system. Cheatwood and DeJarnette [26] follow a similar approach in curve-fitting body geometries. One advantage to this approach is that parameters are added by blending more conic sections with additional elliptic arcs. A limitation of using this shock shape is that the sonic line must remain on the blunted nose. On very blunt geometries (e.g. 60 deg sphere-cone), the sonic line is located at the end of the afterbody and the shock contains inflections in the axial direction. This shock fit does not allow for inflections.

The parameter b governs the shape of the conic section in the same manner as the body parameter $\bar{b}$. The parameter c determines the scale of the shock relative to the body and the parameter d represents the rotation of the conic section. The requirement that the shock curvature at the origin is continuous in the planes of symmetry ($\phi = 0, 180$ deg) leads to the constraint that

$$c_3 = c_1$$

Additional constraints are placed on the coefficient d:

$$d_3 = -d_1 \qquad\qquad d_2 = 0$$

These restrictions imply that the shock shape in the windward ($\phi = 0$ deg) and leeward ($\phi = 180$ deg) planes of symmetry may be rotated, but there is no rotation of the shock shape in the side ($\phi = 90$ deg) meridional plane. Thus, the total number of parameters governing the shock surface is reduced from nine to six.

The iteration procedure for determining the six shock surface parameters is as follows:

1. Assume initial values for the six shock shape parameters b_1, b_2, b_3, c_1, c_2, and d_1. For an axisymmetric flow, the only parameters are b_1 and c_1.

2. Determine initial values for the shock line variables $(x, r, \phi, \sin\Gamma, h_\beta, \Psi_s)$ from the limiting form of the shock shape, Eqs. (2.3.2) and (2.3.3), in the stagnation region. The initial values are given in Appendix D.

3. Calculate the shock standoff distance on the stagnation line (origin of the wind-oriented coordinate system) from the limiting form of Eqs. (2.2.10)–(2.2.15) on the stagnation line. Its derivation is also outlined in Appendix D.

4. Integrate the shock line variables along three shock lines ($\beta = 0, 90, 180$ deg) from the stagnation region to the end of the subsonic region. Only one shock line is needed if the flow is axisymmetric. The derivatives of the shock line variables are obtained from Eqs. (2.1.2), (2.2.3), (B.6), (B.12), and (B.17) as

$$\frac{\partial x}{\partial s} = \cos\Gamma \qquad (2.3.4)$$

$$\frac{\partial r}{\partial s} = \sin\Gamma \cos\delta_\phi \qquad (2.3.5)$$

$$\frac{\partial \phi}{\partial s} = -\frac{\sin\Gamma \sin\delta_\phi}{r} \qquad (2.3.6)$$

$$\frac{\partial \sin\Gamma}{\partial s} = -\kappa_\xi \cos\Gamma \qquad (2.3.7)$$

$$\frac{\partial h_\beta}{\partial s} = h_\beta \kappa_\beta \tan\Gamma \qquad (2.3.8)$$

$$\frac{\partial \Psi_s}{\partial s} = h_\beta \sin\Gamma \qquad (2.3.9)$$

where

$$\frac{\partial}{\partial s} \equiv \frac{1}{h_\xi}\frac{\partial}{\partial \xi}$$

To insure that the axial location is the same for each shock line, transform the distance along a shock line, s, to a time-like variable along a shock line, t, using

$$\frac{\partial}{\partial t} = \frac{x}{\cos\Gamma}\frac{\partial}{\partial s}$$

This transformation allows derivatives in the ϕ-direction to be found more conveniently and also results in well-behaved derivatives near the origin. The

integration scheme is detailed in Appendix E. Shock angles and curvatures are calculated from the assumed shock surface using Eqs. (2.1.2), (B.6), (B.7), and (B.17).

5. After each integration step, calculate the shock standoff distance n_b for each shock line using the shock layer equations. A geometric distance $n_{b_{geo}}$ is also found by projecting a normal line from the assumed shock surface to the known body shape.

6. Stop the integration when the surface ($\Psi = 0$) Mach number is supersonic on each shock line. A typical value for M_b is 1.05.

7. Compute the error between the calculated body shape and the known body shape for each of the three shock lines. Errors in body position and slope are estimated at the last integration step and are given by

$$e_{1_k} = \left(\frac{n_b}{n_{b_{geo}}} \right)_{isub} - 1 \qquad e_{2_k} = \left(\frac{\nabla n_b}{\nabla n_{b_{geo}}} \right)_{isub} - 1$$

where ∇ is the backwards difference operator and *isub* represents the last integration step.

8. Use the error in the body shape to obtain improved shock surface parameters from a quasi-Newton nonlinear equations solver. The above steps are then repeated until the error between the calculated and known body shape is within a prescribed tolerance. Consequently, the calculated body shape is constrained to match the given body shape at only a few points.

9. Once the shock surface has been determined, the shock variables are integrated along all shock lines (as determined by the user) from the stagnation region to the end of the subsonic-transonic region.

2.3.2 Supersonic Region

Once past the transonic region, the flow is totally supersonic and a marching scheme is well posed. The shock surface and resulting shock lines from the transonic region form a starting solution for the marching procedure. The general marching procedure is as follows:

1. Starting at x_i, predicted values for the shock variables $(r, \phi, \sin\Gamma, h_\beta, \Psi_s)$ are obtained at x_{i+1} for each shock line using Eqs. (2.3.5)-(2.3.9). In the supersonic region, it is not necessary to use the time-like variable t. Instead, transform to the axial coordinate x using

$$\frac{\partial}{\partial x} = \frac{1}{\cos\Gamma}\frac{\partial}{\partial s}$$

2. The angle δ_ϕ and the derivative $\frac{\partial\sigma}{\partial\beta}$ are computed using the predicted values of the shock radius. These derivatives may be calculated from finite differences in the circumferential direction. Smoother derivatives are obtained by fitting the shock radii with an ellipse in a least squares sense and then differentiating the ellipse.

3. On each shock line, the local shock curvature κ_ξ is varied in Eqs. (2.2.10)-(2.2.15) until the calculated shock layer thickness matches the geometric thick-

ness. Convergence usually requires two or three iterations with the secant method.

4. The above steps are repeated for the corrector step using the new values for the shock curvature κ_ξ.

5. Upon completion of the corrector step at x_{i+1} for each shock line, predicted values for the shock variables are obtained at x_{i+2} and the entire process is repeated.

3 Viscous Analysis

In this chapter, the analysis of the viscous region near the body surface is detailed. An overview of the method is given in Ref. [27]. Because the viscous region is assumed to be thin in comparison with the shock layer, the appropriate governing equations are the 3-D boundary layer equations. These equations may be found in most textbooks concerning viscous flow (such as Ref. [28]), so they are not repeated here. Properties at the boundary layer edge are obtained from the inviscid solution previously described.

3.1 Axisymmetric Analog

The 3-D boundary layer analysis is simplified by using the axisymmetric analog [13] as is done in most engineering aerothermal methods. The full equations are first written in a inviscid surface streamline coordinate system. The crossflow velocity component tangent to the surface but normal to the streamline is then assumed to be equal to zero throughout the boundary layer. This assumption, which is similar to the approximation of $w = 0$ used in the outer inviscid region, is accurate when the streamline curvature is small [29] or when the wall is highly cooled [30]. The 3-D boundary layer equations reduce to their axisymmetric form, provided the distance along the streamline is substituted for the surface distance and the scale factor describing the divergence of the streamlines is interpreted as the axisymmetric body radius. This approach allows any axisymmetric boundary layer method to be used.

3.2   Inviscid Surface Streamlines

Before applying the axisymmetric analog, inviscid surface streamlines are computed from the approximate inviscid solution. These body streamlines may be calculated from the surface pressure distribution [9] or from the velocity components [11]. The approximate inviscid method used here predicts accurate surface pressures, but the direction of the velocity on the surface is not accurate. Therefore, in the present analysis, streamlines are calculated from the surface pressures.

A streamline coordinate system [9] $(\bar{\xi}, \bar{\beta}, \bar{n})$ is defined in which $\bar{\xi}$ and $\bar{\beta}$ are coordinates of a point on the body surface and $\bar{n}$ is the distance normal to the body. The bars indicate the coordinates are relative to the body, rather than the shock. Differential arc lengths along each coordinate direction at the body are $h_{\bar{\xi}} d\bar{\xi}$, $h_{\bar{\beta}} d\bar{\beta}$, and $d\bar{n}$ where $h_{\bar{\xi}}$ and $h_{\bar{\beta}}$ are scale factors for the corresponding coordinates.

If the body surface is represented by $r = f_b(x, \phi)$ in wind axes with the axial coordinate parallel to the freestream velocity and passing through the stagnation point, the unit vector normal (outward) to the body surface is given by Eq. (2.1.3) as

$$\mathbf{e}_{\bar{n}} = -\sin\Gamma_b \, \mathbf{e}_x + \cos\Gamma_b \, \cos\delta_{\phi_b} \, \mathbf{e}_r - \cos\Gamma_b \, \sin\delta_{\phi_b} \, \mathbf{e}_\phi \qquad (3.2.1)$$

The body angles are defined in the same fashion as the shock angles, so that

$$\tan\delta_{\phi_b} = \frac{1}{f_b} \frac{\partial f_b}{\partial \phi} \qquad \tan\Gamma_b = \frac{\partial f_b}{\partial x} \cos\delta_{\phi_b} \qquad \sigma_b = \phi - \delta_{\phi_b}$$

The body geometry in the wind axes is related to the body axes in Appendix F.

The tangential unit vectors on the surface, $\mathbf{e}_{\bar{\xi}}$ and $\mathbf{e}_{\bar{\beta}}$, are similar to the tangential

unit vectors at the shock. The vector $\mathbf{e}_{\bar{\xi}}$ is in the direction of a surface streamline and $\mathbf{e}_{\bar{\beta}}$ is perpendicular to the streamline. From Ref. [9] they are given as

$$\mathbf{e}_{\bar{\xi}} = \cos\bar{\theta}\mathbf{e}_{\bar{s}} + \sin\bar{\theta}\mathbf{e}_{\bar{t}} \qquad (3.2.2)$$

$$\mathbf{e}_{\bar{\beta}} = -\sin\bar{\theta}\mathbf{e}_{\bar{s}} + \cos\bar{\theta}\mathbf{e}_{\bar{t}} \qquad (3.2.3)$$

where

$$\mathbf{e}_{\bar{s}} = \cos\Gamma_b\,\mathbf{e}_x + \sin\Gamma_b\,\cos\delta_{\phi_b}\,\mathbf{e}_r - \sin\Gamma_b\,\sin\delta_{\phi_b}\,\mathbf{e}_\phi \qquad (3.2.4)$$

$$\mathbf{e}_{\bar{t}} = \sin\delta_{\phi_b}\,\mathbf{e}_r + \cos\delta_{\phi_b}\,\mathbf{e}_\phi \qquad (3.2.5)$$

and the angle $\bar{\theta}$ represents the orientation of the surface streamlines with respect to $\mathbf{e}_{\bar{s}}$. Note that the vectors $\mathbf{e}_{\bar{s}}$ and $\mathbf{e}_{\bar{t}}$ are identical in form to the unit vectors $\mathbf{e}_{\bar{\xi}}$ and $\mathbf{e}_\beta$ defined earlier.

The orientation of the inviscid surface streamlines, given by $\bar{\theta}$, is found by applying the momentum equations along the body surface in conjunction with the pressure distribution generated by the inviscid solution. From Eq. (2.2.4), the momentum equations may be written as

$$\frac{D\mathbf{V}}{Dt} = -\frac{1}{\rho}\nabla p$$

where $\frac{D}{Dt}$ represents the time derivative along a streamline and is equivalent to $\mathbf{V}\cdot\nabla\mathbf{V}$ for steady flow. Writing this equation in the orthogonal streamline coordinates and substituting

$$\frac{D\mathbf{V}}{Dt} = \frac{V}{h_{\bar{\xi}}}\frac{\partial\mathbf{V}}{\partial\bar{\xi}} \qquad\qquad \mathbf{V} = \bar{u}\mathbf{e}_{\bar{\xi}}$$

gives

$$\frac{\bar{u}}{h_{\bar{\xi}}}\frac{\partial \bar{u}}{\partial \bar{\xi}}\mathbf{e}_{\bar{\xi}} + \frac{\bar{u}^2}{h_{\bar{\xi}}}\frac{\partial \mathbf{e}_{\bar{\xi}}}{\partial \bar{\xi}} = -\frac{1}{\rho}\left(\frac{1}{h_{\bar{\xi}}}\frac{\partial p}{\partial \bar{\xi}}\mathbf{e}_{\bar{\xi}} + \frac{1}{h_{\bar{\beta}}}\frac{\partial p}{\partial \bar{\beta}}\mathbf{e}_{\bar{\beta}} + \frac{\partial p}{\partial n}\mathbf{e}_{\bar{n}}\right) \qquad (3.2.6)$$

By taking the scalar product of Eq. (3.2.6) with $\mathbf{e}_{\bar{\beta}}$ and substituting the unit vectors from Eqs. (3.2.2)–(3.2.5), the following expression is obtained:

$$\frac{1}{h_{\bar{\xi}}}\frac{\partial \bar{\theta}}{\partial \bar{\xi}} = -\frac{\sin\Gamma_b}{h_{\bar{\xi}}}\frac{\partial \sigma_b}{\partial \bar{\xi}} - \frac{1}{\rho_b \bar{u}_b^2}\frac{1}{h_{\bar{\beta}}}\frac{\partial p_b}{\partial \bar{\beta}} \qquad (3.2.7)$$

The derivative of the scale factor $h_{\bar{\beta}}$ can be determined in the same manner as the derivative of the scale factor h_β. Referring to Eq. (B.11), the derivative is

$$\frac{\partial h_{\bar{\beta}}}{\partial \bar{\xi}} = h_{\bar{\xi}}\frac{\partial \mathbf{e}_{\bar{\xi}}}{\partial \bar{\beta}} \cdot \mathbf{e}_{\bar{\beta}}$$

Substituting Eqs. (3.2.2)–(3.2.5) yields

$$\frac{1}{h_{\bar{\xi}}}\frac{\partial \left(\ln h_{\bar{\beta}}\right)}{\partial \bar{\xi}} = \frac{1}{h_{\bar{\beta}}}\frac{\partial \bar{\theta}}{\partial \bar{\beta}} + \frac{\sin\Gamma_b}{h_{\bar{\beta}}}\frac{\partial \sigma_b}{\partial \bar{\beta}} \qquad (3.2.8)$$

Equations (3.2.7) and (3.2.8) may be integrated along a surface streamline to obtain the streamline direction $\bar{\theta}$ and the scale factor $h_{\bar{\beta}}$, respectively. Although these body streamlines can be determined after the inviscid solution has already been calculated, it is more convenient to compute the inviscid flowfield and the surface streamlines simultaneously. This simplifies the coupling of the inviscid and boundary layer regions. Before applying these equations along shock coordinates, transformation operators relating derivatives with respect to the the streamline coordinates $(\bar{\xi}, \bar{\beta})$ to derivatives with respect to the shock coordinates (ξ, β) are needed. In the approximate inviscid method, the curvilinear coordinate system is assumed to be orthogonal throughout the shock layer. This assumption simplifies the analysis but does

not change the form of the approximate pressure and velocity relations, Eqs. (2.2.10) and (2.2.11), since the flowfield variables are evaluated at the shock (where the co-ordinate system is in fact orthogonal). At the body surface, however, the shock coordinate system is nonorthogonal and the correct coordinate directions need to be considered. Using the coordinate directions at the surface, the transformation operators are derived in Appendix B and repeated here:

$$\frac{\mathcal{J}_b}{h_{\bar{\xi}}}\frac{\partial}{\partial\bar{\xi}} = \left(\mathcal{B}_b \mathbf{e}_{\bar{\xi}}\cdot\mathbf{e}_{\xi} - \mathcal{D}_b \mathbf{e}_{\bar{\xi}}\cdot\mathbf{e}_{\beta}\right)\frac{1}{h_{\xi}}\frac{\partial}{\partial\xi} + \left(\mathcal{A}_b \mathbf{e}_{\bar{\xi}}\cdot\mathbf{e}_{\beta} - \mathcal{D}_b \mathbf{e}_{\bar{\xi}}\cdot\mathbf{e}_{\xi}\right)\frac{1}{h_{\beta}}\frac{\partial}{\partial\beta} \qquad (3.2.9)$$

and

$$\frac{\mathcal{J}_b}{h_{\bar{\beta}}}\frac{\partial}{\partial\bar{\beta}} = \left(\mathcal{B}_b \mathbf{e}_{\bar{\beta}}\cdot\mathbf{e}_{\xi} - \mathcal{D}_b \mathbf{e}_{\bar{\beta}}\cdot\mathbf{e}_{\beta}\right)\frac{1}{h_{\xi}}\frac{\partial}{\partial\xi} + \left(\mathcal{A}_b \mathbf{e}_{\bar{\beta}}\cdot\mathbf{e}_{\beta} - \mathcal{D}_b \mathbf{e}_{\bar{\beta}}\cdot\mathbf{e}_{\xi}\right)\frac{1}{h_{\beta}}\frac{\partial}{\partial\beta} \qquad (3.2.10)$$

where

$$\mathcal{A}_b = 1 - n_b\kappa_{\xi}$$

$$\mathcal{B}_b = 1 - n_b\kappa_{\beta}$$

$$\mathcal{D}_b = \frac{n_b}{h_{\beta}}\frac{\partial\Gamma}{\partial\beta}$$

$$\mathcal{J}_b = \mathcal{A}_b\mathcal{B}_b - \mathcal{D}_b^2$$

The scalar products may be evaluated from Eq. (2.1.8) and Eqs. (3.2.2)–(3.2.5) as

$$\mathbf{e}_{\bar{\xi}}\cdot\mathbf{e}_{\xi} = \cos\bar{\theta}\mathbf{e}_{\bar{s}}\cdot\mathbf{e}_{\xi} + \sin\bar{\theta}\mathbf{e}_{\bar{t}}\cdot\mathbf{e}_{\xi}$$

$$\mathbf{e}_{\bar{\xi}}\cdot\mathbf{e}_{\beta} = \cos\bar{\theta}\mathbf{e}_{\bar{s}}\cdot\mathbf{e}_{\beta} + \sin\bar{\theta}\mathbf{e}_{\bar{t}}\cdot\mathbf{e}_{\beta} \qquad (3.2.11)$$

$$\mathbf{e}_{\bar{\beta}}\cdot\mathbf{e}_{\xi} = -\sin\bar{\theta}\mathbf{e}_{\bar{s}}\cdot\mathbf{e}_{\xi} + \cos\bar{\theta}\mathbf{e}_{\bar{t}}\cdot\mathbf{e}_{\xi}$$

$$\mathbf{e}_{\bar{\beta}}\cdot\mathbf{e}_{\beta} = -\sin\bar{\theta}\mathbf{e}_{\bar{s}}\cdot\mathbf{e}_{\beta} + \cos\bar{\theta}\mathbf{e}_{\bar{t}}\cdot\mathbf{e}_{\beta}$$

where

$$\mathbf{e}_{\bar{s}} \cdot \mathbf{e}_{\xi} = \cos\Gamma \cos\Gamma_b + \sin\Gamma \sin\Gamma_b \cos(\sigma - \sigma_b)$$

$$\mathbf{e}_{\bar{s}} \cdot \mathbf{e}_{\beta} = -\sin\Gamma_b \sin(\sigma - \sigma_b) \qquad\qquad (3.2.12)$$

$$\mathbf{e}_{\bar{t}} \cdot \mathbf{e}_{\xi} = \sin\Gamma \sin(\sigma - \sigma_b)$$

$$\mathbf{e}_{\bar{t}} \cdot \mathbf{e}_{\beta} = \cos(\sigma - \sigma_b)$$

These operators can be used to calculate the pressure derivative that appears in Eq. (3.2.7). They also allow Eqs. (3.2.7) and (3.2.8) to be integrated with respect to the shock coordinate ξ. The limiting forms of these equations in the stagnation region are derived and given in Appendix G.

3.3 Convective-Heating Equations

The axisymmetric analog allows any axisymmetric boundary layer method to be applied along an inviscid surface streamline. Although the axisymmetric boundary layer equations may be integrated numerically, a set of approximate convective-heating equations developed by Zoby [24] provides accurate surface heating rates with a minimal amount of computational effort. These equations are used here since they are consistent with the approximate nature of the inviscid method described previously. Laminar and turbulent heating rates may be calculated from these relations for both perfect gas and equilibrium flows. Results using this technique have been shown to compare favorably with more detailed methods for both wind tunnel and flight conditions [31, 32, 33]. A complete derivation of the approximate heating equations

is found in Appendix H and their stagnation region values are given in Appendix G.

3.3.1 Laminar Heat Transfer

The laminar heating rates are calculated by first relating the surface skin friction to the momentum thickness Reynolds number. Then a modified Reynolds analogy is used to relate the heat transfer to the skin friction. The surface heat transfer is given by

$$q_{w_L} = 0.22 \left(Re_{\theta_L}\right)^{-1} \left(\frac{\rho^*}{\rho_e}\right) \left(\frac{\mu^*}{\mu_e}\right) \rho_e \bar{u}_e \left(h_{aw} - h_w\right) \left(Pr_w\right)^{-0.6} \tag{3.3.1}$$

where Eckert's reference enthalpy relation [34] is used to account for compressibility effects. The laminar momentum thickness, θ_L, which appears in the momentum thickness Reynolds number, Re_{θ_L}, is given by

$$\theta_L = \frac{0.664 \left(\int_0^{\bar{\xi}} \rho^* \mu^* \bar{u}_e h_{\bar{\beta}}^2 \, h_{\bar{\xi}} \, d\bar{\xi}\right)^{1/2}}{\rho_e \bar{u}_e h_{\bar{\beta}}} \tag{3.3.2}$$

3.3.2 Turbulent Heat Transfer

The turbulent heating rates are computed in a similar fashion as

$$q_{w_T} = c_1 \left(Re_{\theta_T}\right)^{-m} \left(\frac{\rho^*}{\rho_e}\right) \left(\frac{\mu^*}{\mu_e}\right)^m \rho_e \bar{u}_e \left(h_{aw} - h_w\right) \left(Pr_w\right)^{-0.4} \tag{3.3.3}$$

The turbulent momentum thickness is defined by

$$\theta_T = \frac{\left(c_2 \int_0^{\bar{\xi}} \rho^* \mu^{*m} u_e h_{\bar{\beta}}^{c_3} \, h_{\bar{\xi}} \, d\bar{\xi}\right)^{c_4}}{\rho_e \bar{u}_e h_{\bar{\beta}}} \tag{3.3.4}$$

where

$$m = \frac{2}{N+1} \qquad\qquad c_3 = 1 + m$$

$$c_1 = \left(\frac{1}{c_5}\right)^{\frac{2N}{N+1}} \left[\frac{N}{(N+1)(N+2)}\right]^m \qquad c_4 = \frac{1}{c_3}$$

$$c_2 = (1+m)c_1 \qquad\qquad c_5 = 2.2433 + 0.93N$$

and N is computed from a curve fit of axisymmetric nozzle wall data [35] as

$$N = 12.67 - 6.5\log\left(Re_{\theta_T}\right) + 1.21\left[\log\left(Re_{\theta_T}\right)\right]^2$$

Note that the momentum thickness for both laminar and turbulent flows may be numerically integrated in the same manner as the surface streamline variables $\bar{\theta}$ and $h_{\bar{3}}$.

3.3.3   Transition

In the transition region, both the laminar and turbulent values of θ and q_w are calculated. Their distribution is then computed from the weighting function of Dhawan and Narasimha [36] as

$$\theta = \theta_L + w_f\left(\theta_T - \theta_L\right) \qquad\qquad q_w = q_{w_L} + w_f\left(q_{w_T} - q_{w_L}\right)$$

where

$$w_f = 1 - \exp\left(-0.412\xi_{tr}^2\right) \qquad\qquad \xi_{tr} = 4\left(\frac{\bar{s} - \bar{s}_{beg}}{\bar{s}_{end} - \bar{s}_{beg}}\right)$$

and $\bar{s}$ is the distance along the body surface. The beginning and end of transition must be specified in the present approach.

3.3.4   Edge Properties

The laminar and turbulent heating equations given by Eqs. (3.3.1)–(3.3.4) require properties evaluated at the edge of the boundary layer. These edge conditions are

obtained from the approximate inviscid solution. However, care must be taken in determining the correct edge properties. It cannot be assumed that they are equal to the inviscid body values due to the large entropy gradients near the surface. This entropy layer is created by the highly curved shock waves generated by blunt-nosed bodies traveling at hypersonic speeds. The boundary layer grows inside the entropy layer and eventually "swallows" the entropy layer. At that point, the value of the entropy at the boundary layer edge differs significantly from the normal shock value. Thus, the density and velocity at the edge are different than the corresponding surface values.

In this investigation, boundary-layer edge properties are found by interpolating in the approximate inviscid solution a distance away from the wall equal to the boundary layer thickness (see Fig. 3.1). The laminar boundary layer thickness [24, 37] is approximately

$$\left(\frac{\delta}{\theta}\right)_L = 5.55 \tag{3.3.5}$$

whereas the turbulent boundary layer thickness [24, 38] is approximately

$$\left(\frac{\delta}{\theta}\right)_T = N + 1 + \left[\left(\frac{N+2}{N}\frac{h_w}{h_{aw}} + 1\right)\left(1 + 1.29 Pr_w^{1/3}\frac{\bar{u}_e^2}{2h_e}\right)\right] \tag{3.3.6}$$

The procedure involves assuming an edge location and iterating until the assumed edge location matches the edge calculated from Eqs. (3.3.5) or (3.3.6). An additional approximation is made by interpolating in the inviscid solution along a line normal to the shock instead of normal to the body. For thin shock layers, this simplification does not create any significant errors. This approach for computing the boundary
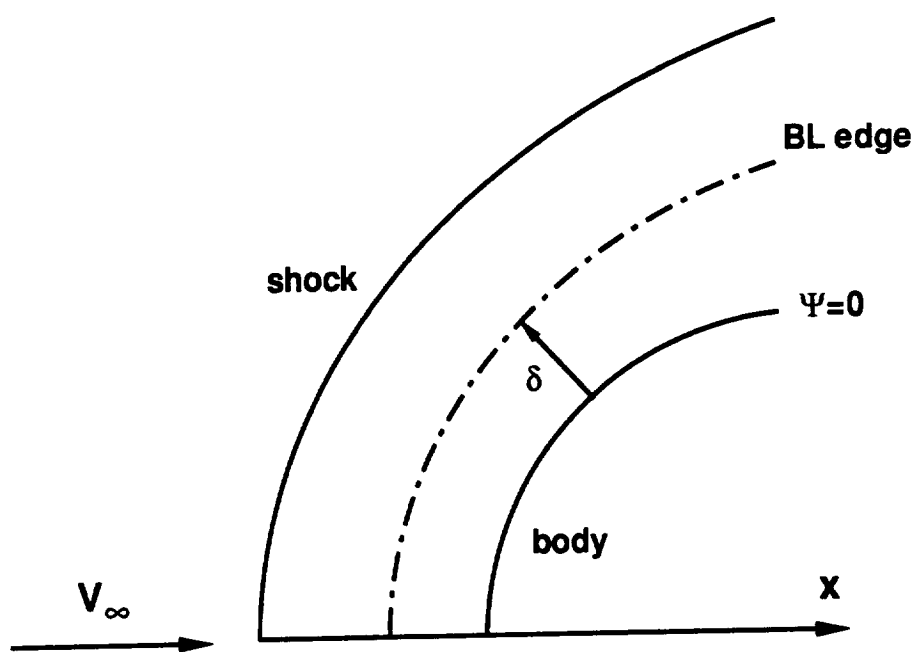
Figure 3.1. Boundary layer edge.

layer edge properties approximately accounts for the effects of entropy layer swallowing. It has been used successfully by several authors for both axisymmetric [24] and 3-D [11, 39, 40] flows.

4 Viscous Interaction

The previous chapters outline the classic boundary layer approach where it is assumed that the viscous region has a negligible effect on the outer inviscid flowfield. As such, the inviscid solution may be obtained independently of the boundary layer. This is a valid assumption for high Reynolds number flows where the boundary layer is indeed very thin compared to the shock layer.

At moderate to low Reynolds numbers and at higher Mach numbers, the boundary layer may occupy a significant portion of shock layer. For these conditions, the interaction between the inviscid and viscous regions is important. The boundary layer displaces the outer inviscid layer thereby creating an increase in the surface pressure. Consequently, this increase in pressure influences the boundary layer and increases the surface heat transfer. This chapter gives the transpiration boundary condition (which accounts for the displacement effect of the boundary layer on the inviscid layer) and describes its implementation. Approximate expressions for the boundary layer displacement thickness are also given.

4.1 Transpiration Boundary Condition

For both viscous and inviscid flows, the continuity equation written in the surface streamline coordinates $(\bar{\xi}, \bar{\beta}, \bar{n})$ is

$$\frac{\partial}{\partial \bar{\xi}}(\rho \bar{u} h_{\bar{\beta}}) + \frac{\partial}{\partial \bar{n}}(\rho \bar{v} h_{\bar{\xi}} h_{\bar{\beta}}) = 0 \qquad (4.1.1)$$

where the axisymmetric analog (i.e. $\bar{w} = 0$) has been used. The streamline geometric factors corresponding to the shock layer geometric factors $\mathcal{A}$ and $\mathcal{B}$ appearing in Eq. (2.2.1) are assumed to be equal to unity across the boundary layer. Multiply Eq. (4.1.1) by $d\bar{n}$ and integrate from the surface to the edge of the boundary layer. For the boundary layer solution where $\bar{v}_b = 0$:

$$(\rho \bar{v} h_\xi h_{\bar{\beta}})_e = -\int_0^\delta \frac{\partial}{\partial \xi}(\rho \bar{u} h_{\bar{\beta}}) \, d\bar{n} \tag{4.1.2}$$

Apply Eq. (4.1.1) to the inviscid solution with injection or suction at the wall to obtain

$$(\rho_i \bar{v}_i h_\xi h_{\bar{\beta}})_e - (\rho_i \bar{v}_i h_\xi h_{\bar{\beta}})_b = -\int_0^\delta \frac{\partial}{\partial \xi}(\rho_i \bar{u}_i h_{\bar{\beta}}) \, d\bar{n} \tag{4.1.3}$$

At the boundary layer edge, set $(\rho_i \bar{v}_i)_e = (\rho \bar{v})_e$. Subtracting Eq. (4.1.3) from Eq. (4.1.2) gives

$$(\rho_i \bar{v}_i h_\xi h_{\bar{\beta}})_b = \int_0^\delta \frac{\partial}{\partial \xi}(\rho_i \bar{u}_i h_{\bar{\beta}} - \rho \bar{u} h_{\bar{\beta}}) \, d\bar{n} = \frac{d}{d\xi} \int_0^\delta (\rho_i \bar{u}_i h_{\bar{\beta}} - \rho \bar{u} h_{\bar{\beta}}) \, d\bar{n}$$

By assuming the absence of an entropy layer ($\rho_i \bar{u}_i \approx \rho_e \bar{u}_e$) and substituting the definition of the displacement thickness given by Eq. (H.3), this relation can be simplified as

$$(\rho_i \bar{v}_i h_\xi h_{\bar{\beta}})_b = \frac{d}{d\xi}(\rho_e \bar{u}_e h_{\bar{\beta}} \delta^*) \tag{4.1.4}$$

where δ^* is the boundary layer displacement thickness. The quantity $(\rho_i \bar{v}_i h_\xi h_{\bar{\beta}})_b$ represents the mass transpired through the body surface for the inviscid flow to account for the mass defect in the boundary layer. Equation (4.1.4) is referred to as the *transpiration boundary condition*. For inviscid CFD methods whose surface

boundary conditions consist of specifying the normal velocity component at the wall. Eq. (4.1.4) is the appropriate boundary condition for viscous interaction. However, the approximate inviscid method described in this investigation defines the body surface in terms of $\Psi = 0$ and the distance $n = n_b$ from the shock.

Return to Eq. (4.1.1) and define the stream functions $\bar{\Psi}$ and $\bar{\Phi}$ such that if $\bar{\Phi} = \bar{\beta}$,

$$\frac{\partial \bar{\Psi}}{\partial \bar{n}} = \rho_i \bar{u}_i h_{\bar{\beta}} \tag{4.1.5}$$

$$\frac{\partial \bar{\Psi}}{\partial \bar{\xi}} = -\rho_i \bar{v}_i h_{\bar{\xi}} h_{\bar{\beta}} \tag{4.1.6}$$

Comparing Eq. (4.1.6) with Eq. (4.1.4) gives

$$\bar{\Psi}_b = -\rho_e \bar{u}_e h_{\bar{\beta}} \delta^* \tag{4.1.7}$$

This equation gives the transpiration boundary condition in terms of the stream function defined in the streamline coordinate system. The boundary condition with respect to $\bar{n}$ is found by integrating Eq. (4.1.5) and assuming the absence of an entropy layer near the body. This boundary condition becomes

$$\bar{n}_{\Psi=0} = \delta^* \tag{4.1.8}$$

which states that the boundary layer displaces the outer inviscid flow a distance equal to δ^*, thereby creating an "effective" body shape. This is an anticipated result and is the most common way of accounting for the viscous interaction. Equations (4.1.4), (4.1.7), and (4.1.8) are equivalent boundary conditions.

The boundary condition in $\bar{n}$ is applied in the approximate inviscid method by
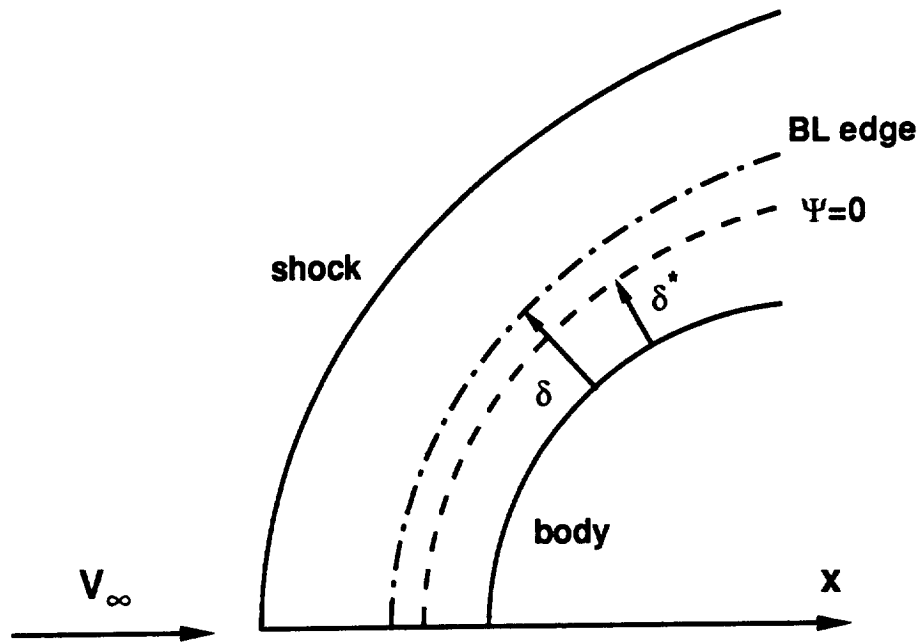
Figure 4.1. Boundary layer displacement thickness.

first assuming that $e_{\bar{n}} \approx -e_n$. This leads to

$$\bar{n} = n_b - n$$

Substituting Eq. (4.1.8) gives the shock layer thickness as

$$n_b = (n_b)_{\Psi=0} + \delta^* \tag{4.1.9}$$

In Fig. 4.1, the effective body is represented by $\Psi = 0$ and is located a distance equal to δ^* above the actual body. The distance $(n_b)_{\Psi=0}$ is the distance from the shock to $\Psi = 0$. The distance n_b is the total distance from the shock to the actual body. Thus, the transpiration boundary condition is included in the approximate inviscid method by adding the boundary layer displacement thickness to the shock layer thickness previously calculated. It is this distance that is matched to the geometric distance

from the shock to the body. Note that the boundary layer edge is now located a distance equal to $\delta - \delta^*$ above the effective body.

The iteration procedure for including the viscous interaction is handled differently in the subsonic and supersonic regions. Referring to Sec. 2.3.1, in the subsonic region, the displacement thickness is calculated after each integration step and included in the total shock layer thickness as stated by Eq. (4.1.9). The remaining procedure is the same. In the supersonic region, a predicted value for the displacement thickness is obtained from a linear extrapolation of the previous values. It is held constant as the local shock curvature is varied. An updated value for the displacement thickness is then computed for the corrector step. If the displacement thickness changes significantly from the predicted value, then additional corrector steps are necessary.

4.2 Displacement Thickness

To apply the transpiration boundary condition, expressions for the boundary layer displacement thickness and total thickness are needed. For laminar flow, Ref. [37] gives the distances as

$$\frac{\delta}{\theta} = \frac{\delta_{tr}}{\theta_{tr}} + \frac{\bar{u}_e^2}{2h_e}(H_{tr} + 1)$$

and

$$\frac{\delta^*}{\theta} = H_{tr} + \frac{\bar{u}_e^2}{2h_e}(H_{tr} + 1)$$

where H_{tr} is a transformed form factor (see Appendix H) for low speed flows. In computing the boundary layer thickness, Zoby [24] assumes $H_{tr} = -1$ and $\frac{\delta_{tr}}{\theta_{tr}} = 5.55$.

However, this choice for the form factor leads to a negative displacement thickness. This is unrealistic at some flow conditions. In this investigation, it is assumed that

$$H_{tr} = 0$$

which corresponds to a cold wall with zero pressure gradient (flat plate) in the analysis of Ref. [37]. Simplifying the above expressions yields

$$\left(\frac{\delta}{\theta}\right)_L = 5.55 + \frac{\bar{u}_e^2}{2h_e} \tag{4.2.1}$$

and

$$\left(\frac{\delta^*}{\theta}\right)_L = \frac{\bar{u}_e^2}{2h_e} \tag{4.2.2}$$

The turbulent displacement thickness corresponding to Eq. (3.3.6) is obtained from Ref. [38] as

$$\left(\frac{\delta^*}{\theta}\right)_T = -1 + \left[\left(\frac{N+2}{N}\frac{h_w}{h_{aw}} + 1\right)\left(1 + 0.97Pr_w^{1/3}\frac{\bar{u}_e^2}{2h_e}\right)\right] \tag{4.2.3}$$

5 Results and Discussion

Results obtained with the present technique are presented in this chapter. Inviscid, boundary layer, and interactive inviscid-boundary layer solutions are computed at perfect gas and laminar conditions. Equilibrium-air calculations for laminar and turbulent flow are also shown. Surface pressure and heating rate distributions along with the corresponding shock shapes are examined to demonstrate the capability and accuracy of the present method for blunted axisymmetric and 3-D body shapes at angle of attack. Comparisons are made with experimental data as well as with flight data. Inviscid solutions are compared with the results of two inviscid CFD methods: HALIS [41] and STEIN [42]. Viscous solutions are compared with the results of a VSL method [3], a NS method (LAURA) [1], and an approximate VSL method (AVSL) [43]. The results from two engineering techniques, AEROHEAT [8, 9] and INCHES [10], are also shown where appropriate.

Results are presented in nondimensional form (see Appendix A) in the body-oriented coordinate system $(\bar{x}, \bar{\phi})$. The windward plane is given by $\bar{\phi} = 0$ deg and the leeward plane is located at $\bar{\phi} = 180$ deg. Distances are referenced to the nose radius of the body in the $\bar{x}$-$\bar{z}$ plane, $R_{\bar{z}}$.
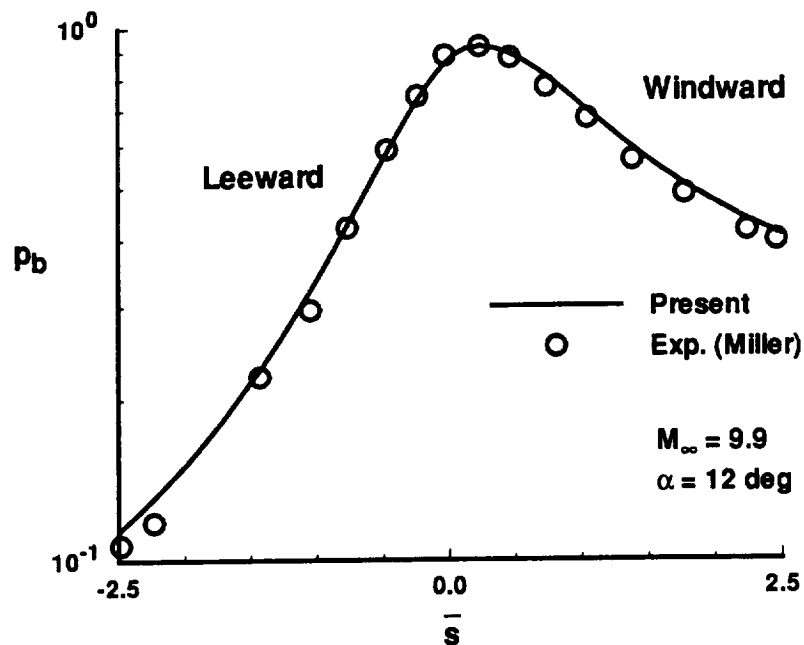
Figure 5.1. Body pressure comparison in planes of symmetry for paraboloid.

5.1   Inviscid Solutions

Inviscid solutions are calculated for a paraboloid and blunted 1.5:1 elliptic cone at angle of attack. Results over spherically-blunted cones at angle of attack using the inviscid version of the present technique [20, 21] have been documented and are not repeated here. All solutions are computed using 21 points in the η direction. These points are clustered to resolve the entropy layer near the body surface.

Paraboloids

Surface pressures and shock shapes for a paraboloid at 12 deg angle of attack are presented in Figs. 5.1 and 5.2, respectively. Experimental results [44] are presented at freestream Mach numbers of 9.9 for the surface pressures and 5.73 for the shock shape. Although a paraboloid is axisymmetric, the shock shape produced in the nose region
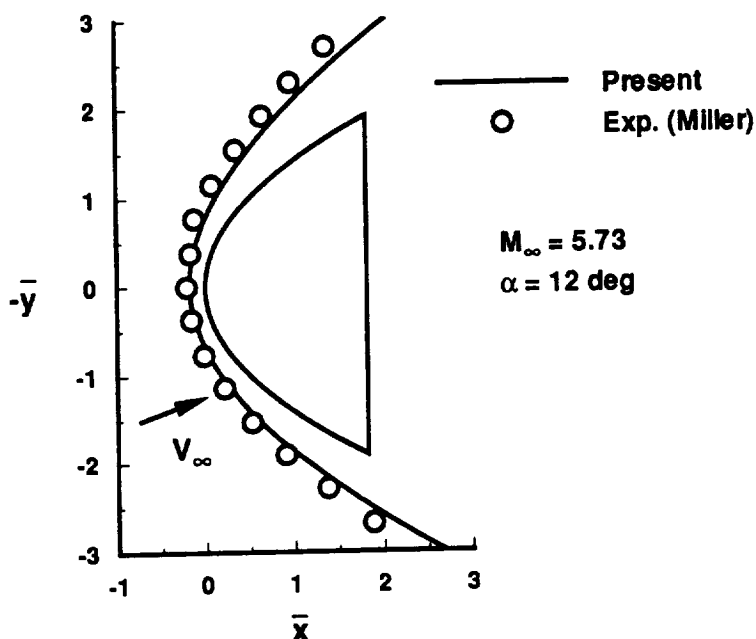
Figure 5.2. Shock shape comparison in planes of symmetry for paraboloid.

is fully three-dimensional when the body is at angle of attack. Three longitudinal

conic sections are blended with an ellipse as described in Sec. 2.3.1 to produce the

shock shape in the nose region. Six iterations using the quasi-Newton nonlinear

equations solver are required for convergence. Good agreement (within 8 percent)

in surface pressures between the present method and the experimental data [44] is

shown in Fig. 5.1. In Fig. 5.2, the calculated shock lies slightly closer to the body

than does the experimentally determined shock shape, but the agreement is good.

Comparisons in Ref. [44] at 0 deg angle of attack were made with the axisymmetric

Maslen technique of Zoby and Graves [15], and a similar result was observed.

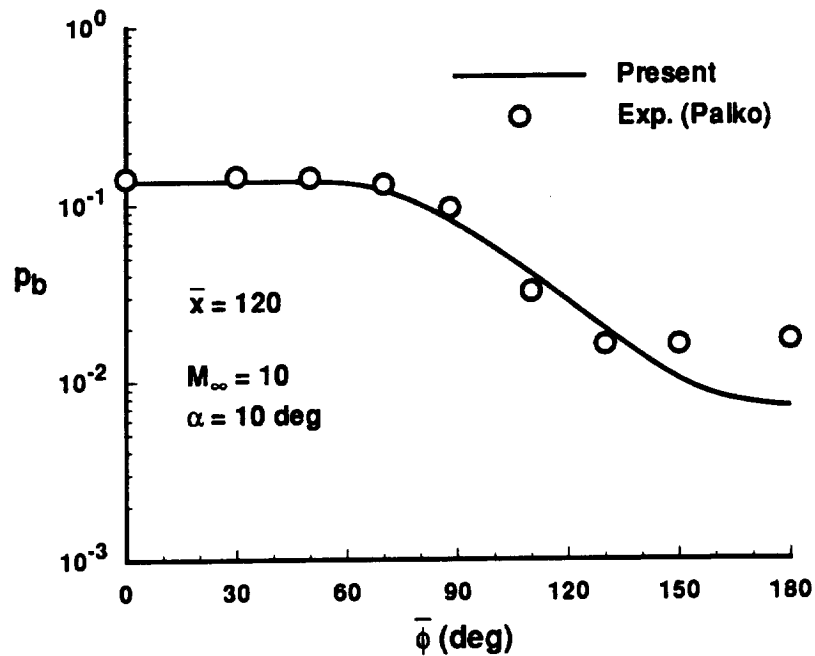**Figure 5.3.** Circumferential body pressure comparison for 1.5:1 elliptic cone.

Blunted Elliptic Cones

Surface pressures over an elliptic cone with a cone half-angle of 10.26 deg in the windward plane and an ellipticity of 1.5 are shown in Fig. 5.3. The experimental data [45] displayed are for a pointed elliptic cone. For the calculations, a very small nose radius is assumed for the elliptic cone. Circumferential pressures are shown for a position far downstream ($\bar{x} = 120$), where the surface pressures should approach sharp cone values. At 10 deg angle of attack, the agreement between the experimental and calculated pressures is excellent except near the leeside region ($\bar{\phi} > 140$ deg) as shown in Fig. 5.3. Since viscous effects are more pronounced in the leeward region, an inviscid method is not appropriate for calculations in this area anyway.

Numerical solutions for this case were also computed using two Euler equation

solvers. The first, a time-dependent solution of the inviscid equations (HALIS) [41], is used to compute the blunt nose region of the elliptic cone. This provides a starting plane for the second Euler equation solver which computes the supersonic region of the flow with a marching procedure (STEIN) [42]. The following run-time comparisons are for a CRAY-2 supercomputer. For a length of 2 nose radii, HALIS requires 1000 iterations for convergence and a time of 120 CPU (central processing unit) sec for a grid consisting of 31 points in the streamwise direction, 37 points in the circumferential direction, and 11 points across the shock layer. For the solution downstream of the nose, STEIN requires 105 CPU sec to advance 50 nose radii using 575 marching steps with a grid consisting of 37 points in the circumferential direction and 21 points across the shock layer. The present technique requires less than 1 CPU sec to advance 50 nose radii using 65 marching steps, 19 points around the circumference of the shock, and 21 points across the shock layer. These comparisons demonstrate the approximate inviscid technique is much faster than more exact CFD methods for 3-D nose shapes.

The surface pressure distribution in the windward plane of symmetry of the elliptic cone is shown in Fig. 5.4 for 10 deg angle of attack and a Mach number of 10. The results of the present method are in excellent agreement with the STEIN solution. Circumferential pressure distributions in the nose region and on the conical afterbody are given in Fig. 5.5 for the elliptic cone at angle of attack. Good agreement is noted except on the leeward side ($\bar{\phi} > 90$ deg).
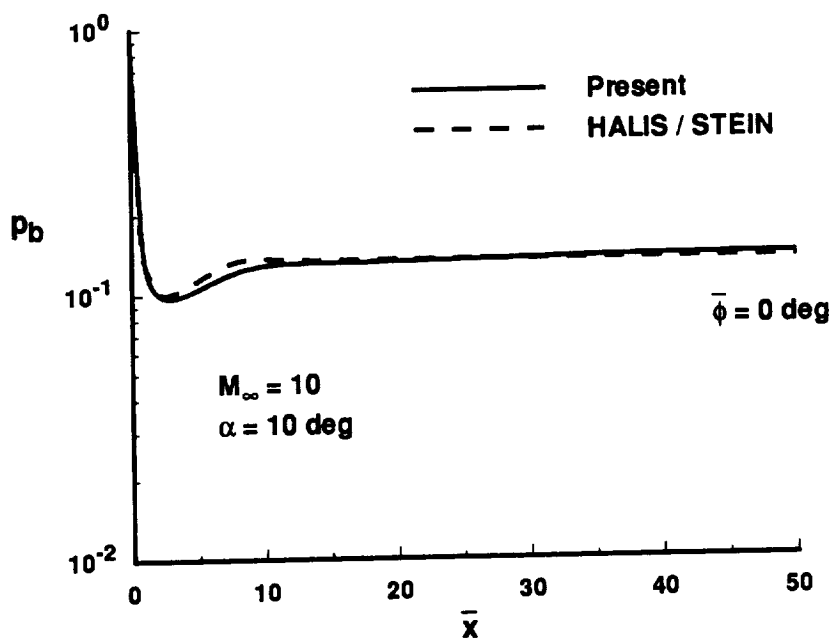
Figure 5.4. Axial body pressure comparison for blunted 1.5:1 elliptic cone.
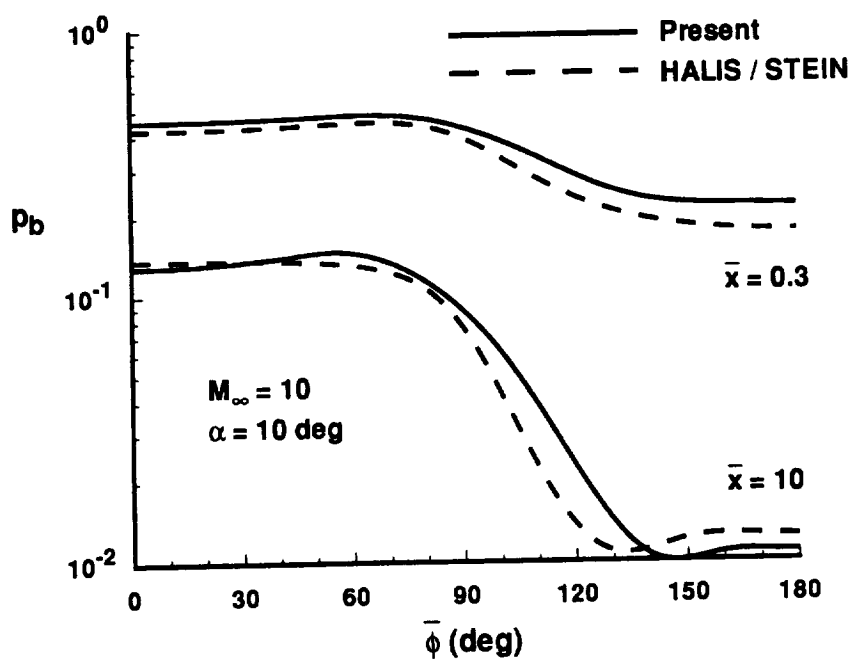

Figure 5.5. Circumferential body pressure comparison for blunted 1.5:1 elliptic cone.

5.2 Boundary Layer Solutions

Surface heating rates are presented for perfect gas and laminar conditions over spherically-blunted and blunted 3-D elliptic cones at angle of attack to evaluate the accuracy of the inviscid-boundary layer technique as described in Chaps. 2 and 3. The Reynolds number is relatively high so that the boundary layer is thin and the viscous interaction may be neglected. Viscous interaction effects are examined later.

Spherically-Blunted Cones

Computed laminar surface heating rates are presented for the windward plane of a 15 deg spherically-blunted cone at angles of attack of 5 and 10 deg. The freestream conditions are $M_\infty = 10.6$, $\rho_\infty = 0.00973\ kg/m^3$, and $T_\infty = 47.3\ K$. The wall temperature is $T_w = 300\ K$. Results of the present method are compared with results of an engineering aerothermal method AEROHEAT [8, 9] and experimental data [46] for a nose radius of $R_{\bar{z}} = 0.0279\ m$. Good agreement (within 10 percent) between the results of the present method and the experimental data is shown in Figs. 5.6 and 5.7. The AEROHEAT results fail to predict the correct magnitude of the surface heating as well as the local maximum in the heating. These discrepancies can be attributed to the modified Newtonian pressure distribution and approximate streamlines used in AEROHEAT. Circumferential heating rates are presented in Figs. 5.8 and 5.9 at two axial locations on the blunted cone for angles of attack of 5 and 10 deg. The comparison of the experimental and predicted heating rates is seen to be good at both

Figure 5.6. Axial heat transfer comparison for 15 deg sphere-cone, $R_{\bar{z}} = 0.0279$ m.

Figure 5.7. Axial heat transfer comparison for 15 deg sphere-cone, $R_{\bar{z}} = 0.0279$ m.
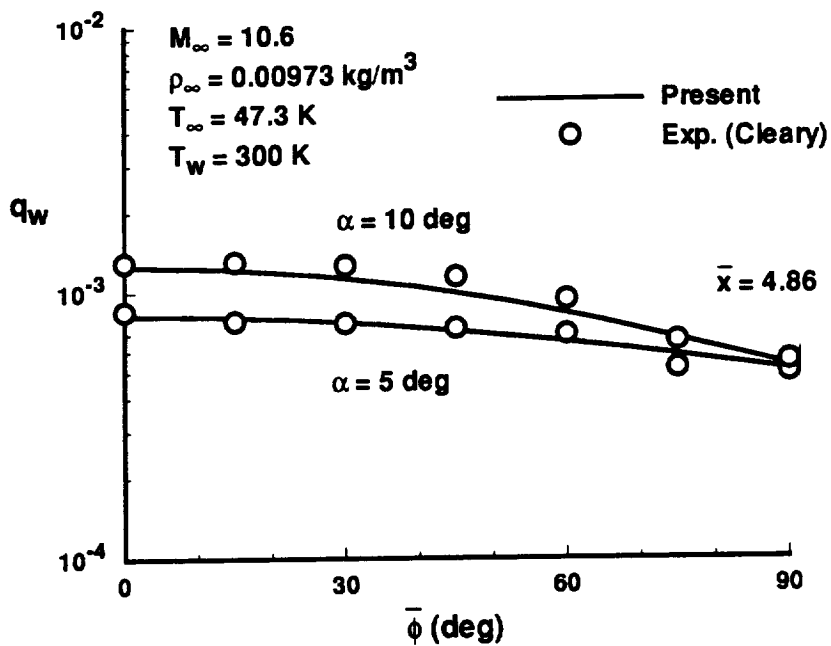
Figure 5.8. Circumferential heat transfer comparison for 15 deg sphere-cone, $R_{\bar{z}} = 0.0279$ m.
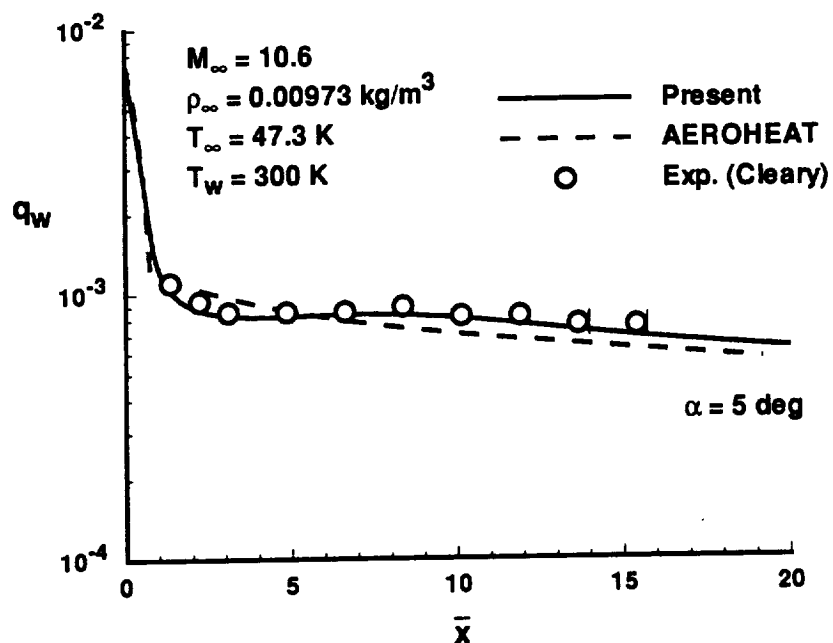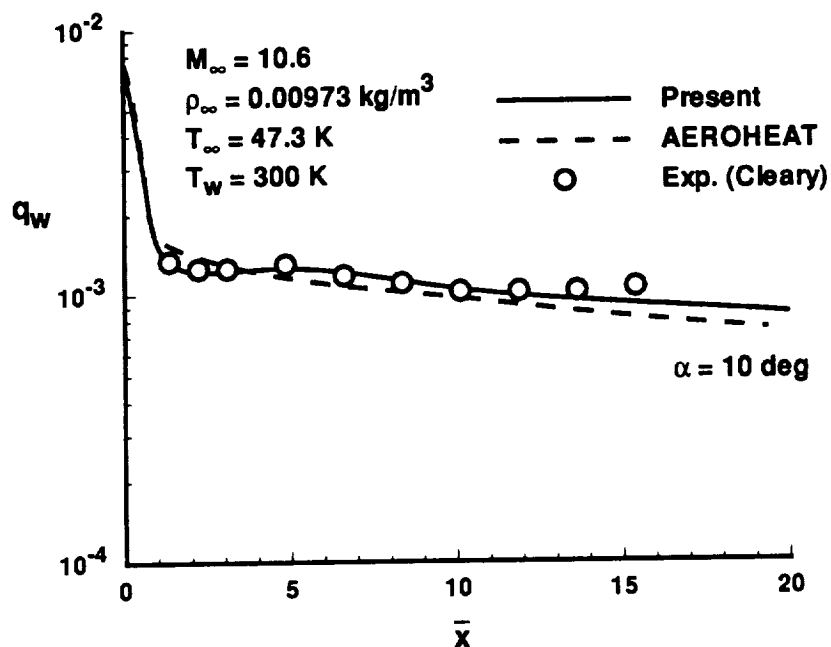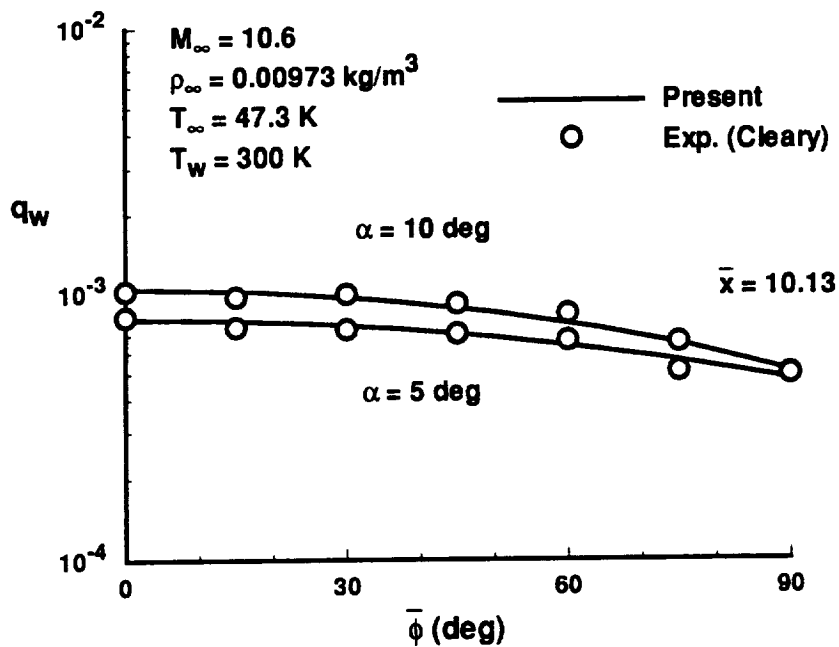

Figure 5.9. Circumferential heat transfer comparison for 15 deg sphere-cone, $R_{\bar{z}} = 0.0279$ m.
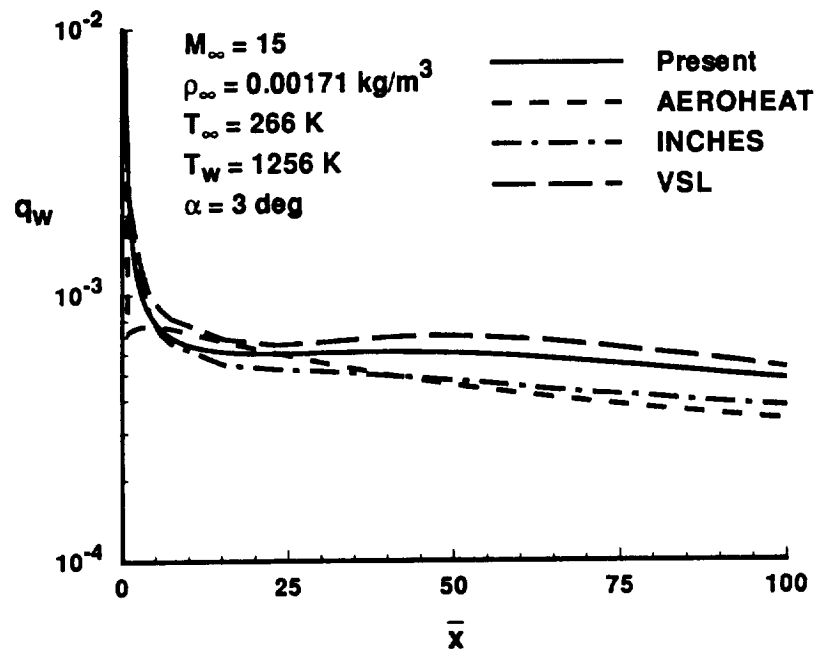
Figure 5.10. Axial heat transfer comparison for 5 deg sphere-cone, $R_{\bar{z}} = 0.0381$ m.

axial stations of 4.86 and 10.13 nose radii. This comparison illustrates the present technique's ability to compute heating rates off the windward plane of symmetry.

To demonstrate the significant improvement of the present method over current engineering aerodynamic heating methods, the surface heating rates in the windward plane of symmetry are calculated for a 5 deg spherically-blunted cone at an angle of attack of 3 deg. The freestream conditions are $M_\infty = 15$, $\rho_\infty = 0.00171$ kg/m^3, and $T_\infty = 266$ K. The wall temperature is specified to be $T_w = 1256$ K. Heating rates are computed using the present technique, AEROHEAT, INCHES [10], and a detailed VSL method [3] for a nose radius of $R_{\bar{z}} = 0.0381$ m. The resulting surface heating rates are presented in Fig. 5.10. The surface heat transfer predicted by AEROHEAT and INCHES differ by as much as 40 percent from the more accurate VSL solution.
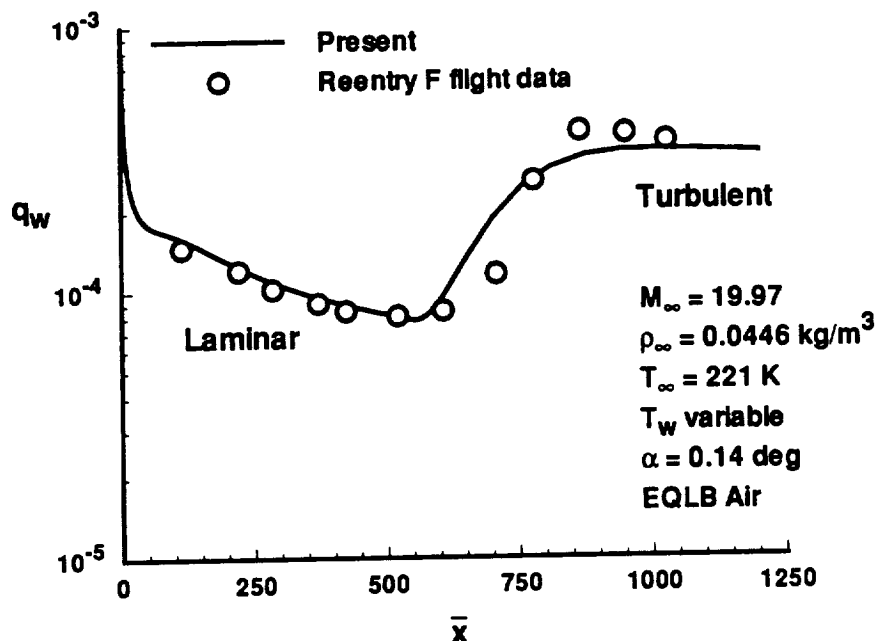
Figure 5.11. Axial heat transfer comparison with Reentry F flight data (5 deg sphere-cone at $\alpha = 0.14$ deg), $R_{\bar{z}} = 0.00356$ m.

This difference can be attributed to the approximate streamlines employed by both engineering techniques. On the other hand, the solution of the present method shows much better agreement (within 15 percent) with the VSL results and also predicts the correct trend in the surface heating rate levels.

The surface heating rates over a 5 deg spherically-blunted cone at equilibrium-air and turbulent conditions are examined next in Fig. 5.11. Results from the present method are compared with heat-transfer data obtained from the flight experiment Reentry F [47]. The Reentry F vehicle was a 5 deg spherically-blunted cone with a length of 13 ft and an initial nose radius of 0.1 inches. The data shown in Fig. 5.11 correspond to a trajectory point at 80,000 ft. The freestream conditions are $M_\infty = 19.97$,

$\rho_\infty = 0.0446 \ kg/m^3$, and $T_\infty = 221 \ K$. The wall temperature is variable and the nose radius is $R_{\bar{z}} = 0.00356 \ m$. The angle of attack is 0.14 deg. The results are for the leeward plane of the vehicle. In the present technique, equilibrium-air properties are obtained from Hansen [48], and transition is assumed to begin at the reported distance [47]. Excellent agreement between the results from the present technique and the flight laminar and turbulent data is noted.

Blunted Elliptic Cones

The perfect gas, laminar solution over a blunted 2:1 elliptic cone is examined next at angles of attack of 0 and 15 deg. Even at 0 deg angle of attack, the flowfield is three-dimensional. The cone angles in the windward and side planes are 5 and 9.93 deg, respectively. The freestream conditions are $M_\infty = 10.19$, $\rho_\infty = 0.0193$ kg/m^3, and $T_\infty = 51.1 \ K$. The wall temperature is $T_w = 261 \ K$ and the nose radius is $R_{\bar{z}} = 0.0254 \ m$. Surface heating rates from the present technique are compared with experimental data [49] and thin layer NS results from the LAURA algorithm [1]. The LAURA method is chosen for comparison purposes because of its ability to compute the flowfield about a 3-D nose. In addition, there is an apparent lack of heat-transfer data available in the open literature on 3-D nose shapes. Thirty-seven streamlines are used to obtain the solution around the elliptic cone in the present technique. A grid of 64 cells in the axial direction, 30 cells around the circumference of the body, and 64 cells in the normal direction is used to obtain the LAURA solution. The present technique requires approximately 200 CPU sec on a Sun workstation to obtain a
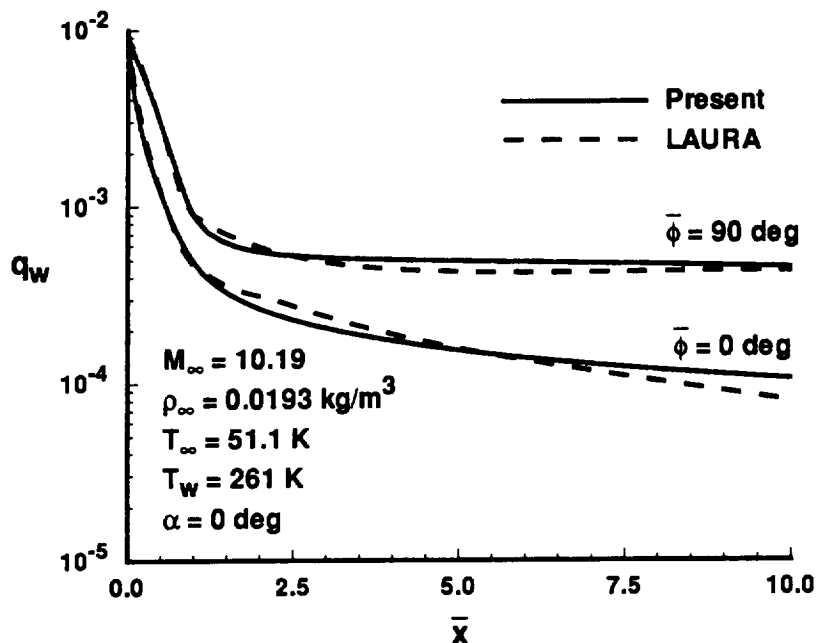
Figure 5.12. Axial heat transfer comparison for blunted 2:1 elliptic cone, $R_{\bar{z}} = 0.0254\ m$.

solution. The LAURA solution requires approximately 4 CPU hrs on a CRAY-2 supercomputer, although it should be noted that no effort was made to optimize the LAURA calculations.

Axial surface heating rates are depicted in Fig. 5.12 for the windward ($\bar{\phi} = 0$ deg) and side ($\bar{\phi} = 90$ deg) planes at an angle of attack of 0 deg. Good agreement is noted near the nose and in the side plane downstream. However, in the windward plane downstream, the results from the present technique overestimate the results generated by LAURA by 25 percent. For the blunted elliptic cone, the surface streamlines diverge rapidly from the side plane and converge towards the windward plane. Unfortunately, in this inflow region near the windward plane, it appears that the approximate
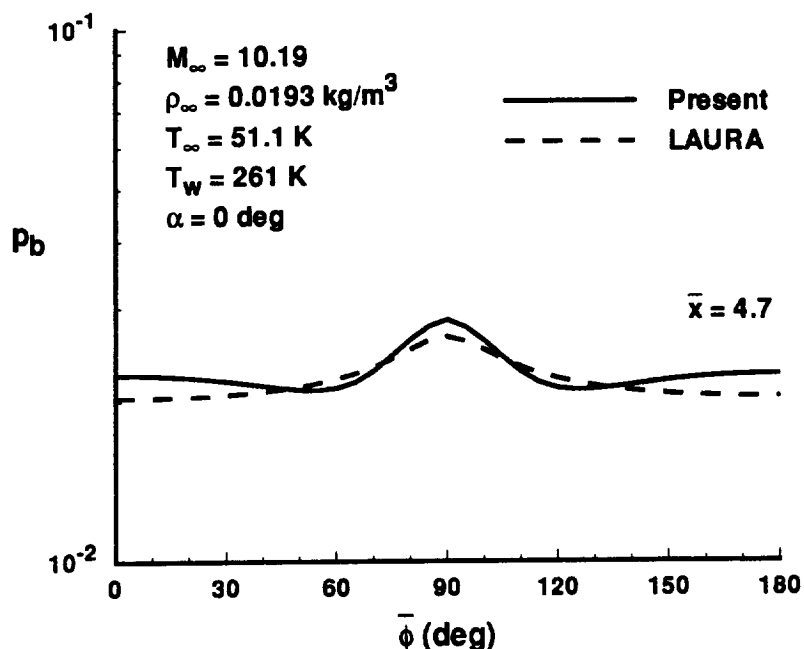
Figure 5.13. Circumferential body pressure comparison for blunted 2:1 elliptic cone.

surface pressures are not accurate enough to predict reasonable streamline paths as shown in Fig. 5.13. For this reason, the solution over the elliptic cone at 0 deg angle of attack is computed using "simplified" surface streamlines which are obtained by setting the streamline angle $\bar{\theta}$ equal to zero. At angle of attack the streamlines are again computed using the surface pressures since the inflow is reduced.

Circumferential heating rates for the blunted elliptic cone at 0 deg angle of attack are depicted in Figs. 5.14–5.17 at four axial locations on the body. The first is on the 3-D nose, whereas the remaining three are downstream on the 3-D afterbody. Excellent agreement (within 10 percent) is seen at $\bar{x} = 0.4$ on the 3-D nose. At $\bar{x} = 2.2$, the rapid drop in the heating rate away from the side plane may be attributed

Figure 5.14. Circumferential heat transfer comparison for blunted 2:1 elliptic cone, $R_{\bar{z}} = 0.0254$ m.

Figure 5.15. Circumferential heat transfer comparison for blunted 2:1 elliptic cone, $R_{\bar{z}} = 0.0254$ m.

Figure 5.16. Circumferential heat transfer comparison for blunted 2:1 elliptic cone, $R_{\bar{z}} = 0.0254$ m.

to the fact that the approximate inviscid solution is based on the shock and tends to smooth the effects of the discontinuity in body curvature at the nose-afterbody juncture. The same trend is noted in the pressure comparisons in Ref. [22]. This effect is seen in Fig. 5.12 around $\bar{x} = 1.0$. Farther downstream (at $\bar{x} = 9.7$ in Fig. 5.17) the surface heating rates from the present method match the circumferential distribution of the LAURA solution and the experimental data except near the windward and leeward planes.

The axial surface heating rates in the windward plane on the blunted 2:1 elliptic cone at 15 deg angle of attack are shown in Fig. 5.18. The agreement between the present results and the LAURA solution is excellent. As noted previously, surface

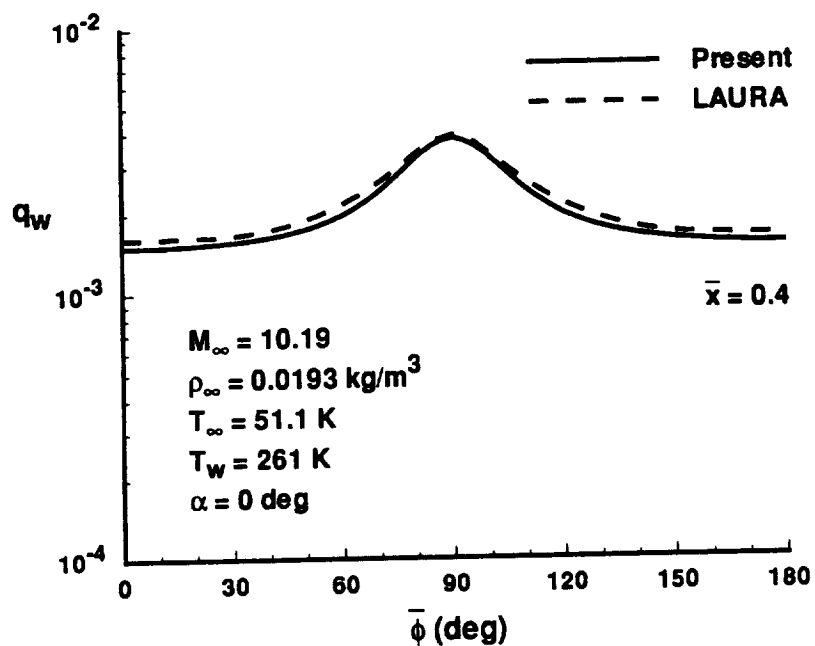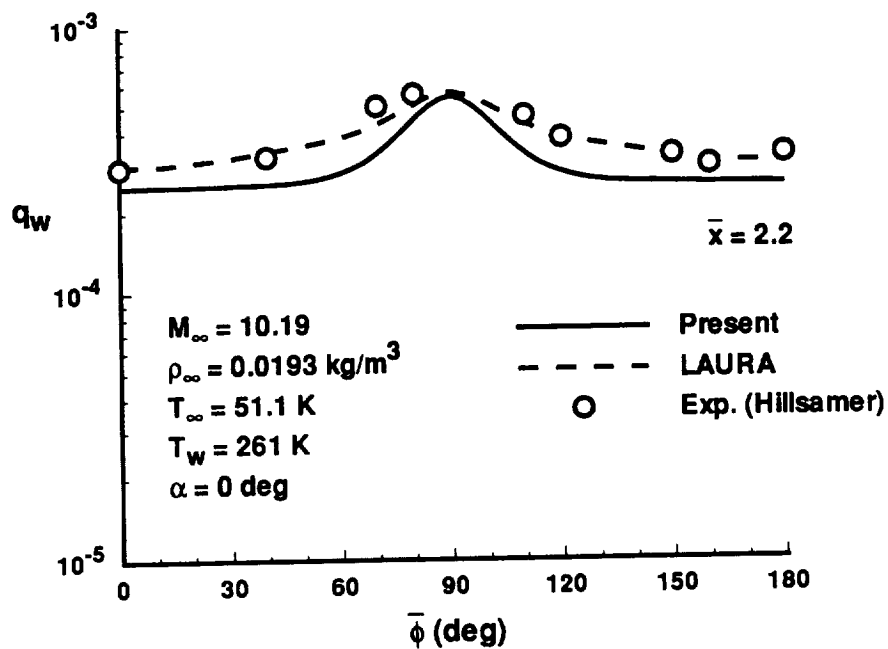**Figure 5.17.** Circumferential heat transfer comparison for blunted 2:1 elliptic cone, $R_{\bar{z}} = 0.0254$ m.

Figure 5.18. Axial heat transfer comparison for blunted 2:1 elliptic cone, $R_{\bar{z}} = 0.0254$ m.

Figure 5.19. Circumferential heat transfer comparison for blunted 2:1 elliptic cone, $R_{\bar{z}} = 0.0254$ m.

streamlines are computed from the pressure distribution at angle of attack. Circumferential surface heating rates are depicted in Figs. 5.19–5.22 at the same four axial locations as shown for 0 deg angle of attack (in Figs. 5.14–5.17). The present technique is inappropriate for calculations in the viscous-dominated leeward region on the afterbody of a vehicle at large angle of attack. For this reason, the solution is computed only in the windward region ($\bar{\phi} < 90$ deg). If a solution is desired only on the blunted nose, then the flowfield may be calculated including the leeward side. Good agreement (within 15 percent) is noted both on the 3-D nose and at the axial stations downstream. There are some discrepancies between the results from LAURA and the experimental data at $\bar{x} = 9.7$. The resolution of the LAURA grid may not
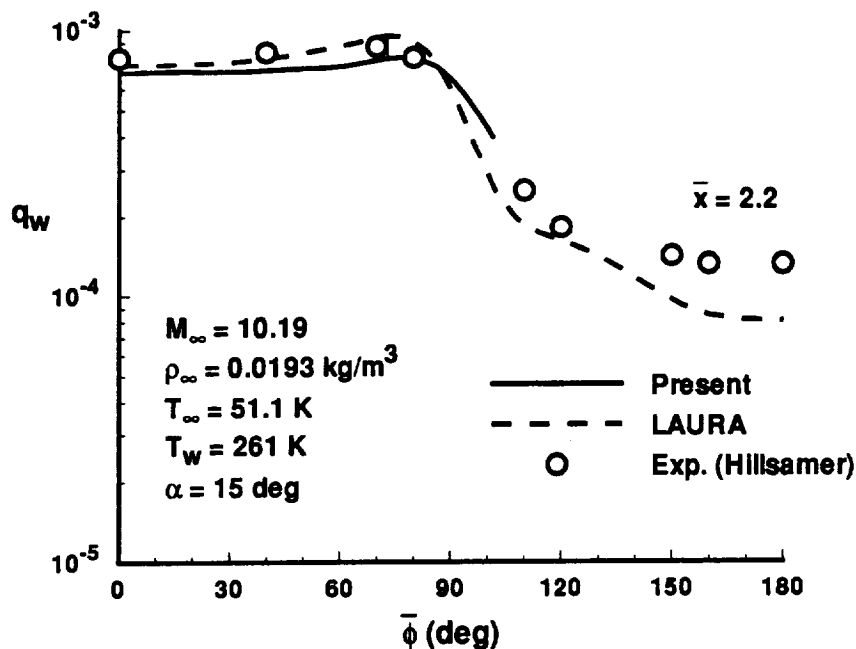
Figure 5.20. Circumferential heat transfer comparison for blunted 2:1 elliptic cone, $R_{\bar{z}} = 0.0254$ m.

be adequate for this case. These comparisons not only demonstrate an improvement over present engineering methods, but the applications to 3-D bodies significantly enhance current capabilities.

5.3 Interactive Inviscid-Boundary Layer Solutions

In this section, results are presented for a spherically-blunted and blunted elliptic cone at lower Reynolds number conditions. At these conditions, the boundary layer represents a significant portion of the shock layer so that viscous interaction could be important. The interaction between the outer inviscid layer and the viscous region is calculated using the procedure described in Chap. 4 and compared with results generated assuming no displacement effect. Note that the lower Reynolds number is
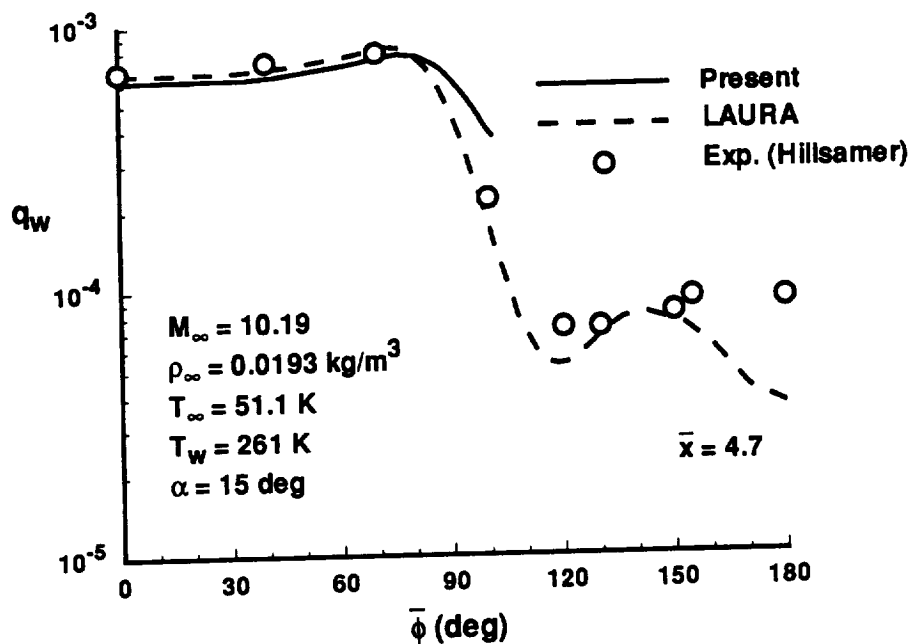
Figure 5.21. Circumferential heat transfer comparison for blunted 2:1 elliptic cone, $R_{\bar{z}} = 0.0254$ m.

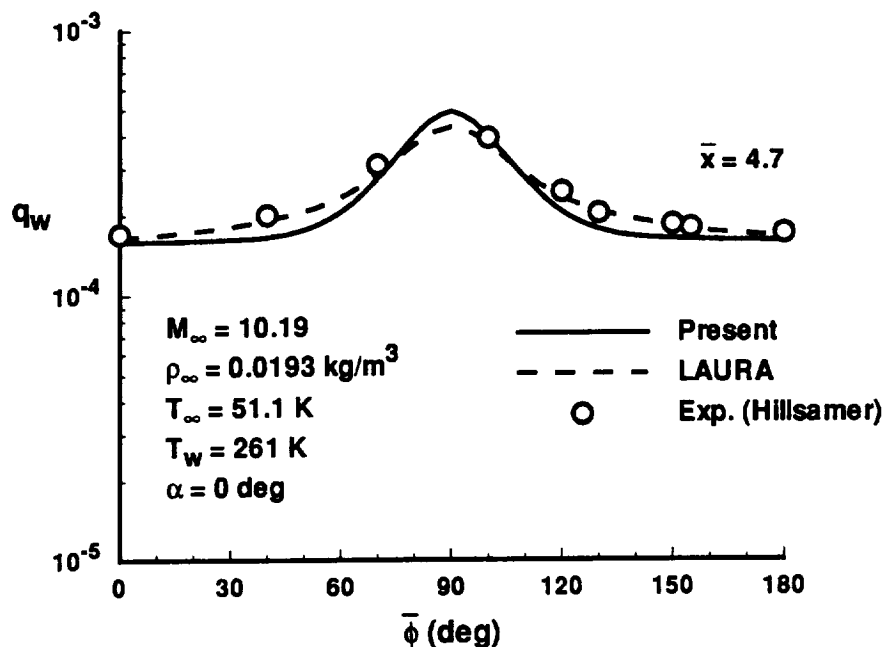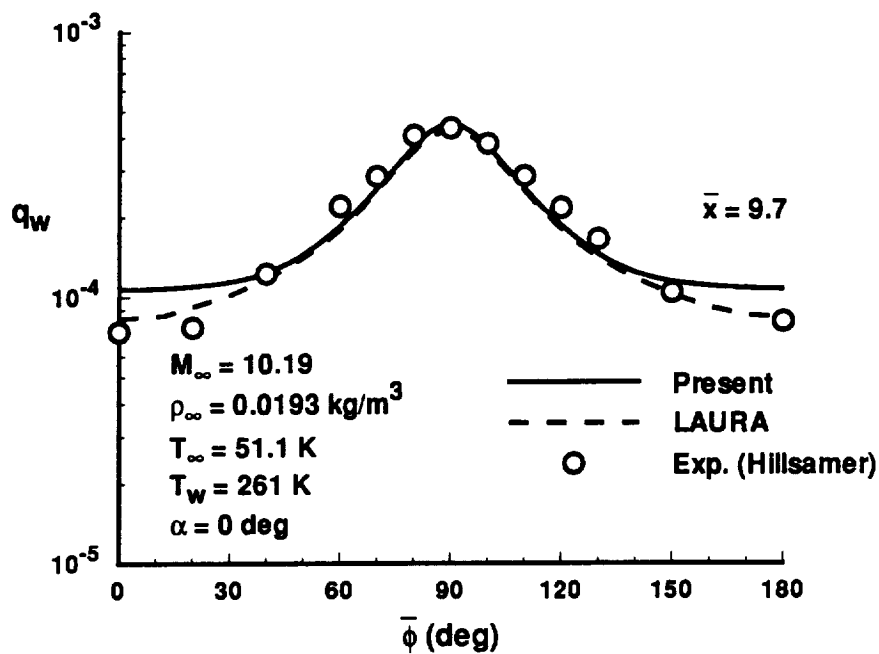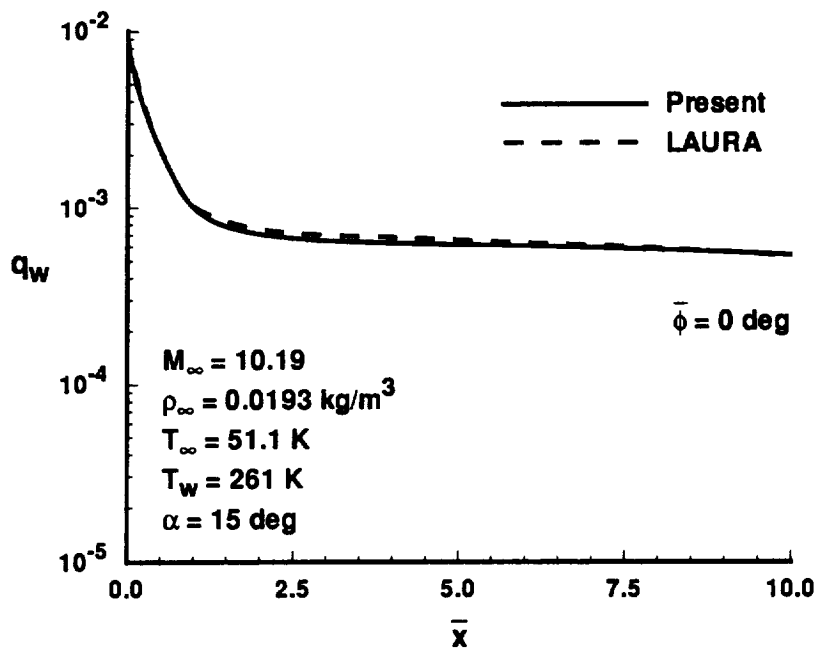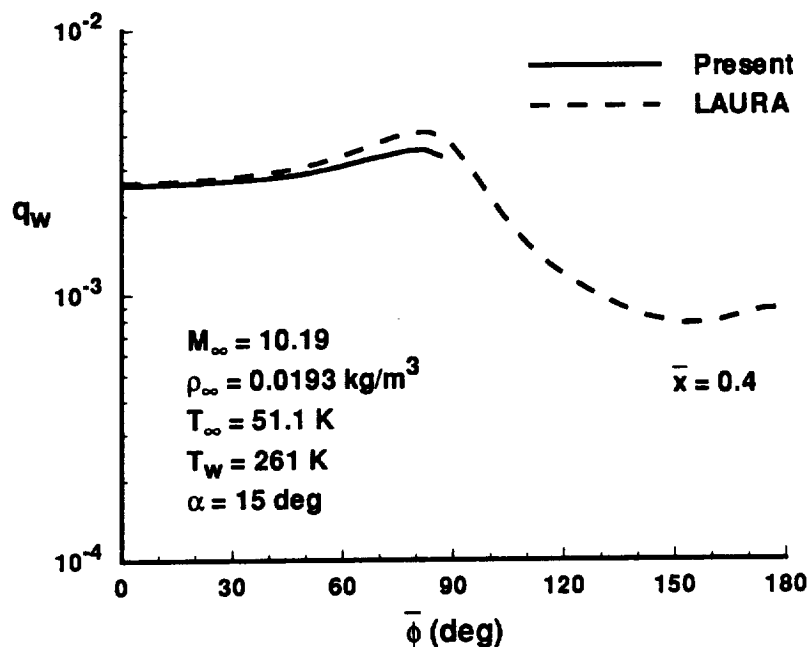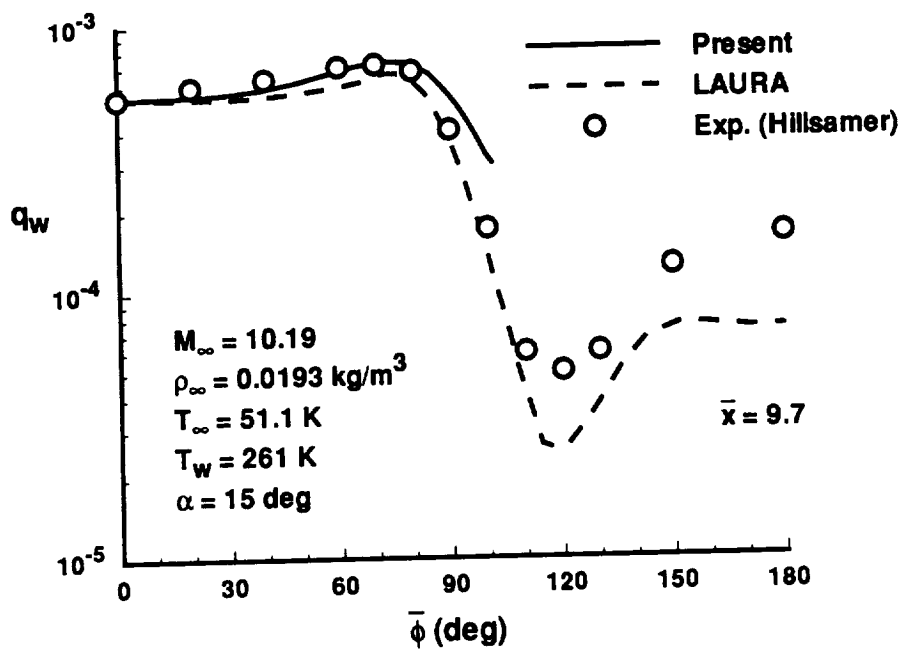**Figure 5.22.** Circumferential heat transfer comparison for blunted 2:1 elliptic cone, $R_{\bar{z}} = 0.0254$ m.
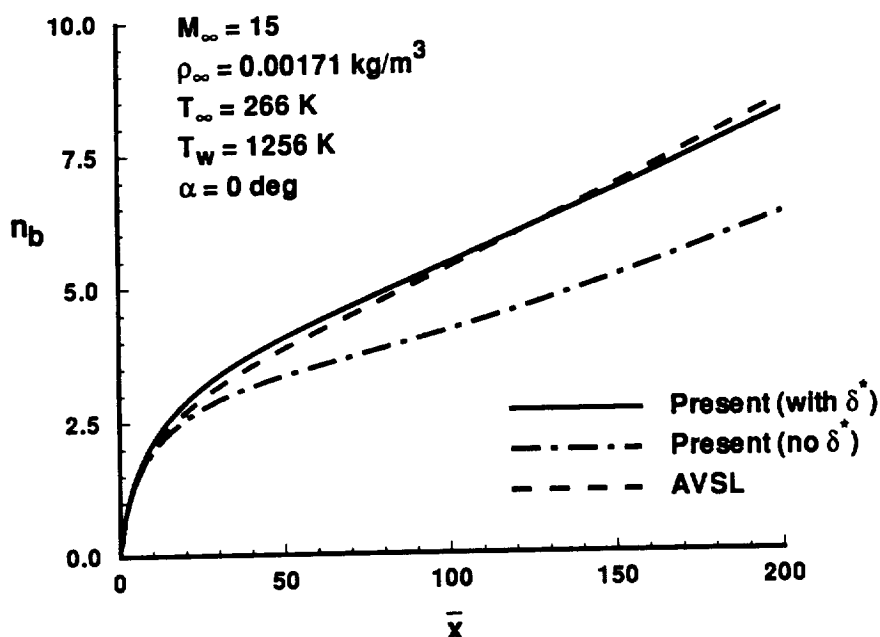
Figure 5.23. Shock layer thickness comparison for 5 deg sphere-cone, $R_{\bar{z}} = 0.00381$ m.

obtained by decreasing the nose radius only. The freestream conditions are identical to the corresponding cases in Sec. 5.2. All solutions are computed assuming perfect gas and laminar conditions.

Spherically-Blunted Cones

The shock layer and displacement thicknesses calculated for a 5 deg spherically-blunted cone are presented in Figs. 5.23 and 5.24 for 0 deg angle of attack. This cone and the corresponding freestream conditions are identical to the ones given in Fig. 5.10 except that the nose radius here is a factor of 10 smaller. It is given by $R_{\bar{z}} = 0.00381$ m. The freestream Reynolds number based on the nose radius is $Re_{\infty} = 1900$. Results from the present technique, both including and neglecting the
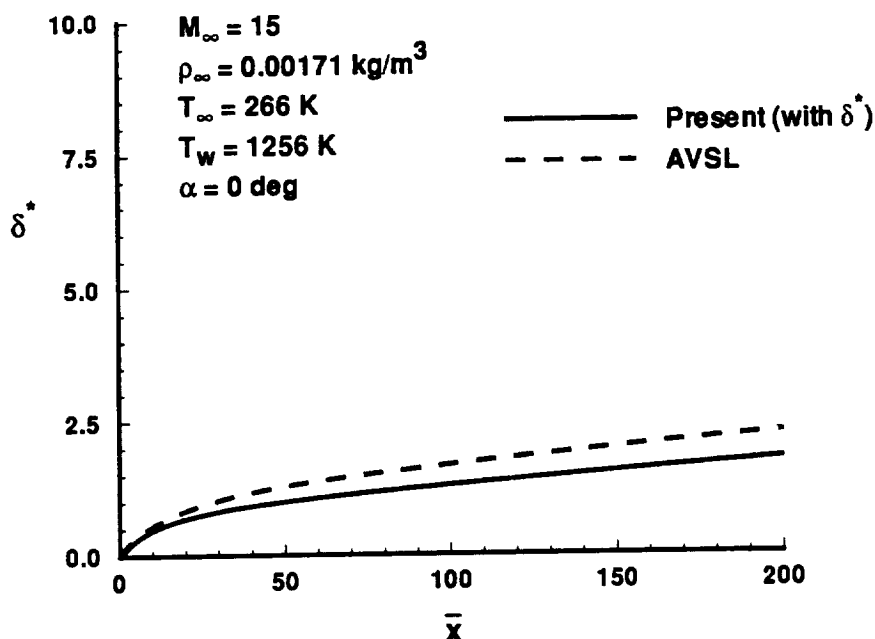
Figure 5.24. Displacement thickness comparison for 5 deg sphere-cone, $R_{\bar{z}} = 0.00381$ m.

viscous interaction, are compared with the solution generated from an approximate, axisymmetric VSL algorithm (AVSL) [43]. The AVSL technique is identical to the VSL method except that the normal momentum equation is replaced by Maslen's second-order pressure equation for axisymmetric flow.

Figures 5.23 and 5.24 illustrate the influence of the boundary layer on the inviscid flowfield. From these figures, the displacement thickness (which is less than the boundary layer thickness) is seen to make up 20 percent of the total shock layer. Therefore, neglecting the viscous interaction in the present technique leads to a much thinner shock layer than the one given by AVSL. By including the displacement effect, the present shock shape shows excellent agreement with the AVSL shock shape.
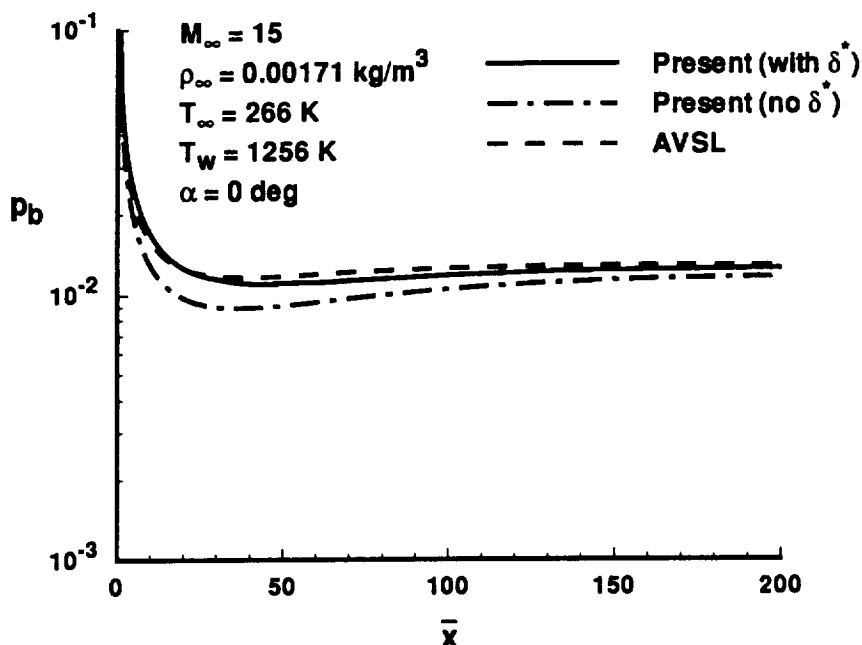
Figure 5.25. Body pressure comparison for 5 deg sphere-cone, $R_{\bar{z}} = 0.00381$ m.

In addition, note that the simple expression used for the ratio of displacement to momentum thickness, Eq. (4.2.2), agrees reasonably well (within 20 percent) with the AVSL solution in Fig. 5.24.

Figures 5.25–5.28 highlight the effect of the viscous interaction on the surface pressures and heat transfer. At the location of the pressure minimum ($\bar{x} \approx 40$) in Fig. 5.25, the present technique without the displacement effect underpredicts the surface pressure by 25 percent compared to the AVSL results. Including the displacement effect in the present method dramatically improves the comparison to within 5 percent. In addition, results generated with the viscous interaction match the correct pressure levels farther downstream at $\bar{x} = 200$. The effect on the heating rates is not as dramatic as shown in Fig. 5.26. This is expected since in the weak interaction
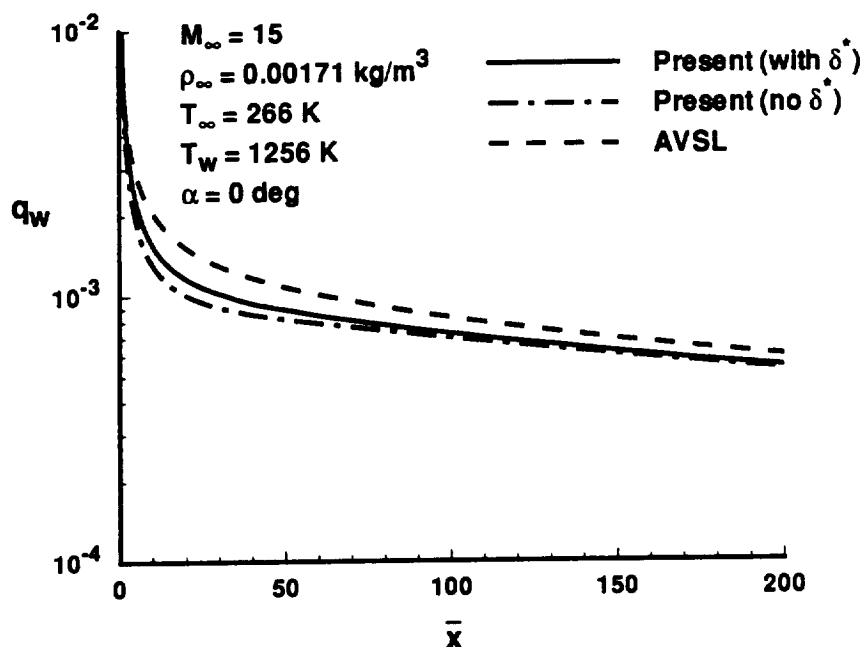
Figure 5.26. Heat transfer comparison for 5 deg sphere-cone, $R_{\bar{z}} = 0.00381$ m.

region downstream, the displacement thickness grows gradually (see Fig. 5.24) and only weakly affects the inviscid flowfield. The corresponding changes in the outer inviscid flow have a negligible effect on the boundary layer and the surface heating. Therefore, the stronger interaction effects are seen in the nose region in Figs. 5.27 and 5.28. Note that at least part of the discrepancy in the heating rates in the pressure overexpansion region is due to approximations made in the AVSL method as documented in Ref. [43].

Results generated over the 5 deg spherically-blunted cone at 0 deg angle of attack with the original nose radius of $R_{\bar{z}} = 0.0381$ m are given in Figs. 5.29-5.31. With the larger nose radius, the freestream Reynolds number is $Re_\infty = 19000$. At these conditions, the boundary layer is much thinner as shown by the shock layer thickness
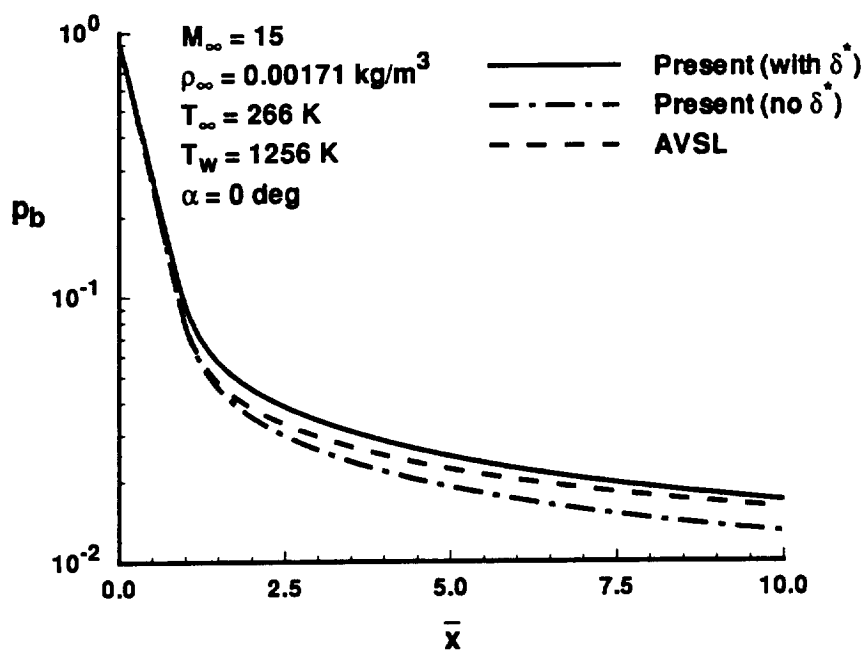
Figure 5.27. Body pressure comparison for 5 deg sphere-cone (nose region),
$R_{\bar{z}} = 0.00381$ m.
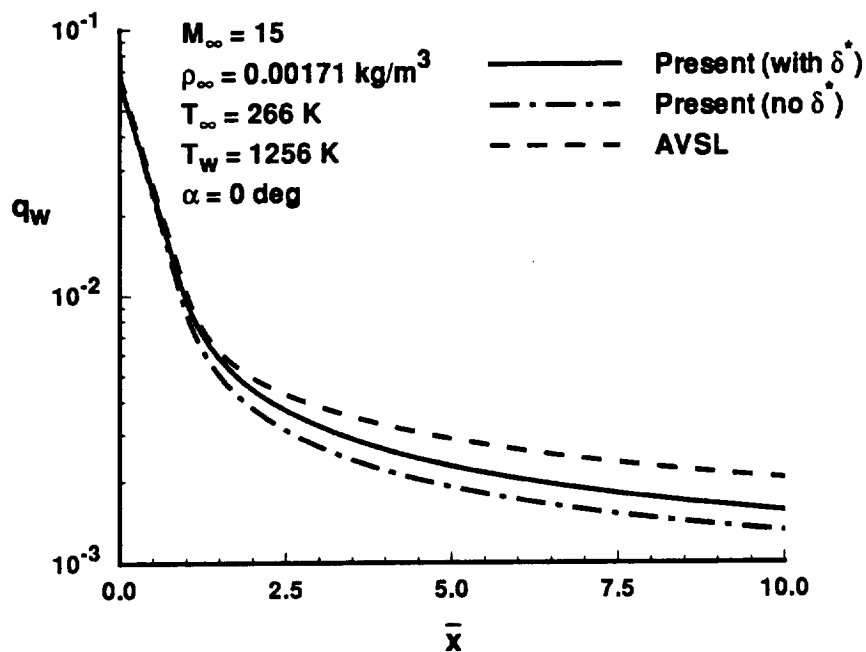
Figure 5.28. Heat transfer comparison for 5 deg sphere-cone (nose region),
$R_{\bar{z}} = 0.00381$ m.
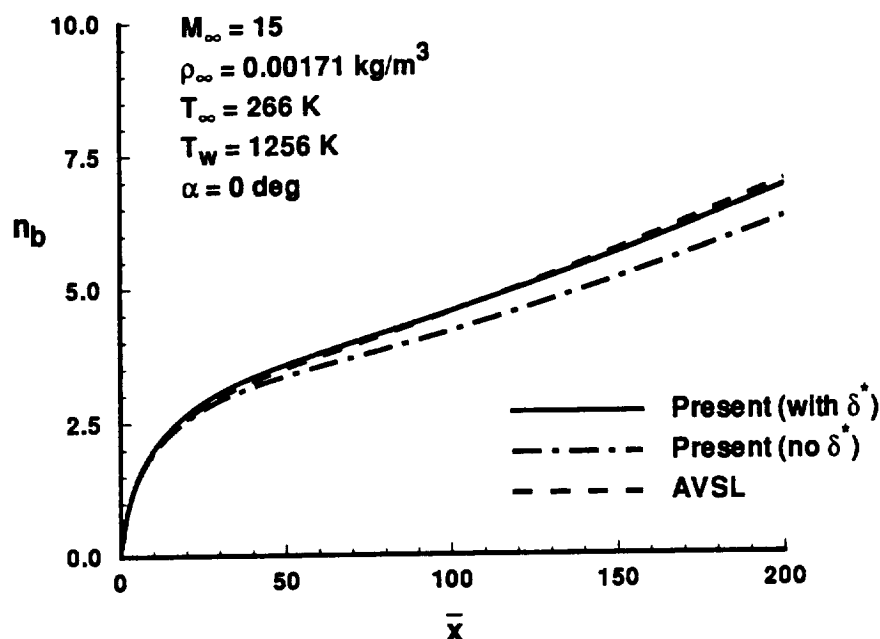
Figure 5.29. Shock layer thickness comparison for 5 deg sphere-cone, $R_{\bar{z}} = 0.0381$ m.

comparisons in Fig. 5.29. As a result, the corresponding effects on the surface pressures and heat transfer in Figs. 5.30 and 5.31 are minimal. As expected, at the larger Reynolds number corresponding to the conditions of Fig. 5.10, viscous interaction effects may be neglected.

Blunted Elliptic Cone

Solutions are examined next for the blunted 2:1 elliptic cone described in Sec. 5.2. As mentioned previously, the cone angles in the windward and side planes are 5 and 9.93 deg, respectively. The freestream conditions are identical to the ones given in Figs. 5.12–5.22. The nose radius is decreased by a factor of 100 to $R_{\bar{z}} = 0.000254$ m to illustrate the displacement effect of the boundary layer. The freestream Reynolds
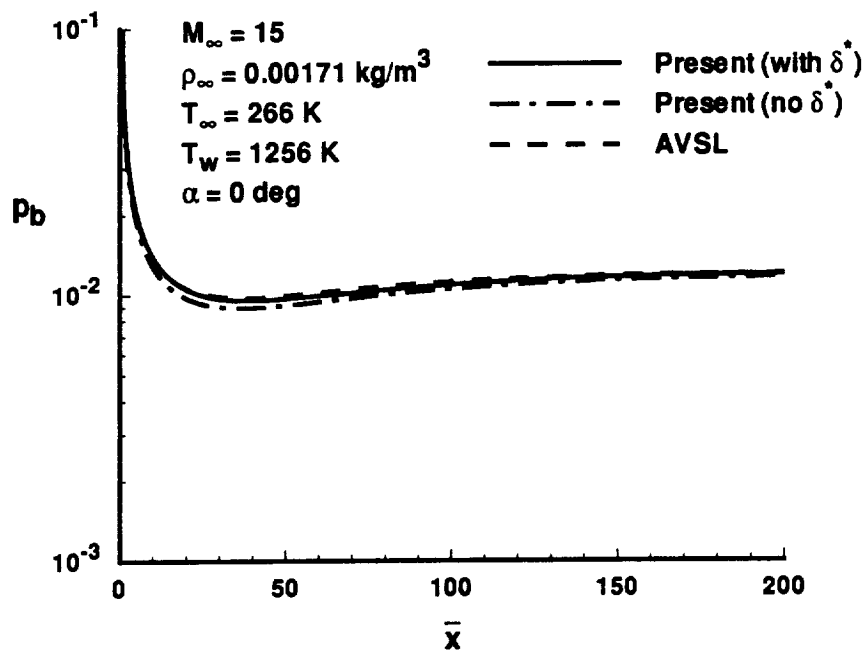
Figure 5.30. Body pressure comparison for 5 deg sphere-cone, $R_{\bar{z}} = 0.0381$ m.
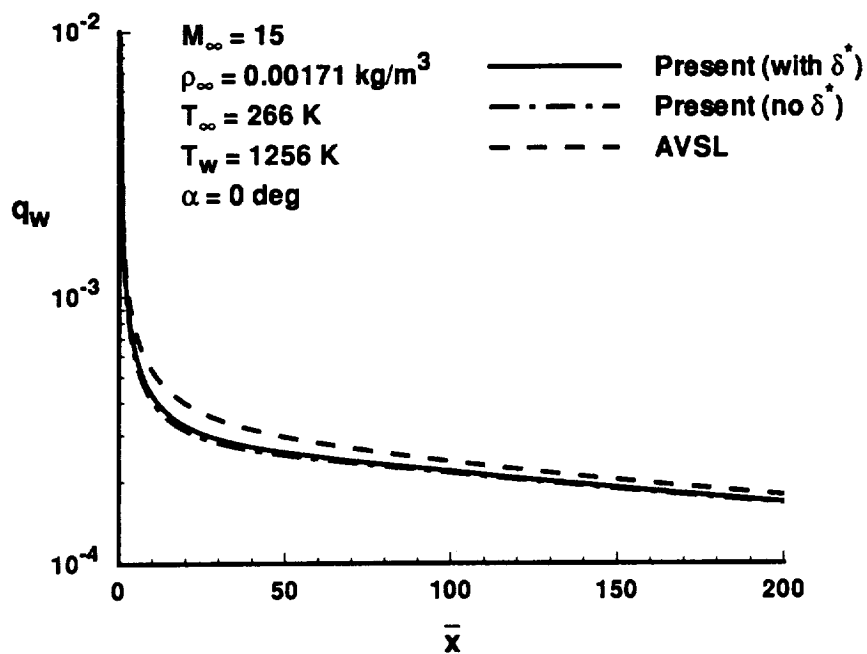
Figure 5.31. Heat transfer comparison for 5 deg sphere-cone, $R_{\bar{z}} = 0.0381$ m.
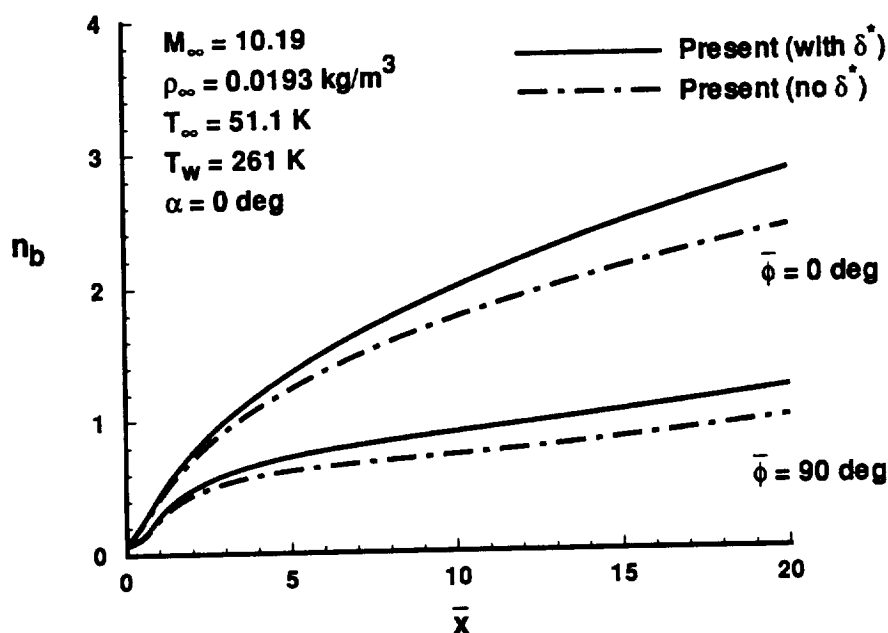
Figure 5.32. Shock layer thickness comparison for blunted 2:1 elliptic cone, $R_{\bar{z}} = 0.000254$ m.

number is $Re_\infty = 2170$. Comparisons are again made with thin layer NS results from the LAURA algorithm.

Shock layer thicknesses in the windward and side planes of symmetry are shown in Fig. 5.32. Results are calculated both including and neglecting the viscous interaction. Simplified surface streamlines ($\bar{\theta} = 0$) are again used. The region where viscous interaction effects should be greatest are encompassed in the relatively short (20 nose radii) computational domain. As seen in the comparison, the boundary layer accounts for 15-20 percent of the shock layer. The viscous interaction should significantly influence the surface properties at these conditions.

Surface pressures and heat transfer in the planes of symmetry are given in
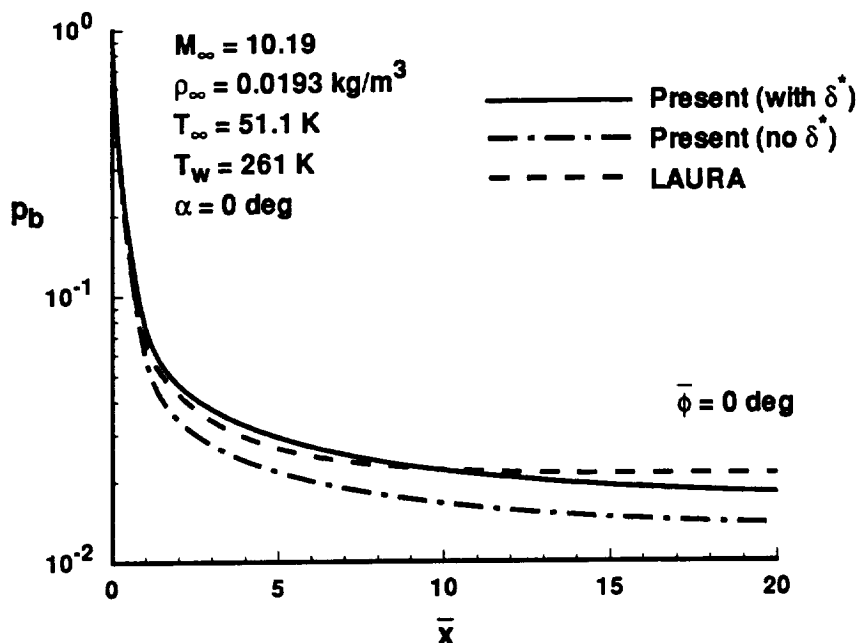
Figure 5.33. Axial body pressure comparison for blunted 2:1 elliptic cone, $R_{\bar{z}} = 0.000254$ m.

Figs. 5.33–5.36. In Figs. 5.33 and 5.34, comparisons of the surface pressures and heating rates improve when viscous interaction effects are included. Without the displacement effect, the present technique underpredicts both the pressure levels and the heating rates by at least 30 percent. By including the displacement effect, the comparison with the LAURA solution is within 15 percent. Similar improvement is seen in the side plane as shown in Figs. 5.35 and 5.36.

Circumferential pressure and heat transfer distributions are given in Figs. 5.37–5.42 at three axial locations. The first is again on the 3-D nose, whereas the other two are located downstream on the 3-D afterbody. As shown in the axial distributions, the results generated with the viscous interaction effects agree more closely
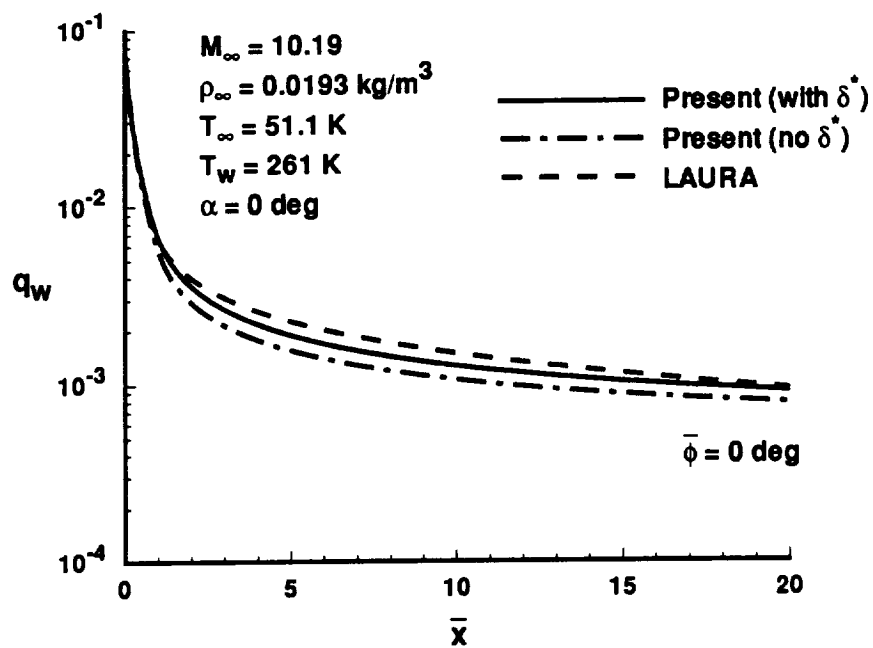
Figure 5.34. Axial heat transfer comparison for blunted 2:1 elliptic cone, $R_{\bar{z}} = 0.000254$ m.
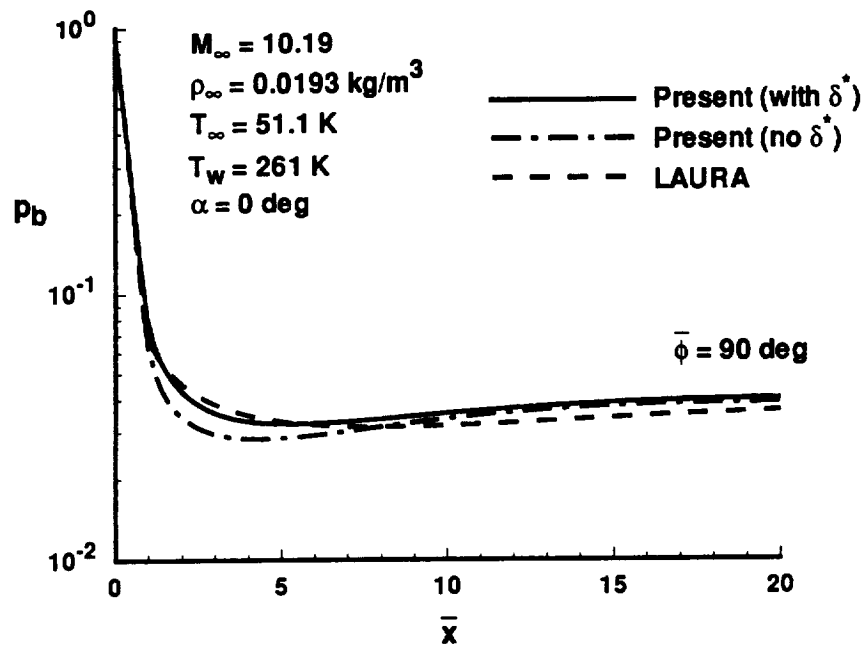
Figure 5.35. Axial body pressure comparison for blunted 2:1 elliptic cone, $R_{\bar{z}} = 0.000254$ m.
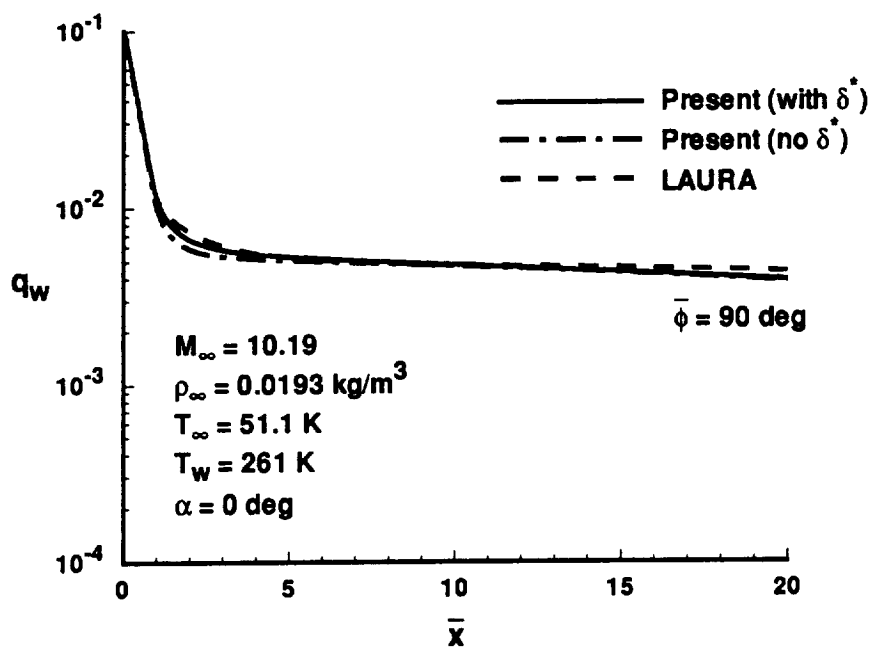
Figure 5.36. Axial heat transfer comparison for blunted 2:1 elliptic cone, $R_{\bar{z}} = 0.000254$ m.
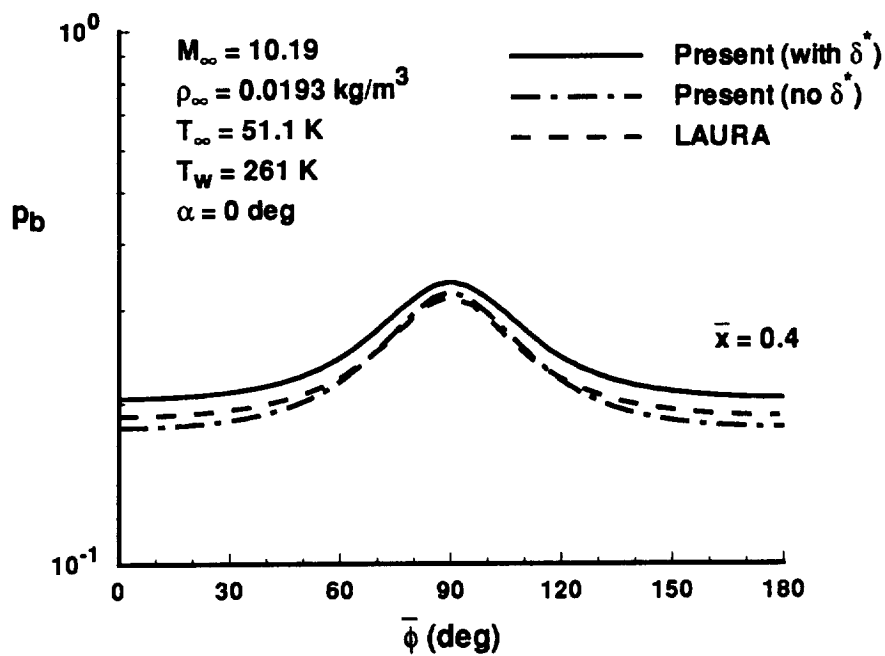
Figure 5.37. Circumferential body pressure comparison for blunted 2:1 elliptic cone, $R_{\bar{z}} = 0.000254$ m.
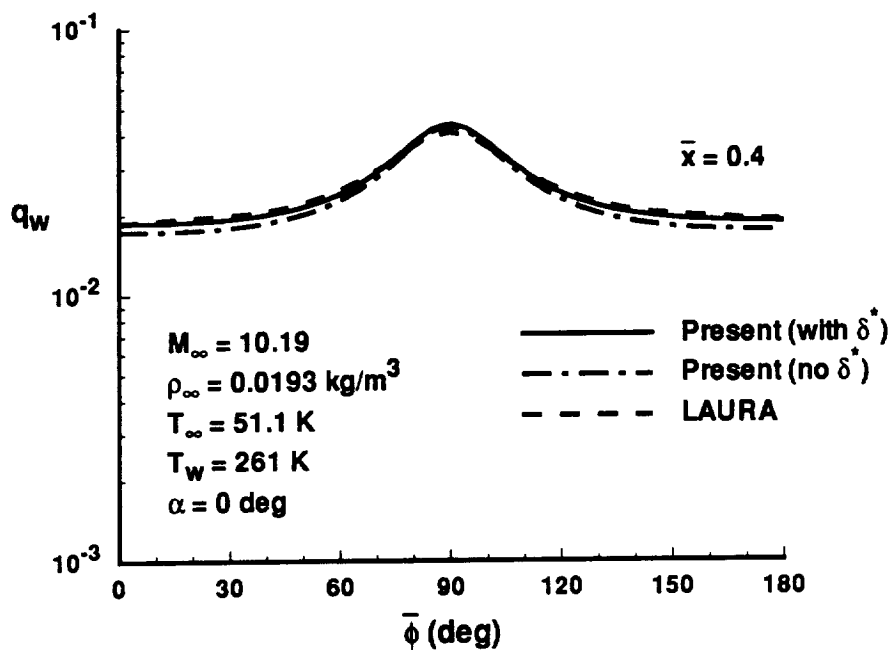
Figure 5.38. Circumferential heat transfer comparison for blunted 2:1 elliptic cone, $R_{\bar{z}} = 0.000254$ m.

with the LAURA solution. The improvement is most dramatic near the windward plane. These comparisons on the 3-D body shape as well as the axisymmetric cone demonstrate that the applicability of engineering methods can be extended to lower Reynolds number flows by including viscous interaction effects. However, keep in mind that at even lower Reynolds numbers, the boundary layer may merge with the shock layer. The shock layer is fully viscous and an inviscid-boundary layer approach is not valid.
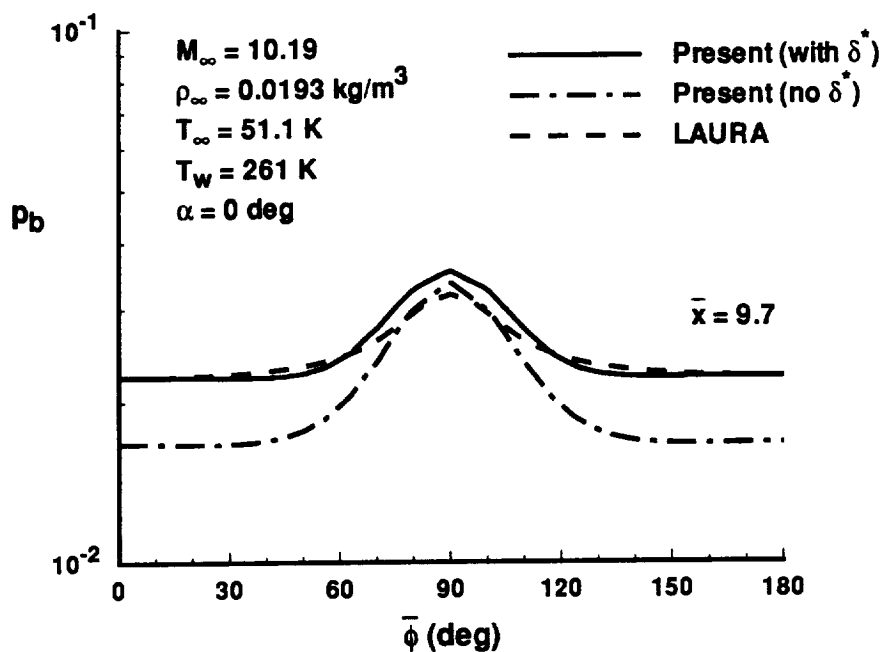
Figure 5.39. Circumferential body pressure comparison for blunted 2:1 elliptic cone, $R_{\bar{z}} = 0.000254$ m.
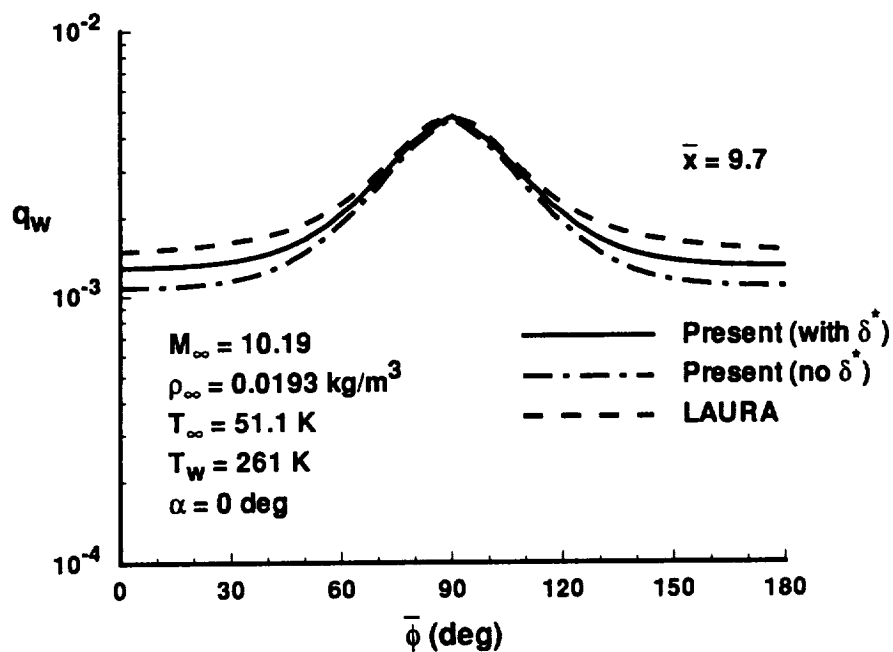
Figure 5.40. Circumferential heat transfer comparison for blunted 2:1 elliptic cone, $R_{\bar{z}} = 0.000254$ m.
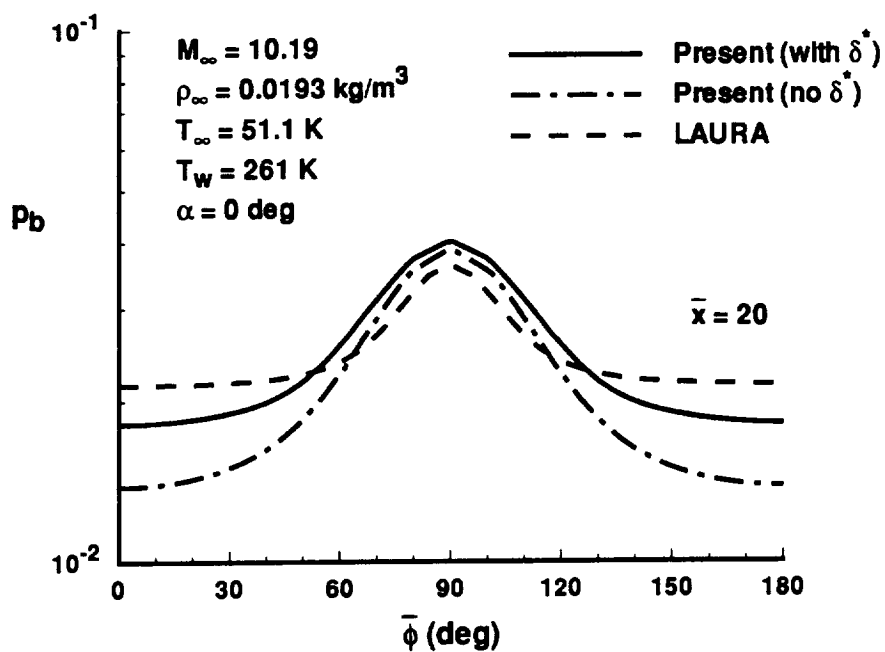
Figure 5.41. Circumferential body pressure comparison for blunted 2:1 elliptic cone, $R_{\bar{z}} = 0.000254$ m.
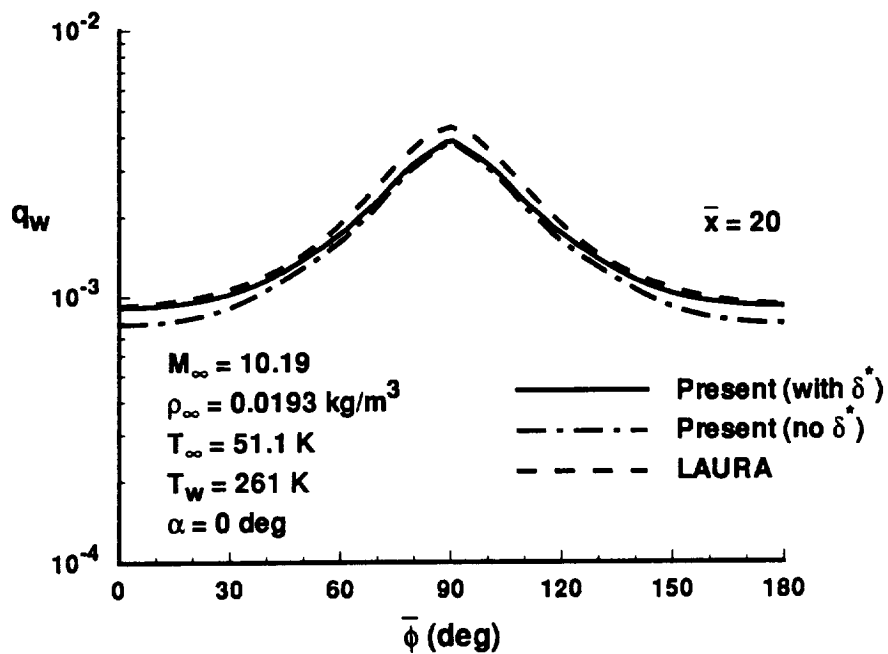
Figure 5.42. Circumferential heat transfer comparison for blunted 2:1 elliptic cone, $R_{\bar{z}} = 0.000254$ m.

6   Conclusions

A new engineering method has been developed that calculates the coupled inviscid-boundary layer flow over blunted bodies in 3-D hypersonic flow. The effect of the boundary layer on the outer inviscid flow is included to improve the applicability of the technique. The method is applied to the solution over spherically-blunted cones and 3-D elliptic cones at angle of attack for the laminar and turbulent flow of a perfect gas and equilibrium air.

The inviscid properties (surface pressures and shock shapes) given by the present technique compare favorably with experimental data and numerical solutions of the Euler equations except in the leeward region at angle of attack. For high Reynolds number flows, the present technique predicts surface heating rates that show good agreement with experimental data, equilibrium-air flight data, and numerical solutions of the NS and VSL equations. One of the limitations of the method is its inability to calculate surface streamlines from the pressure distribution for elliptic bodies at 0 deg angle of attack. Simplified streamlines based solely on the body geometry may be used in these instances. For lower Reynolds numbers, the inclusion of the viscous interaction greatly improves the shock shape and surface properties generated by the present technique. As anticipated, the viscous interaction has the least influence on surface heat transfer.

The present engineering method significantly extends the capabilities of current

engineering techniques in the following areas: 3-D applications, accuracy of inviscid solution, and ability to account for the viscous interaction. Solutions generated by the present technique can also be obtained with very little computational effort. Therefore, for these reasons, it would make an excellent tool for preliminary aerothermal design.

References

[1] P. A. Gnoffo. "An Upwind-Biased, Point-Implicit Relaxation Algorithm for Viscous, Compressible Perfect-Gas Flows". NASA TP-2953, Feb. 1990.

[2] S. L. Lawrence, D. S. Chaussee, and J. C. Tannehill. "Application of an Upwind Algorithm to the Three-Dimensional Parabolized Navier-Stokes Equations". AIAA 87-1112, June 1987.

[3] A. L. Murray and C. H. Lewis. "Hypersonic Three-Dimensional Viscous Shock-Layer Flows Over Blunt Bodies". *AIAA Journal*, Vol. 16: pp. 1279-1286, Dec. 1978.

[4] S. Swaminathann, M. D. Kim, and C. H. Lewis. "Three-Dimensional Nonequilibrium Viscous Shock-Layer Flows Over Complex Geometries". AIAA 83-0212, Jan. 1983.

[5] R. A. Thompson. "Comparison of Nonequilibrium Viscous-Shock-Layer Solutions with Shuttle Heating Measurements". *Journal of Thermophysics and Heat Transfer*, Vol. 4: pp. 162-169, April-June 1990.

[6] D. W. Hall, R. W. Hines, F. P. Baltakis, and A. B. Wardlaw. "Coupled Inviscid/Viscous Aerodynamic Predictions for Supersonic Tactical Missiles". AIAA 90-0617, Jan. 1990.

[7] F. Monnoyer, Ch. Mundt, and M. Pfitzner. "Calculation of the Hypersonic Viscous Flow Past Reentry Vehicles with an Euler-Boundary Layer Coupling Method". AIAA 90-0417, Jan. 1990.

[8] F. R. DeJarnette and H. H. Hamilton. "Inviscid Surface Streamlines and Heat Transfer on Shuttle-Type Configurations". *Journal of Spacecraft and Rockets*, Vol. 10: pp. 314-321, May 1973.

[9] F. R. DeJarnette and H. H. Hamilton. "Aerodynamic Heating on 3-D Bodies Including the Effects of Entropy-Layer Swallowing". *Journal of Spacecraft and Rockets*, Vol. 12: pp. 5-12, Jan. 1975.

[10] E. V. Zoby and A. L. Simmonds. "Engineering Flowfield Method With Angle-of-Attack Applications". *Journal of Spacecraft and Rockets*, Vol. 22: pp. 398-405, July-Aug. 1985.

[11] H. H. Hamilton, F. R. DeJarnette, and K. J. Weilmuenster. "Application of Axisymmetric Analog for Calculating Heating in Three-Dimensional Flows". *Journal of Spacecraft and Rockets*, Vol. 24: pp. 296-302, July-Aug. 1987.

[12] J. D. Anderson, Jr. *Hypersonic and High Temperature Gas Dynamics*. McGraw-Hill, Inc., 1989.

[13] J. C. Cooke. "An Axially Symmetric Analogue for General Three-Dimensional Boundary Layers". Aeronautical Research Council TR R&M 3200, British Ministry of Aviation, June 1961.

[14] S. H. Maslen. "Inviscid Hypersonic Flow Past Smooth Symmetric Bodies". *AIAA Journal*, Vol. 2: pp. 1055–1061, June 1964.

[15] E. V. Zoby and R. A. Graves, Jr. "A Computer Program for Calculating the Perfect Gas Inviscid Flow Field About Blunt Axisymmetric Bodies at an Angle of Attack of 0 deg". NASA TM X-2843, Dec. 1973.

[16] R. A. Thompson, E. V. Zoby, K. E. Wurster, and P. A. Gnoffo. "An Aerothermodynamic Study of Slender Conical Vehicles". *Journal of Thermophysics and Heat Transfer*, Vol. 4: pp. 361–367, Oct.-Dec. 1990.

[17] C. J. Riley, F. R. DeJarnette, and E. V. Zoby. "Surface Pressure and Streamline Effects on Laminar Heating Calculations". *Journal of Spacecraft and Rockets*, Vol. 27: pp. 9–14, Jan.-Feb. 1990.

[18] K. E. Wurster, E. V. Zoby, and R. A. Thompson. "Flowfield and Vehicle Parameter Influence on Results of Engineering Aerothermal Methods". *Journal of Spacecraft and Rockets*, Vol. 28: pp. 16–22, Jan.-Feb. 1991.

[19] S. K. Jackson, Jr. *The Viscous-Inviscid Hypersonic Flow of a Perfect Gas Over Smooth Symmetric Bodies*. PhD thesis, University of Colorado, 1966.

[20] C. J. Riley. "An Approximate Method for Calculating Inviscid Flow Fields Over Three-Dimensional Bodies in Hypersonic Flow". Master's thesis, North Carolina State University, May 1988.

[21] C. J. Riley and F. R. DeJarnette. "An Approximate Method for Calculating Three-Dimensional Inviscid Hypersonic Flow Fields". NASA TP-3018, Aug. 1990.

[22] C. J. Riley and F. R. DeJarnette. "Engineering Calculations of Three-Dimensional Inviscid Hypersonic Flow Fields". *Journal of Spacecraft and Rockets*, Vol. 28: pp. 628–635, Nov.-Dec. 1991.

[23] S. H. Maslen. "Asymmetric Hypersonic Flow". NASA CR-2123, Sept. 1972.

[24] E. V. Zoby, J. N. Moss, and K. Sutton. "Approximate Convective-Heating Equations for Hypersonic Flows". *Journal of Spacecraft and Rockets*, Vol. 18: pp. 64–70, Jan.-Feb. 1981.

[25] M. D. Van Dyke and H. D. Gordon. "Supersonic Flow Past a Family of Blunt Axisymmetric Bodies". NASA TR R-1, 1959.

[26] F. M. Cheatwood and F. R. DeJarnette. "An Interactive User-Friendly Approach to Surface-Fitting Three-Dimensional Geometries". NASA CR-4126, March 1988.

[27] C. J. Riley and F. R. DeJarnette. "An Engineering Aerodynamic Heating Method for Hypersonic Flow". AIAA 92-0499, Jan. 1992.

[28] F. M. White. *Viscous Fluid Flow*. McGraw-Hill, Inc., 1974.

[29] W. D. Hayes. "The Three-Dimensional Boundary Layer". NAVORD Rept. 1313, U.S. Naval Ordnance Test Station, Inyoken, China Lake, CA, May 1951.

[30] R. Vaglio-Laurin. "Laminar Heat Transfer on Three-Dimensional Blunt Nosed Bodies in Hypersonic Flow". *ARS Journal*, Vol. 29: pp. 123–129, Feb. 1959.

[31] E. V. Zoby. "Approximate Heating Analysis for the Windward Symmetry Plane of Shuttle-Like Bodies at Large Angle of Attack". *Progress in Astronautics and Aeronautics*, Vol. 82: pp. 229–247, 1982.

[32] E. V. Zoby. "Analysis of STS-1 Experimental Heating Rates and Transition Data". *Journal of Spacecraft and Rockets*, Vol. 20: pp. 214–218, May-June 1983.

[33] E. V. Zoby. "Analysis of STS-2 Experimental Heating Rates and Transition Data". *Journal of Spacecraft and Rockets*, Vol. 20: pp. 232–237, May-June 1983.

[34] E. R. G. Eckert. "Survey on Heat Transfer at High Speeds". ARL 189, U.S. Air Force, Dec. 1961.

[35] C. B. Johnson and D. M. Bushnell. "Power-Law Velocity-Profile-Exponent Variations With Reynolds Number, Wall Cooling, and Mach Number in a Turbulent Boundary Layer". NASA TN D-5753, April 1970.

[36] S. Dhawan and R. Narasimha. "Some Properties of Boundary Layer Flow During Transition from Laminar to Turbulent Motion". *Journal of Fluid Mechanics*, Vol. 3: pp. 418–436, April 1958.

[37] C. B. Cohen and E. Reshotko. "The Compressible Laminar Boundary Layer With Heat Transfer and Arbitrary Pressure Gradient". NACA Report 1294, 1956.

[38] G. K. Walker and B. A. Schumann. "The Growth of Turbulent Boundary Layers". TIS No. R61SD123, General Electric Co., July 1961.

[39] W. D. Goodrich, C. P. Li, C. K. Houston, P. B. Chiu, and L. Olmedo. "Numerical Computations of Orbiter Flow Fields and Laminar Heating Rates". *Journal of Spacecraft and Rockets*, Vol. 14: pp. 257–264, May 1977.

[40] J. V. Rakich and M. J. Lanfranco. "Numerical Computation of Space Shuttle Laminar Heating and Surface Streamlines". *Journal of Spacecraft and Rockets*, Vol. 14: pp. 265–272, May 1977.

[41] K. J. Weilmuenster and H. H. Hamilton. "Calculations of Inviscid Flow Over Shuttle-Like Vehicles at High Angles of Attack and Comparisons With Experimental Data". NASA TP-2103, May 1983.

[42] F. Marconi, M. Salas, and L. Yaeger. "Development of a Computer Code for Calculating the Steady Super/Hypersonic Inviscid Flow Around Real Configurations. Volume I - Computational Technique". NASA CR-2675, April 1976.

[43] F. M. Cheatwood and F. R. DeJarnette. "An Approximate Viscous Shock Layer Approach to Calculating Hypersonic Flows About Blunt-Nosed Bodies". AIAA 91-1348, June 1991.

[44] C. G. Miller III. "Measured Pressure Distributions, Aerodynamic Coefficients, and Shock Shapes on Blunt Bodies at Incidence in Hypersonic Air and CF4". NASA TM-84489, Sept. 1982.

[45] R. L. Palko and A. D. Ray. "Pressure Distribution and Flow Visualization Tests of a 1.5 Elliptic Cone at Mach 10". AEDC-TDR 63-163, U.S. Air Force, Aug. 1963.

[46] J. W. Cleary. "Effects of Angle of Attack and Bluntness on Laminar Heating-Rate Distributions of a 15° Cone at a Mach Number of 10.6". NASA TN D-5450, Oct. 1969.

[47] P. C. Stainback, C. B. Johnson, L. B. Boney, and K. C. Wicker. "Comparison of Theoretical Predictions and Heat-Transfer Measurements for a Flight Experiment at Mach 20 (Reentry F)". NASA TM X-2560, 1972.

[48] C. F. Hansen. "Approximations for the Thermodynamic and Transport Properties of High-Temperature Air". NASA TR R-50, 1959.

[49] M. E. Hillsamer and J. P. Rhudy. "Heat-Transfer and Shadowgraph Tests of Several Elliptical Lifting Bodies at Mach 10". AEDC-TDR 64-19, U.S. Air Force, Feb. 1964.

[50] P. A. Libby and R. J. Cresci. "Evaluation of Several Hypersonic Turbulent Heat Transfer Analyses by Comparison With Experimental Data". WADC TN 57-72, July 1957.

[51] R. J. Cresci, D. A. MacKenzie, and P. A. Libby. "An Investigation of Laminar, Transitional, and Turbulent Heat Transfer on Blunt-Nosed Bodies in Hypersonic Flow". *Journal of Aerospace Sciences*, Vol. 27: pp. 401–414, June 1960.

[52] L. Lees. "Laminar Heat Transfer Over Blunt Bodies at Hypersonic Flight Speeds". *Jet Propulsion*, Vol. 26: pp. 259–269,274, April 1956.

A   Nondimensional Variables

Variables are nondimensionalized according to the following relations:

$$L = \frac{L'}{L'_{ref}} \qquad \kappa = \kappa' L'_{ref} \qquad \Psi = \frac{\Psi'}{\rho'_\infty V'_\infty L'^2_{ref}}$$

$$V = \frac{V'}{V'_\infty} \qquad \rho = \frac{\rho'}{\rho'_\infty} \qquad p = \frac{p'}{\rho'_\infty V'^2_\infty}$$

$$h = \frac{h'}{V'^2_\infty} \qquad T = \frac{T'}{T'_\infty} \qquad \mathcal{R} = \frac{\mathcal{R}' T'_\infty}{V'^2_\infty}$$

$$\mu = \frac{\mu'}{\rho'_\infty V'_\infty L'_{ref}} \qquad q = \frac{q'}{\rho'_\infty V'^3_\infty} \qquad k = \frac{k' T'_\infty}{\rho'_\infty V'^3_\infty L'_{ref}}$$

Units for the dimensional quantities are

$$L' = [m] \qquad \kappa' = \left[\frac{1}{m}\right] \qquad \Psi' = \left[\frac{kg}{s}\right]$$

$$V' = \left[\frac{m}{s}\right] \qquad \rho' = \left[\frac{kg}{m^3}\right] \qquad p' = \left[\frac{N}{m^2}\right]$$

$$h' = \left[\frac{J}{kg}\right] \qquad T' = [K] \qquad \mathcal{R}' = \left[\frac{J}{kg\ K}\right]$$

$$\mu' = \left[\frac{kg}{m\ s}\right] \qquad q' = \left[\frac{W}{m^2}\right] \qquad k' = \left[\frac{W}{m\ K}\right]$$

C-2

B Coordinate Transformation

Before using the curvilinear coordinates (ξ, β, n), it is advantageous to relate them to more accessible coordinates. On the shock surface where the curvilinear coordinates are orthogonal, transformation operators are derived that relate partial derivatives in the curvilinear system to derivatives in the cylindrical and Cartesian systems. Derivatives of the scale factors at the shock are also given. Within the shock layer where the curvilinear coordinates are nonorthogonal, both the coordinate transformation between the curvilinear and Cartesian systems and their partial derivatives are derived. On the body surface, the transformation between the shock curvilinear coordinates and a set of body orthogonal curvilinear coordinates $(\bar{\xi}, \bar{\beta}, \bar{n})$ is given. This transformation assists in the coupling of the viscous solution with the inviscid solution.

B.1 Shock Surface

To derive the transformation operators on the shock surface, define a position vector $\mathbf{P}_s$ measured from the origin of the cylindrical system to a point on the shock surface. This vector may be expressed as

$$\mathbf{P}_s = x\mathbf{e}_x + r\mathbf{e}_r$$

where

$$r = f(x, \phi)$$

The derivative of this vector is

$$dP_s = \left(e_x + \frac{\partial f}{\partial x}e_r\right)dx + \left(e_\phi + \frac{1}{f}\frac{\partial f}{\partial \phi}e_r\right)fd\phi \qquad (B.1)$$

and since P_s is also a function of (ξ, β)

$$dP_s = \frac{\partial P_s}{\partial \xi}d\xi + \frac{\partial P_s}{\partial \beta}d\beta = e_\xi h_\xi\,d\xi + e_\beta h_\beta\,d\beta \qquad (B.2)$$

where

$$h_\xi e_\xi = \frac{\partial P_s}{\partial \xi} \qquad\qquad h_\beta e_\beta = \frac{\partial P_s}{\partial \beta} \qquad (B.3)$$

Taking the dot product of Eqs. (B.1) and (B.2) with e_x, equating, and noting that x is a function of (ξ, β) yields

$$\frac{\partial x}{\partial \xi} = e_\xi \cdot e_x h_\xi \qquad\qquad \frac{\partial x}{\partial \beta} = e_\beta \cdot e_x h_\beta \qquad (B.4)$$

Taking the dot product of Eqs. (B.1) and (B.2) with e_ϕ and equating gives

$$\frac{\partial \phi}{\partial \xi} = \frac{e_\xi \cdot e_\phi}{f}h_\xi \qquad\qquad \frac{\partial \phi}{\partial \beta} = \frac{e_\beta \cdot e_\phi}{f}h_\beta \qquad (B.5)$$

The transformation operators relating derivatives with respect to (ξ, β) to derivatives with respect to (x, ϕ) at the shock $(n = 0)$ may now be written, using Eq. (2.1.7) and Eqs. (B.4) and (B.5) as

$$\frac{1}{h_\xi}\frac{\partial}{\partial \xi} = \cos\Gamma\frac{\partial}{\partial x} - \frac{\sin\Gamma\sin\delta_\phi}{f}\frac{\partial}{\partial \phi} \qquad (B.6)$$

$$\frac{1}{h_\beta}\frac{\partial}{\partial \beta} = \frac{\cos\delta_\phi}{f}\frac{\partial}{\partial \phi} \qquad (B.7)$$

The transformation operators relating derivatives with respect to (ξ, β) to derivatives with respect to (y, z) at the shock are derived in a similar fashion by noting that

$$P_s = xe_x + ye_y + ze_z$$

where

$$x = g(y, z)$$

The transformation operators are given by

$$\frac{1}{h_\xi} \frac{\partial}{\partial \xi} = \sin\Gamma \left(\cos\sigma \frac{\partial}{\partial y} + \sin\sigma \frac{\partial}{\partial z} \right) \tag{B.8}$$

$$\frac{1}{h_\beta} \frac{\partial}{\partial \beta} = -\sin\sigma \frac{\partial}{\partial y} + \cos\sigma \frac{\partial}{\partial z} \tag{B.9}$$

Derivatives of the scale factors h_ξ and h_β with respect to the curvilinear coordinates may be derived from the fact that

$$\frac{\partial^2 \mathbf{P}}{\partial \xi \partial \beta} = \frac{\partial^2 \mathbf{P}}{\partial \beta \partial \xi}$$

Substitute Eq. (B.3) into the above equality to obtain

$$\frac{\partial h_\beta}{\partial \xi} \mathbf{e}_\beta + h_\beta \frac{\partial \mathbf{e}_\beta}{\partial \xi} = \frac{\partial h_\xi}{\partial \beta} \mathbf{e}_\xi + h_\xi \frac{\partial \mathbf{e}_\xi}{\partial \beta} \tag{B.10}$$

The dot product of Eq. (B.10) with $\mathbf{e}_\xi$ and $\mathbf{e}_\beta$ yields

$$\frac{\partial h_\xi}{\partial \beta} = h_\beta \frac{\partial \mathbf{e}_\beta}{\partial \xi} \cdot \mathbf{e}_\xi \qquad \frac{\partial h_\beta}{\partial \xi} = h_\xi \frac{\partial \mathbf{e}_\xi}{\partial \beta} \cdot \mathbf{e}_\beta \tag{B.11}$$

These relations may be simplified using Eq. (2.1.8) to obtain

$$\frac{1}{h_\xi h_\beta} \frac{\partial h_\xi}{\partial \beta} = -\frac{\sin\Gamma}{h_\xi} \frac{\partial \sigma}{\partial \xi} \qquad \frac{1}{h_\xi h_\beta} \frac{\partial h_\beta}{\partial \xi} = \frac{\sin\Gamma}{h_\beta} \frac{\partial \sigma}{\partial \beta} \tag{B.12}$$

B.2 Shock Layer

The transformation between the curvilinear coordinates (ξ, β, n) and the Cartesian coordinates (x, y, z) in the shock layer is given by

$$\mathbf{P} = \mathbf{P}_s + n \mathbf{e}_n$$

where **P** is a position vector from the origin of the Cartesian system to any point in the shock layer. Using Eq. (2.1.8), this becomes

$$x = x_s + n\sin\Gamma$$

$$y = y_s - n\cos\Gamma\cos\sigma \qquad\qquad\text{(B.13)}$$

$$z = z_s - n\cos\Gamma\sin\sigma$$

where all variables on the right hand side of the equations, with the exception of n, are functions of ξ and β. Subscripts are used to denote the shock coordinates.

Partial derivatives in the two coordinate systems are related by

$$\frac{\partial}{\partial\xi} = \left(\frac{\partial x}{\partial\xi}\right)\frac{\partial}{\partial x} + \left(\frac{\partial y}{\partial\xi}\right)\frac{\partial}{\partial y} + \left(\frac{\partial z}{\partial\xi}\right)\frac{\partial}{\partial z}$$

$$\frac{\partial}{\partial\beta} = \left(\frac{\partial x}{\partial\beta}\right)\frac{\partial}{\partial x} + \left(\frac{\partial y}{\partial\beta}\right)\frac{\partial}{\partial y} + \left(\frac{\partial z}{\partial\beta}\right)\frac{\partial}{\partial z}$$

$$\frac{\partial}{\partial n} = \left(\frac{\partial x}{\partial n}\right)\frac{\partial}{\partial x} + \left(\frac{\partial y}{\partial n}\right)\frac{\partial}{\partial y} + \left(\frac{\partial z}{\partial n}\right)\frac{\partial}{\partial z}$$

The metrics in the above equations may be found by taking the partial derivative of Eq. (B.13) with respect to the curvilinear coordinates and using Eqs. (B.6)–(B.9) for the derivatives of the shock coordinates. The metrics are given by

$$\frac{\partial x}{\partial\xi} = h_\xi \mathcal{A}\cos\Gamma$$

$$\frac{\partial x}{\partial\beta} = h_\beta \mathcal{D}\cos\Gamma \qquad\qquad\text{(B.14)}$$

$$\frac{\partial x}{\partial n} = \sin\Gamma$$

and

$$\frac{\partial y}{\partial\xi} = h_\xi\left(\mathcal{A}\sin\Gamma\cos\sigma - \mathcal{D}\sin\sigma\right)$$

$$\frac{\partial y}{\partial \beta} = h_\beta(-\mathcal{B}\sin\sigma + \mathcal{D}\sin\Gamma\cos\sigma) \qquad \text{(B.15)}$$

$$\frac{\partial y}{\partial n} = -\cos\Gamma\cos\sigma$$

and

$$\frac{\partial z}{\partial \xi} = h_\xi(\mathcal{A}\sin\Gamma\sin\sigma + \mathcal{D}\cos\sigma)$$

$$\frac{\partial z}{\partial \beta} = h_\beta(\mathcal{B}\cos\sigma + \mathcal{D}\sin\Gamma\sin\sigma) \qquad \text{(B.16)}$$

$$\frac{\partial z}{\partial n} = -\cos\Gamma\sin\sigma$$

where $\mathcal{A}$, $\mathcal{B}$, and $\mathcal{D}$ are geometric factors given by

$$\mathcal{A} = 1 - n\kappa_\xi$$

$$\mathcal{B} = 1 - n\kappa_\beta$$

$$\mathcal{D} = n\frac{1}{h_\beta}\frac{\partial \Gamma}{\partial \beta} = -n\frac{\cos\Gamma}{h_\xi}\frac{\partial \sigma}{\partial \xi}$$

and κ_ξ and κ_β represent the curvatures of the shock surface in the ξ-n and β-n planes, respectively. The curvatures may also be defined as

$$\kappa_\xi = -\frac{1}{h_\xi}\frac{\partial \Gamma}{\partial \xi} \qquad\qquad \kappa_\beta = \frac{\cos\Gamma}{h_\beta}\frac{\partial \sigma}{\partial \beta} \qquad \text{(B.17)}$$

The inverse transformation is represented by

$$\frac{\partial}{\partial x} = \left(\frac{\partial \xi}{\partial x}\right)\frac{\partial}{\partial \xi} + \left(\frac{\partial \beta}{\partial x}\right)\frac{\partial}{\partial \beta} + \left(\frac{\partial n}{\partial x}\right)\frac{\partial}{\partial n}$$

$$\frac{\partial}{\partial y} = \left(\frac{\partial \xi}{\partial y}\right)\frac{\partial}{\partial \xi} + \left(\frac{\partial \beta}{\partial y}\right)\frac{\partial}{\partial \beta} + \left(\frac{\partial n}{\partial y}\right)\frac{\partial}{\partial n}$$

$$\frac{\partial}{\partial z} = \left(\frac{\partial \xi}{\partial z}\right)\frac{\partial}{\partial \xi} + \left(\frac{\partial \beta}{\partial z}\right)\frac{\partial}{\partial \beta} + \left(\frac{\partial n}{\partial z}\right)\frac{\partial}{\partial n}$$

where the inverse metrics are given by

$$\frac{\partial \xi}{\partial x} = \frac{1}{\mathcal{J} h_\xi} \mathcal{B} \cos\Gamma$$

$$\frac{\partial \xi}{\partial y} = \frac{1}{\mathcal{J} h_\xi} (\mathcal{B} \sin\Gamma \cos\sigma + \mathcal{D} \sin\sigma) \qquad \text{(B.18)}$$

$$\frac{\partial \xi}{\partial z} = \frac{1}{\mathcal{J} h_\xi} (\mathcal{B} \sin\Gamma \sin\sigma - \mathcal{D} \cos\sigma)$$

and

$$\frac{\partial \beta}{\partial x} = \frac{-1}{\mathcal{J} h_\beta} \mathcal{D} \cos\Gamma$$

$$\frac{\partial \beta}{\partial y} = \frac{-1}{\mathcal{J} h_\beta} (\mathcal{A} \sin\sigma + \mathcal{D} \sin\Gamma \cos\sigma) \qquad \text{(B.19)}$$

$$\frac{\partial \beta}{\partial z} = \frac{1}{\mathcal{J} h_\beta} (\mathcal{A} \cos\sigma - \mathcal{D} \sin\Gamma \sin\sigma)$$

and

$$\frac{\partial n}{\partial x} = \frac{1}{\mathcal{J} h_\xi h_\beta} \sin\Gamma$$

$$\frac{\partial n}{\partial y} = \frac{-1}{\mathcal{J} h_\xi h_\beta} \cos\Gamma \cos\sigma \qquad \text{(B.20)}$$

$$\frac{\partial n}{\partial z} = \frac{-1}{\mathcal{J} h_\xi h_\beta} \cos\Gamma \sin\sigma$$

where $\mathcal{J}$ is a geometric factor related to the Jacobian of (x, y, z) with respect to (ξ, β, n) and is given by

$$\mathcal{J} = \mathcal{A}\mathcal{B} - \mathcal{D}^2$$

For the outer inviscid layer where the curvilinear coordinate system is assumed to be orthogonal, the geometric factors reduce to

$$\mathcal{A} = 1 - n\kappa_\xi$$

$$\mathcal{B} = 1 - n\kappa_\beta$$

$$\mathcal{D} = 0$$

$$\mathcal{J} = \mathcal{AB}$$

B.3 Body Surface

The transformation between the shock curvilinear coordinates (ξ,β) and the body curvilinear coordinates $(\bar{\xi},\bar{\beta})$ is found by defining a position vector to a point on the body surface as

$$\mathbf{P}_b = \mathbf{P}_s + n_b \mathbf{e}_n = x_b \mathbf{e}_x + y_b \mathbf{e}_y + z_b \mathbf{e}_z$$

where all variables are functions of (ξ, β). The Cartesian coordinates of the body are found from Eq. (B.13) with $n = n_b(\xi, \beta)$. The derivative of this vector is

$$d\mathbf{P}_b = \left(\frac{\partial x_b}{\partial \xi}\mathbf{e}_x + \frac{\partial y_b}{\partial \xi}\mathbf{e}_y + \frac{\partial z_b}{\partial \xi}\mathbf{e}_z\right) d\xi + \left(\frac{\partial x_b}{\partial \beta}\mathbf{e}_x + \frac{\partial y_b}{\partial \beta}\mathbf{e}_y + \frac{\partial z_b}{\partial \beta}\mathbf{e}_z\right) d\beta$$

Simplifying using Eqs. (B.14)–(B.16) and Eq. (2.1.8) yields

$$d\mathbf{P}_b = \left(\mathcal{A}_b \mathbf{e}_\xi + \mathcal{D}_b \mathbf{e}_\beta + \frac{1}{h_\xi}\frac{\partial n_b}{\partial \xi}\mathbf{e}_n\right) h_\xi \, d\xi + \left(\mathcal{D}_b \mathbf{e}_\xi + \mathcal{B}_b \mathbf{e}_\beta + \frac{1}{h_\beta}\frac{\partial n_b}{\partial \beta}\mathbf{e}_n\right) h_\beta \, d\beta \quad \text{(B.21)}$$

Since $\mathbf{P}_b$ is also a function of the surface coordinates $(\bar{\xi}, \bar{\beta})$, use Eq. (B.2) to obtain

$$d\mathbf{P}_b = \mathbf{e}_{\bar{\xi}} h_{\bar{\xi}} \, d\bar{\xi} + \mathbf{e}_{\bar{\beta}} h_{\bar{\beta}} \, d\bar{\beta} \quad \text{(B.22)}$$

Taking the dot product of Eqs. (B.21) and (B.22) with $\mathbf{e}_\xi$ and equating gives

$$\mathcal{A}_b h_\xi \, d\xi + \mathcal{D}_b h_\beta \, d\beta = \mathbf{e}_{\bar{\xi}} \cdot \mathbf{e}_\xi h_{\bar{\xi}} \, d\bar{\xi} + \mathbf{e}_{\bar{\beta}} \cdot \mathbf{e}_\xi h_{\bar{\beta}} \, d\bar{\beta}$$

Taking the dot product of Eqs. (B.21) and (B.22) with $\mathbf{e}_\beta$ and equating gives a similar result:

$$\mathcal{D}_b h_\xi \, d\xi + \mathcal{B}_b h_\beta \, d\beta = \mathbf{e}_{\bar{\xi}} \cdot \mathbf{e}_\beta h_{\bar{\xi}} \, d\bar{\xi} + \mathbf{e}_{\bar{\beta}} \cdot \mathbf{e}_\beta h_{\bar{\beta}} \, d\bar{\beta}$$

Solve for $d\xi$ and $d\beta$ to find

$$\mathcal{J}_b h_\xi \, d\xi = \left(\mathcal{B}_b \mathbf{e}_{\bar{\xi}} \cdot \mathbf{e}_\xi - \mathcal{D}_b \mathbf{e}_{\bar{\xi}} \cdot \mathbf{e}_\beta \right) h_{\bar{\xi}} \, d\bar{\xi} + \left(\mathcal{B}_b \mathbf{e}_{\bar{\beta}} \cdot \mathbf{e}_\xi - \mathcal{D}_b \mathbf{e}_{\bar{\beta}} \cdot \mathbf{e}_\beta \right) h_{\bar{\beta}} \, d\bar{\beta}$$

$$\mathcal{J}_b h_\beta \, d\beta = \left(\mathcal{A}_b \mathbf{e}_{\bar{\xi}} \cdot \mathbf{e}_\beta - \mathcal{D}_b \mathbf{e}_{\bar{\xi}} \cdot \mathbf{e}_\xi \right) h_{\bar{\xi}} \, d\bar{\xi} + \left(\mathcal{A}_b \mathbf{e}_{\bar{\beta}} \cdot \mathbf{e}_\beta - \mathcal{D}_b \mathbf{e}_{\bar{\beta}} \cdot \mathbf{e}_\xi \right) h_{\bar{\beta}} \, d\bar{\beta}$$

Noting that ξ and β are functions of $(\bar{\xi}, \bar{\beta})$ gives the transformation operators relating derivatives with respect to the shock coordinates (ξ, β) to derivatives with respect to the body coordinates $(\bar{\xi}, \bar{\beta})$ as

$$\frac{\mathcal{J}_b}{h_{\bar{\xi}}} \frac{\partial}{\partial \bar{\xi}} = \left(\mathcal{B}_b \mathbf{e}_{\bar{\xi}} \cdot \mathbf{e}_\xi - \mathcal{D}_b \mathbf{e}_{\bar{\xi}} \cdot \mathbf{e}_\beta \right) \frac{1}{h_\xi} \frac{\partial}{\partial \xi} + \left(\mathcal{A}_b \mathbf{e}_{\bar{\xi}} \cdot \mathbf{e}_\beta - \mathcal{D}_b \mathbf{e}_{\bar{\xi}} \cdot \mathbf{e}_\xi \right) \frac{1}{h_\beta} \frac{\partial}{\partial \beta} \qquad \text{(B.23)}$$

and

$$\frac{\mathcal{J}_b}{h_{\bar{\beta}}} \frac{\partial}{\partial \bar{\beta}} = \left(\mathcal{B}_b \mathbf{e}_{\bar{\beta}} \cdot \mathbf{e}_\xi - \mathcal{D}_b \mathbf{e}_{\bar{\beta}} \cdot \mathbf{e}_\beta \right) \frac{1}{h_\xi} \frac{\partial}{\partial \xi} + \left(\mathcal{A}_b \mathbf{e}_{\bar{\beta}} \cdot \mathbf{e}_\beta - \mathcal{D}_b \mathbf{e}_{\bar{\beta}} \cdot \mathbf{e}_\xi \right) \frac{1}{h_\beta} \frac{\partial}{\partial \beta} \qquad \text{(B.24)}$$

These transformation operators allow equations in the body coordinate system to be transformed to the shock coordinate system.

C   Shock Properties

The properties at the shock surface are determined by applying the normal shock relations with the upstream velocity equal to the normal component of the freestream velocity. In the curvilinear coordinate system (ξ, β, n), the freestream velocity components are

$$u'_\infty = V'_\infty \mathbf{e}_x \cdot \mathbf{e}_\xi \qquad v'_\infty = V'_\infty \mathbf{e}_x \cdot \mathbf{e}_n \qquad w'_\infty = V'_\infty \mathbf{e}_x \cdot \mathbf{e}_\beta$$

Using Eq. (2.1.7), these velocity components become

$$u'_\infty = V'_\infty \cos \Gamma \qquad v'_\infty = V'_\infty \sin \Gamma \qquad w'_\infty = 0$$

The tangential velocity u' is conserved across the shock surface so that

$$u'_s = u'_\infty = V'_\infty \cos\Gamma$$

The governing equations (continuity, momentum, and energy) for the equilibrium or frozen flow across a normal shock are now applied using the normal velocity component v'. They are

$$\rho'_\infty v'_\infty = \rho'_s v'_s$$

$$p'_\infty + \rho'_\infty v'^2_\infty = p'_s + \rho'_s v'^2_s$$

$$h'_\infty + \frac{v'^2_\infty}{2} = h'_s + \frac{v'^2_s}{2}$$

Transforming to nondimensional variables (see Appendix A) yields

$$u_s = \cos\Gamma \qquad\qquad (C.1)$$

$$\rho_s v_s \;=\; \sin\Gamma \qquad\qquad\qquad (C.2)$$

$$p_s + \rho_s v_s^2 \;=\; p_\infty + \sin^2\Gamma \qquad\qquad\qquad (C.3)$$

$$h_s + \frac{v_s^2}{2} \;=\; h_\infty + \frac{\sin^2\Gamma}{2} \qquad\qquad\qquad (C.4)$$

For closure of this set of equations, an equation of state is needed. For both equilibrium and perfect gas flows, this is in the form of

$$\rho_s = \rho_s(p_s, h_s)$$

C.1   Perfect Gas

For a perfect gas, the equation of state involving pressure, density, and enthalpy is given by

$$h' = \frac{\gamma}{\gamma - 1}\frac{p'}{\rho'}$$

At the shock (in nondimensional form),

$$h_s = \frac{\gamma}{\gamma - 1}\frac{p_s}{\rho_s} \qquad\qquad\qquad (C.5)$$

Now solve Eqs. (C.2)–(C.5) to obtain the shock properties for a perfect gas. They are

$$p_s = \frac{2\sin^2\Gamma}{\gamma + 1} - \frac{\gamma - 1}{\gamma(\gamma + 1)M_\infty^2} \qquad\qquad\qquad (C.6)$$

$$\rho_s = \frac{(\gamma + 1)M_\infty^2 \sin^2\Gamma}{(\gamma - 1)M_\infty^2 \sin^2\Gamma + 2} \qquad\qquad\qquad (C.7)$$

$$v_s = \frac{\sin\Gamma}{\rho_s} \qquad\qquad\qquad (C.8)$$

with h_s defined above.

C.2 Equilibrium

For a flow in thermodynamic and chemical equilibrium, the equation of state is given by

$$\rho' = \rho'(p', h') \tag{C.9}$$

This relation is typically evaluated through the use of tables or curve-fits of data. Unlike the shock properties for a perfect gas, shock properties for an equilibrium flow cannot be determined explicitly. An iterative numerical solution is required. Substitute Eq. (C.2) into Eqs. (C.3) and (C.4) to obtain

$$p_s = p_\infty + \sin^2\Gamma \left(1 - \frac{1}{\rho_s} \right) \tag{C.10}$$

$$h_s = h_\infty + \frac{\sin^2\Gamma}{2} \left(1 - \frac{1}{\rho_s^2} \right) \tag{C.11}$$

The iterative procedure is as follows:

1. Assume a value for ρ_s. A typical value is 10.

2. Calculate p_s and h_s from Eqs. (C.10) and (C.11).

3. Calculate a new value for ρ_s from the equation of state, Eq. (C.9).

4. Repeat steps 2 and 3 until the difference between the new and old values for ρ_s is within a prescribed tolerance.

5. Calculate the normal velocity v_s from Eq. (C.2).

D   Inviscid Stagnation Region

Because the governing inviscid flowfield equations are indeterminate on the stagnation line (origin of wind-oriented coordinate system), a limiting solution is developed in the surrounding region. This solution then provides the initial location of a shock line and the shock standoff distance on the stagnation line. A similar approach for surface streamlines in the stagnation region is found in Ref. [8].

D.1   Shock Line Geometry

An analytic solution describing the curvilinear coordinate geometry in the stagnation region may be found by neglecting x^2 and xr in the shock surface equations, Eqs. (2.3.2) and (2.3.3). For convenience, use Cartesian coordinates and describe the shock surface by an elliptic paraboloid as

$$By^2 + z^2 = 2cx \qquad \text{(D.1)}$$

where

$$c = R_z \qquad\qquad B = \frac{R_z}{R_y}$$

and the shock radius of curvature at the origin is R_y in the $x - y$ plane and R_z in the $x - z$ plane. Now define

$$F(x, y, z) \equiv By^2 + z^2 - 2cx = 0$$

Using Eq. (2.1.3), the unit vector normal to the shock surface can be calculated:

$$\mathbf{e}_n = \frac{c\mathbf{e}_x - By\mathbf{e}_y - z\mathbf{e}_z}{(c^2 + B^2y^2 + z^2)^{1/2}} \qquad (D.2)$$

The shock angles Γ and σ may be determined by comparing Eqs. (D.2) and (2.1.8). They are given by

$$\tan\Gamma = \frac{c}{(B^2y^2 + z^2)^{1/2}} \qquad \tan\sigma = \frac{z}{By} \qquad (D.3)$$

The equation for a shock line is found by applying the transformation operator, Eq. (B.8), to yield

$$\frac{\partial z/\partial \xi}{\partial y/\partial \xi} = \tan\sigma = \frac{z}{By}$$

Integrate to find

$$z^B = Cy \qquad (D.4)$$

where the parameter C is a function of β and distinguishes one shock line from another. The behavior of the shock lines near the origin is illustrated by examining the slope and location of the shock lines:

$$\frac{dz}{dy} = \tan\sigma = \frac{Cz^{1-B}}{B} \qquad \frac{z}{y} = \tan\phi = Cz^{1-B}$$

For $B = 1$ (axisymmetric), the shock lines emanate radially from the stagnation line. However, if C is finite and non-zero and B is not equal to one, the shock lines emanate from $\phi = 90$ deg for $B > 1$ and from $\phi = 0$ deg and $\phi = 180$ deg for $B < 1$. The shock lines for $B > 1$ are shown in Fig. D.1. For $B < 1$, the same pattern is simply rotated 90 deg.
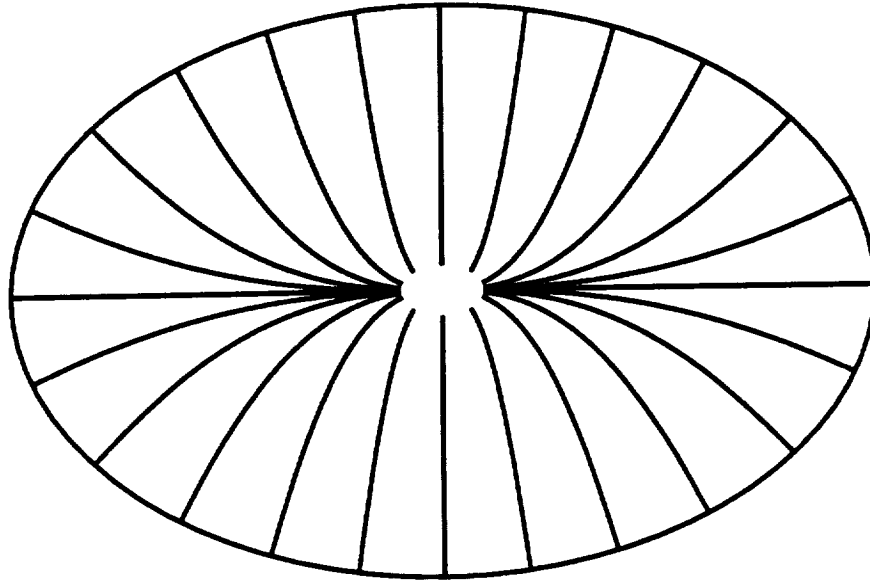
Figure D.1. Stagnation region shock lines $(B > 1)$: front view.

The scale factor at the shock may be found by substituting the equation defining

a shock line, Eq. (D.4), into the transformation operator, Eq. (B.9), to yield

$$h_\beta = \frac{C'}{C} \frac{yz}{(B^2 y^2 + z^2)^{1/2}} \qquad (D.5)$$

where

$$C' \equiv \frac{dC}{d\beta}$$

An explicit expression for the stream function at the shock may be obtained from

Eq. (2.2.3) and (C.2) as

$$\Psi_s = \int_0^\xi \sin\Gamma h_\beta h_\xi \, d\xi$$

The transformation operators, Eqs. (B.8) and (B.9), are used to calculate the differ-

ential along a shock line as

$$d\xi = \frac{(B^2 y^2 + z^2)^{1/2}}{h_\xi \sin\Gamma} \frac{dz}{z} \tag{D.6}$$

Substitute Eqs. (D.5) and (D.6) into the equation for the stream function Ψ_s and

integrate to yield

$$\Psi_s = \frac{C'}{C} \frac{yz}{B+1} \tag{D.7}$$

To determine the parameter $C(\beta)$, an arbitrary value of β is assigned to each

shock line at a point in the stagnation region. The convention used here is to relate

β to the circumferential angle ϕ. Thus, the initial location of a shock line is found by

defining

$$\epsilon^2 = 2cx_\epsilon \qquad\qquad \beta = \phi_\epsilon$$

where ϵ is a constant with a typical value between 0.01 and 0.10 and shock lines may

be arbitrarily distributed around the shock surface at x_ϵ. From Eq. (D.1)

$$y_\epsilon = \frac{\epsilon\cos\beta}{(B\cos^2\beta + \sin^2\beta)^{1/2}} \qquad\qquad z_\epsilon = \frac{\epsilon\sin\beta}{(B\cos^2\beta + \sin^2\beta)^{1/2}} \tag{D.8}$$

Substitute into Eq. (D.4) to find

$$C = \frac{\sin^B\beta}{\cos\beta} \left(\frac{\epsilon^2}{B\cos^2\beta + \sin^2\beta} \right)^{\frac{B-1}{2}}$$

and

$$\frac{C'}{C} = \frac{1}{\sin\beta\cos\beta} \left(\frac{B^2\cos^2\beta + \sin^2\beta}{B\cos^2\beta + \sin^2\beta} \right)$$

The shock curvatures κ_ξ and κ_β appear in the approximate pressure equation and

in the geometric factors that define the coordinate transformation across the layer.

They are calculated from the derivatives of the shock angles Γ and σ as

$$\kappa_\xi = -\frac{1}{h_\xi}\frac{\partial\Gamma}{\partial\xi} \qquad\qquad \kappa_\beta = \frac{\cos\Gamma}{h_\beta}\frac{\partial\sigma}{\partial\beta} \qquad\qquad (D.9)$$

Using Eq. (D.3), the shock angle derivatives become

$$\frac{\partial\Gamma}{\partial y} = -\frac{B^2 y \sin^3\Gamma}{c^2\cos\Gamma} \qquad\qquad \frac{\partial\Gamma}{\partial z} = -\frac{z\sin^3\Gamma}{c^2\cos\Gamma} \qquad\qquad (D.10)$$

and

$$\frac{\partial\sigma}{\partial y} = -\frac{Bz}{B^2 y^2 + z^2} \qquad\qquad \frac{\partial\sigma}{\partial z} = \frac{By}{B^2 y^2 + z^2} \qquad\qquad (D.11)$$

Substitute into the transformation operators, Eqs. (B.8) and (B.9), to obtain

$$\kappa_\xi = \frac{\sin^3\Gamma}{c}\left(\frac{B^3 y^2 + z^2}{B^2 y^2 + z^2}\right) \qquad\qquad \kappa_\beta = \frac{B\sin\Gamma}{c}\left(\frac{By^2 + z^2}{B^2 y^2 + z^2}\right) \qquad\qquad (D.12)$$

D.2   Shock Standoff Distance

The shock standoff distance on the stagnation line is calculated from Eq. (2.2.15)

as

$$n_{b_0} - \frac{n_{b_0}^2 \kappa_\beta}{2} = \int_0^1 \frac{d\eta}{\rho\lim\limits_{\xi\to 0}\left(\dfrac{u h_\beta}{\Psi_s}\right)} \qquad\qquad (D.13)$$

where the velocity term $\dfrac{u h_\beta}{\Psi_s}$ is indeterminate along the stagnation line and is found

from the flowfield equations in the stagnation region. This analysis follows the ap-

proach of Ref. [9]. However, the complete energy equation and a more accurate

pressure relation are used here.

The tangential velocity u is obtained from the energy equation Eq. (2.2.12):

$$h + \frac{1}{2}(u^2 + v^2) = h_{s_0} + \frac{1}{2}v_{s_0}^2 = H_\infty \qquad\qquad (D.14)$$

Before u can be calculated, analytic expressions are needed for the flowfield properties. Since enthalpy is a function of pressure and entropy, expand about the position where the streamline crosses the shock to give

$$h(\xi, \beta, \Psi) \approx h_s(\beta, \Psi) + \left(\frac{\partial h}{\partial p}\right)_s [p(\xi, \beta, \Psi) - p_s(\beta, \Psi)] \qquad (D.15)$$

where

$$\left(\frac{\partial h}{\partial p}\right)_s = \frac{1}{\rho_s(\beta, \Psi)}$$

from the first and second laws of thermodynamics. Since density is a function of pressure and enthalpy, expand about the normal shock position to obtain

$$\frac{1}{\rho_s(\beta, \Psi)} \approx \frac{1}{\rho_{s_0}} + \left[\frac{\partial(1/\rho)}{\partial p}\right]_{s_0} [p_s(\beta, \Psi) - p_{s_0}] + \left[\frac{\partial(1/\rho)}{\partial h}\right]_{s_0} [h_s(\beta, \Psi) - h_{s_0}] \quad (D.16)$$

The pressure and normal velocity component across the layer appear in the enthalpy relation and energy equation, respectively, and are given by Eqs. (2.2.10) and (2.2.11) as

$$p(\xi, \beta, \Psi) = p_s(\xi, \beta) + p_1(\xi, \beta) [\eta - 1] + p_2(\xi, \beta) \left[\eta^2 - 1\right] \qquad (D.17)$$

$$v(\xi, \beta, \Psi) = v_s(\xi, \beta) + v_1(\xi, \beta) [\eta - 1] \qquad (D.18)$$

where

$$p_1 = \frac{\sin^2\Gamma \cos^2\Gamma}{B + 1} \left(\frac{B^3 y^2 + z^2}{B^2 y^2 + z^2}\right)$$

$$p_2 = -\frac{\sin^2\Gamma}{2(B + 1)\rho_s} \left[\sin^2\Gamma \left(\frac{B^3 y^2 + z^2}{B^2 y^2 + z^2}\right) + B \left(\frac{B y^2 + z^2}{B^2 y^2 + z^2}\right)\right]$$

$$v_1 = \frac{\sin\Gamma}{(B + 1)\rho_s} \left[\sin^2\Gamma \left(\frac{B^3 y^2 + z^2}{B^2 y^2 + z^2}\right) + B \left(\frac{B y^2 + z^2}{B^2 y^2 + z^2}\right)\right]$$

and

$$\eta \equiv \frac{\Psi}{\Psi_s}$$

The shock wave geometry in the stagnation region has been used to simplify these pressure and velocity expressions.

Now define the variables at the shock in terms of the shock angle Γ such that

$$\cos \Gamma \equiv G$$

$$\sin^2 \Gamma \equiv 1 - G^2 \tag{D.19}$$

$$p_s \equiv p_{s_0} - \Delta p G^2 \tag{D.20}$$

$$h_s \equiv h_{s_0} - \Delta h G^2 \tag{D.21}$$

where in the stagnation region

$$G^2 \ll 1 \qquad \Delta p G^2 \ll 1 \qquad \Delta h G^2 \ll 1$$

Substitute into Eq. (D.16) to yield

$$\frac{1}{\rho_s} \approx \frac{1}{\rho_{s_0}} - \Delta(1/\rho) G^2 \tag{D.22}$$

where

$$\Delta(1/\rho) = \left[\frac{\partial(1/\rho)}{\partial p}\right]_{s_0} \Delta p + \left[\frac{\partial(1/\rho)}{\partial h}\right]_{s_0} \Delta h \tag{D.23}$$

The quantities Δp, Δh, and $\Delta(1/\rho)$ are related to the shock gradients of the respective properties and may be calculated from the shock properties for either a perfect gas or an equilibrium flow. Their derivation will be detailed in a subsequent section.

Next substitute Eqs. (D.15)-(D.23) into the energy equation, Eq. (D.14), and neglect higher order terms to obtain for the velocity

$$
\begin{aligned}
u^2(\xi, \beta, \Psi) &= \frac{G^2(\xi, \beta)}{\rho_{s_0}} \left\{ -\frac{1}{B+1} \left(\frac{B^3 y^2 + z^2}{B^2 y^2 + z^2} \right) (\eta - 1) \left[2 - \frac{1}{\rho_{s_0}} (\eta - 1) \right] \right. \\
&\qquad \left. + 2\Delta p + \frac{1}{\rho_{s_0}} + \Delta(1/\rho) \left(\eta^2 + 1 \right) \right\} \\
&\quad + \frac{G^2(\beta, \Psi)}{\rho_{s_0}} \left\{ 2\rho_{s_0} \Delta h - 2\Delta p - \Delta(1/\rho) \left(\eta^2 - 1 \right) \right\} \qquad \text{(D.24)}
\end{aligned}
$$

Recall that (ξ, β) refers to the shock location along a line normal to the shock and (β, Ψ) refers to the position where a streamline crosses the shock. Evaluate $G^2(\xi, \beta)$ from the shock line geometry as

$$
\lim_{y, z \to 0} \frac{h_\beta^2 G^2(\xi, \beta)}{\Psi_s^2} = \frac{(B+1)^2}{c^2} \qquad \text{(D.25)}
$$

Determine $G^2(\beta, \Psi)$ from the approximation that the shock angle Γ varies linearly with the stream function Ψ along shock lines. This approximation is employed throughout the flowfield and implies

$$
\sin\Gamma(\beta, \Psi) \approx 1 + [\sin\Gamma(\xi, \beta) - 1]\eta
$$

Substituting Eq. (D.19) gives

$$
\lim_{y, z \to 0} \frac{h_\beta^2 G^2(\beta, \Psi)}{\Psi_s^2} \approx \lim_{y, z \to 0} \frac{h_\beta^2 G^2(\xi, \beta)}{\Psi_s^2} \eta = \frac{(B+1)^2}{c^2} \eta \qquad \text{(D.26)}
$$

The ratio of shock coordinates that appears in the velocity expression is evaluated by substituting Eq. (D.4) for the coordinate y and taking the limit as the coordinate z

approaches zero to yield

$$D \equiv \lim_{z \to 0} \left(\frac{B^3 y^2 + z^2}{B^2 y^2 + z^2} \right) = \begin{cases} B & B \leq 1 \\ \\ 1 & B > 1 \end{cases} \qquad (D.27)$$

The limit of the shock curvature κ_β at the origin is found in a similar manner as

$$\kappa_{\beta_0} = \lim_{z \to 0} \frac{B \sin \Gamma}{c} \left(\frac{B y^2 + z^2}{B^2 y^2 + z^2} \right) = \begin{cases} \frac{1}{c} & B \leq 1 \\ \\ \frac{B}{c} & B > 1 \end{cases} \qquad (D.28)$$

Substitute Eqs. (D.24)–(D.28) into Eq. (D.13) and simplify to yield for the stagnation shock standoff distance

$$n_{b_0} \kappa_{\beta_0} = 1 - \left[1 - 2\kappa_{\beta_0} \frac{c}{B+1} \rho_{s_0}^{1/2} \int_0^1 \frac{d\eta}{\rho \left(u_0 + \eta u_1 \right)^{1/2}} \right]^{1/2} \qquad (D.29)$$

where

$$u_0 = -\frac{D}{B+1} (\eta - 1) \left[2 - \frac{1}{\rho_{s_0}} (\eta - 1) \right] + 2\Delta p + \frac{1}{\rho_{s_0}} + \Delta(1/\rho) \left(\eta^2 + 1 \right)$$

$$u_1 = 2\rho_{s_0} \Delta h - 2\Delta p - \Delta(1/\rho) \left(\eta^2 - 1 \right)$$

Note that the density is calculated from the equation of state as

$$\rho = \rho(p, S_0)$$

Expressions for the shock gradients Δp, Δh, and $\Delta(1/\rho)$ are given below.

D.3   Shock Gradients

Substitute for the shock values of pressure and enthalpy in the shock relations Eqs. (C.3) and (C.4) to obtain

$$p_{s_0} - \Delta p G^2 = p_\infty + (1 - G^2)(1 - \frac{1}{\rho_s})$$

$$h_{s_0} - \Delta h G^2 = h_\infty + \frac{1}{2}(1 - G^2)(1 - \frac{1}{\rho_s^2})$$

Now substitute for the density with Eq. (D.23) and neglect higher order terms to obtain

$$\Delta p = -\left[\frac{\partial(1/\rho)}{\partial p}\right]_{s_0} \Delta p - \left[\frac{\partial(1/\rho)}{\partial h}\right]_{s_0} \Delta h + 1 - \frac{1}{\rho_{s_0}}$$

$$\Delta h = \frac{1}{\rho_{s_0}} \left\{ -\left[\frac{\partial(1/\rho)}{\partial p}\right]_{s_0} \Delta p - \left[\frac{\partial(1/\rho)}{\partial h}\right]_{s_0} \Delta h \right\} + \frac{1}{2}\left(1 - \frac{1}{\rho_{s_0}^2}\right)$$

Solve for Δp and Δh to yield

$$\Delta p = \frac{1}{I}\left[\left(1 - \frac{1}{\rho_{s_0}}\right)\left\{1 + \frac{1}{\rho_{s_0}}\left[\frac{\partial(1/\rho)}{\partial h}\right]_{s_0}\right\} - \frac{1}{2}\left[\frac{\partial(1/\rho)}{\partial h}\right]_{s_0}\left(1 - \frac{1}{\rho_{s_0}^2}\right)\right] \quad \text{(D.30)}$$

$$\Delta h = \frac{1}{I}\left[\frac{1}{2}\left(1 - \frac{1}{\rho_{s_0}^2}\right)\left\{1 + \left[\frac{\partial(1/\rho)}{\partial p}\right]_{s_0}\right\} - \frac{1}{\rho_{s_0}}\left[\frac{\partial(1/\rho)}{\partial p}\right]_{s_0}\left(1 - \frac{1}{\rho_{s_0}}\right)\right] \quad \text{(D.31)}$$

where

$$I = 1 + \left[\frac{\partial(1/\rho)}{\partial p}\right]_{s_0} + \frac{1}{\rho_{s_0}}\left[\frac{\partial(1/\rho)}{\partial h}\right]_{s_0}$$

The density derivatives can be calculated explicitly for a perfect gas from

$$\frac{1}{\rho} = \frac{\gamma - 1}{\gamma}\frac{h}{p}$$

to yield

$$\frac{\partial(1/\rho)}{\partial p} = -\frac{1}{\rho p} \qquad \frac{\partial(1/\rho)}{\partial h} = \frac{1}{\rho h}$$

For an equilibrium gas, these derivatives must be calculated numerically.

E   Numerical Integration Scheme

The scheme used to numerically integrate the shock line and surface streamline variables is a variable-step size, second-order, predictor-corrector, ordinary differential equation solver. To illustrate the scheme for a single equation, let y be the dependent variable, x be the independent variable, f be the derivative of y with respect to x, and h be the step size in x. Then the predictor step gives

$$y_i^p = y_{i-1}^c + \frac{h}{2}(3f_{i-1} - f_{i-2})$$

whereas the corrector step yields

$$y_i^c = y_{i-1}^c + \frac{h}{2}(f_i + f_{i-1})$$

where the index i represents the current x location. The local truncation error e is estimated by the difference in the predicted and corrected values as

$$e = |y_p - y_c|$$

The step size h is varied such that the error e remains below a prescribed tolerance.

Initial conditions for the predictor-corrector scheme are calculated from a second-order Runge-Kutta scheme given by

$$y_i = y_{i-1} + hk_2$$

where

$$k_1 = f(x_{i-1}, y_{i-1}) \qquad k_2 = f(x_{i-1} + \frac{h}{2}, y_{i-1} + \frac{h}{2}k_1)$$

F Body Geometry

In Sec. 3.2, the surface streamline equations require body geometry angles that are referenced to the wind axes. However, reentry vehicle geometries are typically described with respect to the body axis as in Ref. [26]. The transformation from a body-oriented to a wind-oriented coordinate system and its application are detailed here for a 3-D body.

The 3-D body surface may be described in the body-oriented system by

$$\bar{r} = \bar{f}(\bar{x}, \bar{\phi})$$

and in the wind axes by

$$r = f(x, \phi)$$

The two sets of axes are shown in Fig. 2.5. No subscripts are used here since all variables apply to the body surface.

The body angles are defined by Eq. (2.1.2) such that in the body axes

$$\tan\bar{\delta}_\phi = \frac{1}{\bar{f}}\frac{\partial\bar{f}}{\partial\bar{\phi}} \qquad \tan\bar{\Gamma} = \frac{\partial\bar{f}}{\partial\bar{x}}\cos\bar{\delta}_\phi \qquad \bar{\sigma} = \bar{\phi} - \bar{\delta}_\phi \qquad (F.1)$$

and in the wind axes

$$\tan\delta_\phi = \frac{1}{f}\frac{\partial f}{\partial\phi} \qquad \tan\Gamma = \frac{\partial f}{\partial x}\cos\delta_\phi \qquad \sigma = \phi - \delta_\phi \qquad (F.2)$$

For later use, derivatives of these angles with respect to the body axis coordinates

are needed. They are given by

$$\frac{\partial \bar{\delta}_\phi}{\partial \bar{x}} = \cos^2 \bar{\delta}_\phi \left[\frac{1}{\bar{f}} \frac{\partial^2 \bar{f}}{\partial \bar{x} \partial \phi} - \left(\frac{1}{\bar{f}} \frac{\partial \bar{f}}{\partial \phi} \right) \frac{1}{\bar{f}} \frac{\partial \bar{f}}{\partial \bar{x}} \right] \tag{F.3}$$

$$\frac{1}{\bar{f}} \frac{\partial \bar{\delta}_\phi}{\partial \phi} = \frac{\cos^2 \bar{\delta}_\phi}{\bar{f}} \left[\frac{1}{\bar{f}} \frac{\partial^2 \bar{f}}{\partial \bar{\phi}^2} - \left(\frac{1}{\bar{f}} \frac{\partial \bar{f}}{\partial \phi} \right)^2 \right] \tag{F.4}$$

and

$$\frac{\partial \bar{\sigma}}{\partial \bar{x}} = -\frac{\partial \bar{\delta}_\phi}{\partial \bar{x}} \tag{F.5}$$

$$\frac{1}{\bar{f}} \frac{\partial \bar{\sigma}}{\partial \phi} = \frac{1}{\bar{f}} - \frac{1}{\bar{f}} \frac{\partial \bar{\delta}_\phi}{\partial \bar{\phi}} \tag{F.6}$$

and

$$\frac{\partial \bar{\Gamma}}{\partial \bar{x}} = \cos^2 \bar{\Gamma} \left(\frac{\partial^2 \bar{f}}{\partial \bar{x}^2} \cos \bar{\delta}_\phi - \frac{\partial \bar{f}}{\partial \bar{x}} \sin \bar{\delta}_\phi \frac{\partial \bar{\delta}_\phi}{\partial \bar{x}} \right) \tag{F.7}$$

$$\frac{1}{\bar{f}} \frac{\partial \bar{\Gamma}}{\partial \phi} = \cos^2 \bar{\Gamma} \left[\frac{1}{\bar{f}} \frac{\partial^2 \bar{f}}{\partial \bar{x} \partial \bar{\phi}} \cos \bar{\delta}_\phi - \frac{\partial \bar{f}}{\partial \bar{x}} \sin \bar{\delta}_\phi \left(\frac{1}{\bar{f}} \frac{\partial \bar{\delta}_\phi}{\partial \phi} \right) \right] \tag{F.8}$$

The unit vector normal to the body surface is calculated from Eq. (2.1.3). In the body axes, the vector becomes

$$\mathbf{e}_{\bar{n}} = -\sin \bar{\Gamma} \mathbf{e}_{\bar{x}} + \cos \bar{\Gamma} \cos \bar{\sigma} \mathbf{e}_{\bar{y}} + \cos \bar{\Gamma} \sin \bar{\sigma} \mathbf{e}_{\bar{z}} \tag{F.9}$$

and similarly in the wind axes

$$\mathbf{e}_{\bar{n}} = -\sin \Gamma \mathbf{e}_x + \cos \Gamma \cos \sigma \mathbf{e}_y + \cos \Gamma \sin \sigma \mathbf{e}_z \tag{F.10}$$

Referring to Fig. 2.5, the two systems are related in Cartesian coordinates by

$$\mathbf{e}_{\bar{x}} = \cos \alpha \mathbf{e}_x + \sin \alpha \mathbf{e}_y$$

$$\mathbf{e}_{\bar{y}} = -\sin \alpha \mathbf{e}_x + \cos \alpha \mathbf{e}_y \tag{F.11}$$

$$\mathbf{e}_{\bar{z}} = \mathbf{e}_z$$

and

$$\bar{x} = \bar{x}_0 + \left(x - n_{b_0}\right)\cos\alpha + y\sin\alpha$$

$$\bar{y} = \bar{y}_0 - \left(x - n_{b_0}\right)\sin\alpha + y\cos\alpha \qquad \text{(F.12)}$$

$$\bar{z} = z$$

where $(\bar{x}_0, \bar{y}_0)$ is the stagnation point on the body and n_{b_0} is the shock standoff distance on the stagnation line. The stagnation point is assumed to be the Newtonian stagnation point located by

$$\mathbf{V}_\infty \cdot \mathbf{e}_{\bar{n}} = -1$$

Noting that $\mathbf{V}_\infty = \mathbf{e}_x$ and substituting Eq. (F.9) and Eq. (F.11) gives

$$\sin\bar{\Gamma}_0 = \cos\alpha$$

The stagnation point can then be calculated from the definition of $\bar{\Gamma}$.

The body radius $\bar{f}$ is assumed to be a known function of the body axis coordinates $(\bar{x}, \bar{\phi})$. However, the body location is given by its wind axis coordinates (x, ϕ) obtained from Eq. (B.13) with $n = n_b$. Before calculating $\bar{f}$, transform the wind-oriented coordinates to the corresponding body axis coordinates using Eq. (F.12). Then from either an analytic expression such as Eq. (2.3.1) or a geometry package such as the one detailed in Ref. [26], the body radius $\bar{f}$ may be computed along with its first and second derivatives with respect to $\bar{x}$ and $\bar{\phi}$. The body angles and their derivatives with respect to the body axes are then calculated from Eq. (F.1) and Eqs. (F.3)–(F.8).

To obtain the surface angles with respect to the wind axes, substitute Eq. (F.11) into Eq. (F.9) and equate with Eq. (F.10) to yield

$$\sin\Gamma = \cos\alpha \sin\bar{\Gamma} + \sin\alpha \cos\bar{\Gamma} \cos\bar{\sigma}$$

$$\cos\Gamma \cos\sigma = -\sin\alpha \sin\bar{\Gamma} + \cos\alpha \cos\bar{\Gamma} \cos\bar{\sigma} \qquad \text{(F.13)}$$

$$\cos\Gamma \sin\sigma = \cos\bar{\Gamma} \sin\bar{\sigma}$$

Differentiate to obtain

$$\cos^2\Gamma \, d\sigma = (\cos\alpha \cos\bar{\Gamma} - \sin\alpha \sin\bar{\Gamma} \cos\bar{\sigma}) \cos\bar{\Gamma} \, d\bar{\sigma} + (\sin\alpha \sin\bar{\sigma}) \, d\bar{\Gamma}$$

$$\cos\Gamma \, d\Gamma = (\cos\alpha \cos\bar{\Gamma} - \sin\alpha \sin\bar{\Gamma} \cos\bar{\sigma}) \, d\bar{\Gamma} - (\sin\alpha \sin\bar{\sigma}) \cos\bar{\Gamma} \, d\bar{\sigma}$$

where the differential represents both

$$\frac{\partial}{\partial \bar{x}} \qquad \qquad \frac{1}{\bar{f}} \frac{\partial}{\partial \bar{\phi}}$$

All terms on the right-hand side of these equations are known.

Before transforming these derivatives with respect to the body axes to derivatives with respect to the wind axes, transformation operators are needed. Following the procedure of Appendix B, define a position vector from the origin of the shock-oriented system to a point on the body surface as

$$\mathbf{P} = \mathbf{P}_0 + \bar{x}\mathbf{e}_{\bar{x}} + \bar{f}\mathbf{e}_{\bar{r}} = x\mathbf{e}_x + f\mathbf{e}_r$$

The analysis of Appendix B gives the transformation operators relating derivatives in the body axis coordinates $(\bar{x}, \bar{\phi})$ to derivatives with respect to the shock-oriented

coordinates (x,ϕ) as

$$\frac{\partial}{\partial x} = \left(\frac{\partial \bar{x}}{\partial x}\right)\frac{\partial}{\partial \bar{x}} + \left(\bar{f}\frac{\partial \bar{\phi}}{\partial x}\right)\frac{1}{\bar{f}}\frac{\partial}{\partial \bar{\phi}} \tag{F.14}$$

$$\frac{1}{f}\frac{\partial}{\partial \phi} = \left(\frac{1}{f}\frac{\partial \bar{x}}{\partial \phi}\right)\frac{\partial}{\partial \bar{x}} + \left(\frac{\bar{f}}{f}\frac{\partial \bar{\phi}}{\partial \phi}\right)\frac{1}{\bar{f}}\frac{\partial}{\partial \bar{\phi}} \tag{F.15}$$

where

$$\frac{\partial \bar{x}}{\partial x} = \cos\alpha + \frac{\partial f}{\partial x}(\sin\alpha\,\cos\phi)$$

$$\bar{f}\frac{\partial \bar{\phi}}{\partial x} = \sin\alpha\,\sin\bar{\phi} + \frac{\partial f}{\partial x}(-\cos\alpha\,\sin\bar{\phi}\,\cos\phi + \cos\bar{\phi}\,\sin\phi)$$

$$\frac{1}{f}\frac{\partial \bar{x}}{\partial \phi} = -\sin\alpha\,\sin\phi + \frac{1}{f}\frac{\partial f}{\partial \phi}(\sin\alpha\,\cos\phi)$$

$$\frac{\bar{f}}{f}\frac{\partial \bar{\phi}}{\partial \phi} = \cos\alpha\,\sin\bar{\phi}\,\sin\phi + \cos\bar{\phi}\,\cos\phi + \frac{1}{f}\frac{\partial f}{\partial \phi}(-\cos\alpha\,\sin\bar{\phi}\,\cos\phi + \cos\bar{\phi}\,\sin\phi)$$

G Viscous Stagnation Region

The surface streamline and convective-heating equations are indeterminate at the stagnation point on the body. Therefore, a limiting solution similar to the analyses of Appendix D and Ref. [8] is found in the stagnation region. This solution gives the initial location and orientation of the streamlines as well as the stagnation values of the momentum thickness and heat transfer.

G.1 Streamline Geometry

Before describing the streamline geometry, define the shock and body surfaces in the stagnation region. Recall from Appendix D that the shock surface may be represented by an elliptic paraboloid as

$$By^2 + z^2 = 2cx \qquad (G.1)$$

where (x,y,z) are referenced to the wind axes. The body surface is also given by an elliptic paraboloid from Eq. (2.3.1):

$$\bar{B}\bar{y}^2 + \bar{z}^2 = 2\bar{x} \qquad (G.2)$$

where $\bar{x}^2$ has been neglected and $(\bar{x},\bar{y},\bar{z})$ refer to the body axes depicted in Fig. 2.5. Transform the body equation to wind axes using Eq. (F.12) to obtain

$$\left(\bar{B}\cos^2\alpha\right) y_b^2 + z_b^2 = 2\left(\frac{1}{\cos\alpha}\right)\left(x_b - n_{b_0}\right) \qquad (G.3)$$

where x_b^2 and $x_b y_b$ have been neglected. Comparing with Eq. (G.1) implies

$$B_b = \bar{B} \cos^2\alpha \qquad c_b = \frac{1}{\cos\alpha}$$

The angles Γ and Γ_b are calculated using Eq. (D.3). However, in the stagnation region, the shock and body coordinates are small so that higher powers of these coordinates may be neglected. That is,

$$y = \mathcal{O}(\epsilon) \qquad z = \mathcal{O}(\epsilon)$$

where ϵ is a small parameter defined in Appendix D. The shock angle Γ may then be approximated as

$$\sin\Gamma \approx 1 \qquad \cos\Gamma = \mathcal{O}(\epsilon)$$

Similarly, the body angle Γ_b reduces to

$$\sin\Gamma_b \approx 1 \qquad \cos\Gamma_b = \mathcal{O}(\epsilon)$$

Because the surface streamlines are integrated with respect to the shock coordinates, the transformation between the shock coordinates (ξ, β) and the body coordinates $(\bar{\xi}, \bar{\beta})$ is needed in the stagnation region. Substitute for Γ and Γ_b in Eqs. (3.2.11) and (3.2.12) and neglect higher powers of ϵ to obtain

$$\mathbf{e}_{\bar{\xi}} \cdot \mathbf{e}_\xi \approx \cos(\bar{\theta} + \sigma_b - \sigma)$$

$$\mathbf{e}_{\bar{\xi}} \cdot \mathbf{e}_\beta \approx \sin(\bar{\theta} + \sigma_b - \sigma)$$

$$\mathbf{e}_{\bar{\beta}} \cdot \mathbf{e}_\xi \approx -\sin(\bar{\theta} + \sigma_b - \sigma)$$

$$\mathbf{e}_{\bar{\beta}} \cdot \mathbf{e}_\beta \approx \cos(\bar{\theta} + \sigma_b - \sigma)$$

The transformation operators at the shock, given by Eqs. (B.8) and (B.9), simplify

to

$$\frac{1}{h_\xi}\frac{\partial}{\partial \xi} \approx \cos\sigma\frac{\partial}{\partial y} + \sin\sigma\frac{\partial}{\partial z}$$

$$\frac{1}{h_\beta}\frac{\partial}{\partial \beta} \approx -\sin\sigma\frac{\partial}{\partial y} + \cos\sigma\frac{\partial}{\partial z}$$

Now substitute into Eqs. (3.2.9) and (3.2.10) to obtain for the transformation

$$
\begin{aligned}
\frac{\mathcal{J}_b}{h_\xi}\frac{\partial}{\partial \xi} \approx &\left[\cos(\bar\theta + \sigma_b - \sigma)(\mathcal{B}_b\cos\sigma + \mathcal{D}_b\sin\sigma)\right.\\
&\left. - \sin(\bar\theta + \sigma_b - \sigma)(\mathcal{A}_b\sin\sigma + \mathcal{D}_b\cos\sigma)\right]\frac{\partial}{\partial y}\\
+ &\left[\cos(\bar\theta + \sigma_b - \sigma)(\mathcal{B}_b\sin\sigma - \mathcal{D}_b\cos\sigma)\right.\\
&\left. + \sin(\bar\theta + \sigma_b - \sigma)(\mathcal{A}_b\cos\sigma - \mathcal{D}_b\sin\sigma)\right]\frac{\partial}{\partial z}
\end{aligned}
$$

and

$$
\begin{aligned}
\frac{\mathcal{J}_b}{h_{\bar\beta}}\frac{\partial}{\partial \bar\beta} \approx &\left[-\sin(\bar\theta + \sigma_b - \sigma)(\mathcal{B}_b\cos\sigma + \mathcal{D}_b\sin\sigma)\right.\\
&\left. - \cos(\bar\theta + \sigma_b - \sigma)(\mathcal{A}_b\sin\sigma + \mathcal{D}_b\cos\sigma)\right]\frac{\partial}{\partial y}\\
+ &\left[-\sin(\bar\theta + \sigma_b - \sigma)(\mathcal{B}_b\sin\sigma - \mathcal{D}_b\cos\sigma)\right.\\
&\left. + \cos(\bar\theta + \sigma_b - \sigma)(\mathcal{A}_b\cos\sigma - \mathcal{D}_b\sin\sigma)\right]\frac{\partial}{\partial z}
\end{aligned}
$$

The geometric terms involving $\mathcal{A}$, $\mathcal{B}$, and $\mathcal{D}$ may be simplified using their definitions

given in Appendix B along with Eqs. (D.9)–(D.12) to obtain

$$\mathcal{B}_b\cos\sigma + \mathcal{D}_b\sin\sigma \approx \cos\sigma\left(1 - \frac{n_{b_0}}{c}\right)$$

$$\mathcal{A}_b\sin\sigma + \mathcal{D}_b\cos\sigma \approx \sin\sigma\left(1 - \frac{n_{b_0}}{c}\right)$$

$$\mathcal{B}_b \sin\sigma - \mathcal{D}_b \sin\sigma \approx \sin\sigma \left(1 - \frac{Bn_{b_0}}{c}\right)$$

$$\mathcal{A}_b \cos\sigma - \mathcal{D}_b \sin\sigma \approx \cos\sigma \left(1 - \frac{Bn_{b_0}}{c}\right)$$

and

$$\mathcal{J}_b \approx \left(1 - \frac{n_{b_0}}{c}\right)\left(1 - \frac{Bn_{b_0}}{c}\right)$$

The transformation between the shock and body coordinates may now be written as

$$\frac{1}{h_\xi}\frac{\partial}{\partial \xi} \approx \cos(\bar{\theta} + \sigma_b)\frac{1}{h_y}\frac{\partial}{\partial y} + \sin(\bar{\theta} + \sigma_b)\frac{1}{h_z}\frac{\partial}{\partial z} \tag{G.4}$$

$$\frac{1}{h_{\bar{\beta}}}\frac{\partial}{\partial \bar{\beta}} \approx -\sin(\bar{\theta} + \sigma_b)\frac{1}{h_y}\frac{\partial}{\partial y} + \cos(\bar{\theta} + \sigma_b)\frac{1}{h_z}\frac{\partial}{\partial z} \tag{G.5}$$

where the scale factors are

$$h_y = 1 - \frac{Bn_{b_0}}{c} \qquad\qquad h_z = 1 - \frac{n_{b_0}}{c}$$

The inviscid surface velocity is represented by

$$\mathbf{V} = \bar{u}_b \mathbf{e}_{\bar{\xi}} \approx U_b \mathbf{e}_y + W_b \mathbf{e}_z$$

$$\approx \bar{u}_b \left[\cos(\bar{\theta} + \sigma_b)\,\mathbf{e}_y + \sin(\bar{\theta} + \sigma_b)\,\mathbf{e}_z\right] \tag{G.6}$$

where the velocity components U and W are functions of the shock coordinates y and z. On the stagnation line ($y = 0$, $z = 0$), the velocity components are equal to zero and from symmetry across $z = 0$,

$$\frac{\partial U}{\partial z} = 0 \qquad\qquad W = 0$$

Therefore, in the stagnation region,

$$U \approx \left(\frac{\partial U}{\partial y}\right)_0 y \qquad\qquad W \approx \left(\frac{\partial W}{\partial z}\right)_0 z$$

The velocity gradients may be calculated for both perfect gas and equilibrium flows

from Eq. (D.24) as

$$
\left(\frac{\partial U}{\partial y}\right)_0 = \frac{B}{c\rho_{s0}}\left\{-\frac{B}{B+1}(\eta-1)\left[2-\frac{1}{\rho_{s0}}(\eta-1)\right]\right.
$$
$$
\left. +2\Delta p + \frac{1}{\rho_{s0}} + \Delta(1/\rho)\left(\eta^2+1\right)\right\}^{1/2} \tag{G.7}
$$

$$
\left(\frac{\partial W}{\partial z}\right)_0 = \frac{1}{c\rho_{s0}}\left\{-\frac{1}{B+1}(\eta-1)\left[2-\frac{1}{\rho_{s0}}(\eta-1)\right]\right.
$$
$$
\left. +2\Delta p + \frac{1}{\rho_{s0}} + \Delta(1/\rho)\left(\eta^2+1\right)\right\}^{1/2} \tag{G.8}
$$

where, at the body surface, $\eta = 0$.

Now the equation of a streamline in terms of the corresponding shock coordinates

can be obtained from Eq. (G.4) and Eq. (G.6) as

$$
\frac{\partial z/\partial\bar{\xi}}{\partial y/\partial\bar{\xi}} = \frac{h_y}{h_z}\tan(\bar{\theta}+\sigma_b) = \frac{h_y z}{\tilde{B}h_z y}
$$

where

$$
\tilde{B} = \frac{\left(\frac{\partial U_b}{\partial y}\right)_o}{\left(\frac{\partial W_b}{\partial z}\right)_o}
$$

Note that $\tilde{B}$ should not be confused with the body geometry parameter $\bar{B}$. This

equation may be integrated to obtain

$$
z^{\tilde{B}\frac{h_z}{h_y}} = \bar{C}y \tag{G.9}
$$

where the parameter $\bar{C}$ is a function of the streamline coordinate $\bar{\beta}$ and y and z

represent the shock coordinates. Remember that the surface streamline coordinates

y_b and z_b are located along the shock normal coordinate n.

The scale factor at the body is found by substituting Eq. (G.9) into Eq. (G.5), so that

$$h_{\bar{\beta}} = \frac{\bar{C}'}{\bar{C}} h_y \frac{yz}{(\tilde{B}^2 y^2 + z^2)^{1/2}} \qquad (G.10)$$

where

$$\bar{C}' \equiv \frac{d\bar{C}}{d\bar{\beta}}$$

The parameter $\bar{C}(\bar{\beta})$ is analogous to the shock line parameter $C(\beta)$. It is determined by assigning a value of $\bar{\beta}$ to each surface streamline in the stagnation region. For convenience, define $\bar{\beta} = \beta$ for the streamlines corresponding to the ϵ-curve $(x_\epsilon, y_\epsilon, z_\epsilon)$ defined in Appendix D. Substituting the ϵ-curve coordinates given by Eq. (D.8) into Eq. (G.9) yields the desired result for $\bar{C}$ as

$$\frac{\bar{C}'}{\bar{C}} = \frac{1}{\sin\beta \cos\beta} \left(\frac{B\tilde{B}\frac{h_z}{h_y} \cos^2\beta + \sin^2\beta}{B\cos^2\beta + \sin^2\beta} \right)$$

The orientation of the surface streamlines is calculated from Eq. (G.6) as

$$\tan(\bar{\theta} + \sigma_b) = \frac{z}{\tilde{B}y} \qquad (G.11)$$

The body angle σ_b may be found using Eqs. (D.3) and (G.3).

$$\tan\sigma_b = \frac{z_b}{B_b y_b}$$

Relate the surface coordinates to the shock coordinates using Eq. (B.13) to obtain

$$y_b = y - n_b \cos\Gamma \cos\sigma \approx h_y y$$

$$z_b = z - n_b \cos\Gamma \sin\sigma \approx h_z z$$

Substituting into Eq. (G.11) yields

$$\tan \bar{\theta} = \frac{yz \left(B_b \frac{h_y}{h_z} - \tilde{B} \right)}{\tilde{B} B_b \frac{h_y}{h_z} y^2 + z^2} \qquad (G.12)$$

This expression can be used to determine the initial orientation of the streamlines by substituting the ϵ-curve coordinates (y_ϵ, z_ϵ) for the shock coordinates (y, z).

G.2 Convective-Heating Equations

In addition to the streamline geometry, the laminar convective-heating equations may also be simplified in the stagnation region. From Eqs. (3.3.1) and (3.3.2), the laminar expressions are given by

$$q_w = 0.22 \left(Re_\theta \right)^{-1} \left(\frac{\rho^*}{\rho_e} \right) \left(\frac{\mu^*}{\mu_e} \right) \rho_e \bar{u}_e \left(h_{aw} - h_w \right) \left(Pr_w \right)^{-0.6} \qquad (G.13)$$

and

$$\theta = \frac{0.664 \left(\int_0^{\bar{\xi}} \rho^* \mu^* \bar{u}_e h_{\bar{\beta}}^2 h_{\bar{\xi}} \, d\bar{\xi} \right)^{1/2}}{\rho_e \bar{u}_e h_{\bar{\beta}}} \qquad (G.14)$$

Since the thermodynamic and transport properties are "even" functions of y and z $(\partial/\partial y = 0, \partial/\partial z = 0)$ at the stagnation point, they may be approximated by their stagnation values as

$$\rho_e \approx \rho_{e_0} \qquad\qquad \rho^* \approx \rho_0^*$$

$$\mu_e \approx \mu_{e_0} \qquad\qquad \mu^* \approx \mu_0^*$$

$$h_{aw} \approx h_{e_0} \qquad\qquad h_w \approx h_{w_0}$$

$$Pr_w \approx Pr_{w_0}$$

where higher order terms have been neglected and Eq. (H.7) has been used to simplify the adiabatic wall enthalpy, h_{aw}. Substituting into Eq. (H.6) yields the reference enthalpy in the stagnation region.

$$h^* \approx \frac{1}{2}\left(h_{e_0} + h_{w_0}\right)$$

The edge velocity is calculated from Eqs. (G.6)–(G.8) as

$$\bar{u}_e \approx \left(\frac{\partial W_e}{\partial z}\right)_0 \left(\tilde{B}^2 y^2 + z^2\right)^{1/2}$$

where $\eta = \eta_e$ is used to obtain W_e. However, the ratio of the velocity gradients, $\tilde{B}$, is still calculated using $\eta = 0$ to keep the analysis simple. This additional approximation causes no great difficulty. The scale factor h_β is given by Eq. (G.10), and the differential arc length along a streamline is found in the same manner as the differential shock line arc length given by Eq. (D.6). The streamline arc length is

$$h_{\bar{\xi}}\, d\bar{\xi} = h_z \left(\tilde{B}^2 y^2 + z^2\right)^{1/2} \frac{dz}{z}$$

Substitute the above expressions into Eq. (G.14) and integrate by making use of Eq. (G.9) to obtain for the momentum thickness:

$$\theta \approx \theta_0 = \frac{0.664}{\rho_{e_0}}\left[\frac{\rho_0^* \mu_0^* h_z}{2\left(\frac{\partial W_e}{\partial z}\right)_0\left(\tilde{B}\frac{h_z}{h_y} + 1\right)}\right]^{1/2} \tag{G.15}$$

The surface heating follows from Eq. (G.13) as

$$q_w \approx q_{w_0} = 0.469 \left(\tilde{B}\frac{h_z}{h_y} + 1\right)^{1/2} (\rho_0^* \mu_0^*)^{1/2}\left[\frac{1}{h_z}\left(\frac{\partial W_e}{\partial z}\right)_0\right]^{1/2}\left(h_{e_0} - h_{w_0}\right)\left(Pr_{w_0}\right)^{-0.6} \tag{G.16}$$

H Convective-Heating Equations

The convective-heating equations developed by Zoby [24] for axisymmetric laminar and turbulent boundary layers are derived from the integral form of the momentum equation [28]. First, define a coordinate system along the axisymmetric body to be (s,n) where s represents the distance along the body surface and n is the distance normal to the body. The corresponding velocity components are u and v and the body radius is given by r. In this system, the momentum equation may be written as

$$\frac{d\theta}{ds} + \frac{\theta}{r}\frac{dr}{ds} + \frac{\theta}{u_e}\frac{du_e}{ds}\left(2 + H + \frac{u_e}{\rho_e}\frac{d\rho_e}{du_e}\right) = \frac{C_f}{2} \tag{H.1}$$

where

$$C_f \equiv \frac{2\tau_w}{\rho_e u_e^2} \qquad\qquad H \equiv \frac{\delta^*}{\theta} \tag{H.2}$$

and the displacement and momentum thicknesses are given by

$$\delta^* = \int_0^\delta \left(1 - \frac{\rho}{\rho_e}\frac{u}{u_e}\right) dn \tag{H.3}$$

and

$$\theta = \int_0^\delta \frac{\rho}{\rho_e}\frac{u}{u_e}\left(1 - \frac{u}{u_e}\right) dn \tag{H.4}$$

Note that δ, δ^*, and θ are the standard symbols for boundary layer flows and should not be confused with the geometry variables δ_ϕ, $\bar{\delta}_\phi$, and $\bar{\theta}$.

For $H = -1$, Eq. (H.5) simplifies to

$$\frac{d}{ds}\left(\rho_e u_e r\theta\right) = \frac{C_f}{2}\rho_e u_e r \tag{H.5}$$

In addition to the simplicity of this relation, Zoby assumes $H = -1$ based on the insensitivity of the turbulent heat transfer to the form factor H for values of approximately 1.0 or less [50, 51]. Lees [52] also uses this value of H in developing a hypersonic laminar method.

Compressibility effects are accounted for by Eckert's reference enthalpy relation [34] which is

$$h^* = \frac{1}{2}\left(h_e + h_w\right) + 0.22\left(h_{aw} - h_e\right) \tag{H.6}$$

where the adiabatic wall enthalpy, h_{aw}, is defined as

$$h_{aw} = h_e + \frac{1}{2}Ru_e^2 \tag{H.7}$$

The recovery factor R is equal to $R \approx Pr^{1/2}$ for laminar flows and $R \approx Pr^{1/3}$ for turbulent flows. The reference enthalpy concept allows the formulas and variables of incompressible flow to be used for compressible flow provided all physical properties are evaluated at the reference enthalpy or temperature. For instance, the skin friction coefficient defined in Eq. (H.2) may be written as

$$C_{f_{inc}} \equiv \frac{2\tau_w}{\rho^* u_e^2}$$

Thus, the relationship between the compressible and incompressible skin friction coefficients is

$$C_f = \frac{\rho^*}{\rho_e}C_{f_{inc}} \tag{H.8}$$

In a similar fashion, the definition of the momentum thickness gives

$$\theta \approx \frac{\rho^*}{\rho_e}\int_0^\delta \frac{u}{u_e}\left(1 - \frac{u}{u_e}\right)dn = \frac{\rho^*}{\rho_e}\theta_{inc} \tag{H.9}$$

whereas the definition of the Reynolds number based on momentum thickness yields

$$Re_\theta = \frac{\rho_e u_e \theta}{\mu_e} = \frac{\mu^*}{\mu_e} Re_{\theta_{inc}} \qquad \text{(H.10)}$$

For both laminar and turbulent flows, the incompressible skin friction coefficient is assumed to be of the form

$$\frac{C_{f_{inc}}}{2} = c_1 \left(Re_{\theta_{inc}} \right)^{-m} \qquad \text{(H.11)}$$

where c_1 and m are constants. Substitute Eqs. (H.8)–(H.10) into Eq. (H.11) to obtain

$$\frac{C_f}{2} = c_1 \frac{\rho^*}{\rho_e} \left(\frac{\mu^*}{\mu_e} \right)^m (Re_\theta)^{-m} \qquad \text{(H.12)}$$

By substituting this relation into Eq. (H.5), the integral form of the momentum equation becomes

$$\frac{d}{ds} (\rho_e u_e r \theta) = \rho_e u_e r c_1 \frac{\rho^*}{\rho_e} \left(\frac{\mu^*}{\mu_e} \right)^m (Re_\theta)^{-m} \qquad \text{(H.13)}$$

This equation may be used to determine the momentum thickness for both laminar and turbulent flows according to the values c_1 and m.

H.1 Laminar Boundary Layer

For the laminar boundary layer over a flat plate, the Blasius [28] solution gives

$$\frac{C_{f_{inc}}}{2} = 0.22 \left(Re_{\theta_{inc}} \right)^{-1}$$

which implies

$$c_1 = 0.22 \qquad m = 1$$

is a good approximation. Substitute these values into Eq. (H.13) and integrate to obtain for the momentum thickness:

$$\theta_L = \frac{0.664 \left(\int_0^s \rho^* \mu^* u_e r^2 ds \right)^{1/2}}{\rho_e u_e r} \tag{H.14}$$

The surface heat transfer is then calculated from a modified Reynolds analogy as

$$St = \frac{C_f}{2} \left(Pr_w \right)^{-0.6}$$

where St is the Stanton number and is defined as

$$St \equiv \frac{q_w}{\rho_e u_e \left(h_{aw} - h_w \right)}$$

Simplify the above relation using Eq. (H.12) and solve for the laminar surface heating rate to obtain

$$q_{w_L} = 0.22 \left(Re_{\theta_L} \right)^{-1} \left(\frac{\rho^*}{\rho_e} \right) \left(\frac{\mu^*}{\mu_e} \right) \rho_e u_e \left(h_{aw} - h_w \right) \left(Pr_w \right)^{-0.6} \tag{H.15}$$

H.2 Turbulent Boundary Layer

For a turbulent boundary layer, the parameters c_1 and m are not constant. They are found by assuming a velocity profile of the form

$$\frac{u}{u_e} = \left(\frac{n}{\delta} \right)^{1/N}$$

where the exponent N is a variable and is computed from a curve fit of axisymmetric nozzle wall data [35] as

$$N = 12.67 - 6.5 \log \left(Re_{\theta_T} \right) + 1.21 \left[\log \left(Re_{\theta_T} \right) \right]^2$$

Equation (H.13) may be integrated assuming c_1 and m are locally constant to give

for the turbulent momentum thickness:

$$\theta_T = \frac{\left(c_2 \int_0^s \rho^* \mu^{*m} u_e r^{c_3}\, ds\right)^{c_4}}{\rho_e u_e r} \qquad \text{(H.16)}$$

where from Ref. [24], the parameters are given by

$$m = \frac{2}{N+1} \qquad\qquad c_3 = 1 + m$$

$$c_1 = \left(\frac{1}{c_5}\right)^{\frac{2N}{N+1}} \left[\frac{N}{(N+1)(N+2)}\right]^m \qquad c_4 = \frac{1}{c_3}$$

$$c_2 = (1+m)c_1 \qquad\qquad c_5 = 2.2433 + 0.93N$$

The surface heat transfer then follows from a modified Reynolds analogy for turbulent

flow as

$$St = \frac{C_f}{2}\left(Pr_w\right)^{-0.4}$$

Solving for the surface heat transfer gives

$$q_{w_T} = c_1 \left(Re_{\theta_T}\right)^{-m} \left(\frac{\rho^*}{\rho_e}\right) \left(\frac{\mu^*}{\mu_e}\right)^m \rho_e u_e \left(h_{aw} - h_w\right)\left(Pr_w\right)^{-0.4} \qquad \text{(H.17)}$$

H.3 Axisymmetric Analog

The laminar flow equations given by Eqs. (H.14) and (H.15) and the turbulent

flow equations given by Eqs. (H.16) and (H.17) are derived for axisymmetric flow.

These relations may be applied to 3-D flows by using the axisymmetric analog [13]

approximation. The axisymmetric analog assumptions allow the axisymmetric bound-

ary layer relations given above to be used in a surface streamline coordinate system

$(\bar{\xi},\bar{\beta},\bar{n})$ provided the following substitutions are made:

$$r = h_{\bar{\beta}} \qquad\qquad ds = h_{\bar{\xi}}d\bar{\xi}$$

where $h_{\bar{\beta}}$ is the scale factor describing the divergence of the surface streamlines and $h_{\bar{\xi}} d\bar{\xi}$ is the differential distance along the streamline.